White dwarf–red dwarf binaries in the Galaxy

White dwarf–red dwarf binaries in the Galaxy

Rode dwerg–witte dwerg dubbelsterren in de Melkweg
(met een samenvatting in het Nederlands)

Een wetenschappelijke proeve op het gebied van de
Natuurwetenschappen, Wiskunde en Informatica.

Proefschrift

ter verkrijging van de graad van doctor
aan de Radboud Universiteit Nijmegen
op gezag van de rector magnificus prof. mr. S.C.J.J. Kortmann,
volgens besluit van het College van Decanen
in het openbaar te verdedigen op woensdag 28 november 2007
om 13.30 uur precies

door

Else Josephina Maria van den Besselaar

geboren op 13 maart 1980
te Schijndel

Promotor: Prof. dr. P.J. Groot

Co-promotor: Dr. L. Morales-Rueda

                       Dr. T. Augusteijn
                       Nordic Optical Telescope
                       La Palma

Manuscriptcommissie: Prof. dr. N. de Groot

                       Dr. G. Nelemans

                       Prof. dr. C. Aerts

                       Prof. dr. L. Kaper
                       Universiteit van Amsterdam

                       Dr. B. Gänsicke
                       University of Warwick, UK

A red dwarf and a white dwarf,
orbiting around
A big one and a small one,
still forever bound

Contents

Chapter 1

Introduction

1.1 White dwarf–red dwarf binaries

This thesis is based on several studies of white dwarf–red dwarf binaries. As the name implies these consist of two stars, a white dwarf and a red dwarf, orbiting each other around the centre of mass of the system. A typical optical spectrum is shown in Fig. 1.1.

1.1.1 White dwarfs

Due to variability in the position of Sirius which was unrelated to the parallax effect, Bessel predicted in 1844 that Sirius had a, by that time, unseen companion Sirius B (Bessel 1844). Eighteen years later, this companion was discovered by Clark (Bond 1862). Decades after its discovery it was noticed that the star was too dim for its temperature. Therefore it was concluded that it was a small star, but relatively heavy as well. Sirius B had around the same mass as the Sun, but a volume about the size of the Earth, so it could not be a normal hydrogen burning star (Hussey 1896; Campbell 1920). This was the first discovery of a white dwarf (Eddington 1924; Adams 1925). Soon after this discovery many more white dwarfs were found. The explanation for the physical nature of white dwarfs was a mystery for many years.

When a star is born, it will burn hydrogen in its core producing heat which, in the form of gas pressure, balances the gravity. After exhaustion of the hydrogen in the core, gravity takes over and causes the core to contract while the outer layers expand, until helium burning starts in the core. When
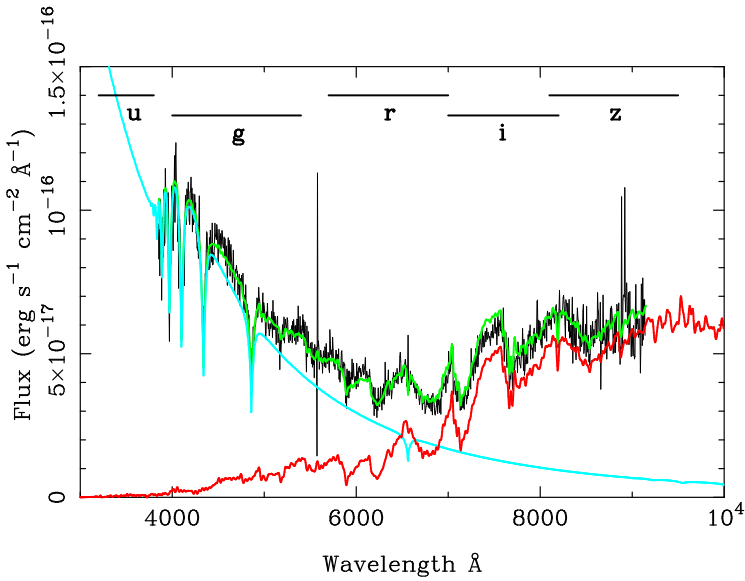
Figure 1.1: *A typical example of a white dwarf–red dwarf binary. This is SDSS J145527.72+611504.6 composed of a white dwarf with a temperature of 22 000 K and log g of 7.5 (dominating in the blue part) and a red dwarf of spectral type M4 (dominating in the red part). The grey/green line on top of the black line is the composite spectrum of the two single stars.*

the helium is exhausted the core will contract again, while the outer layers expand further. For stars with initial masses $\lesssim 8 - 11$ M$_\odot$ the contraction of the core will stop due to electron degeneracy pressure, preventing the density and temperature to rise high enough for the carbon to ignite.

For a normal gas the pressure is the result of the combination of temperature and density according to the ideal gas law. In degenerate matter the density is so high that the pressure arises from the Pauli exclusion principle. This states that two identical particles cannot have the same quantum state. A quantum state is defined by the position, momentum and spin of a particle. For fermions (e.g. electrons) two spin states are allowed and therefore no more than two fermions can share the same position and momentum. In a high density environment, the position of an electron is highly confined, causing its momentum to be increased to occupy a higher quantum level which is needed to comply with the Pauli exclusion principle. As

the momentum is proportional to the velocity, the electrons are on average moving fast, independent of the temperature, which produces a pressure that balances the gravity so that the star is in equilibrium again.

White dwarfs are stars with an electron degenerate core that have on average a mass of 0.6 $M_\odot$ in a volume the size of the Earth (Kothari 1932). Usually there is a small layer of ideal gas of hydrogen (DA white dwarfs) or helium (DB white dwarfs) present around the degenerate core. A model of a DA white dwarf spectrum is shown in Fig. 1.1 as the line going from the upper left to the lower right of the diagram. White dwarfs are born with temperatures around $100\,000$ K. Since there are no nuclear burning processes in a white dwarf the radiation only comes from the dissipation of its remnant thermal energy and therefore the white dwarf will cool with time (Koester 1972).

1.1.2 Red dwarfs

Red dwarfs are normal low-mass hydrogen burning stars of spectral type M. They have a mass of ≤ 0.5 $M_\odot$ and a surface temperature of around $3\,000$ K (Kirkpatrick et al. 1991, 1993). The spectrum of a red dwarf is characterized by molecular absorption bands, mainly titanium-oxide. A template red dwarf spectrum is shown in Fig. 1.1 as the line going from the lower left to the upper right of the diagram. Due to the low mass of red dwarfs, the temperature in the core is relatively low and therefore hydrogen is burnt at a low rate. The typical time scale for hydrogen burning in red dwarfs is 150×10^9 years. This is far longer than the age of the Universe and therefore all red dwarfs should still be on the main-sequence.

1.2 Binary evolution

A large number of binaries observed today that contain at least one stellar remnant, have orbital separations less than the maximum size of the progenitor of the remnant(s). Therefore a strong orbital shrinkage must have taken place during the evolution of the binary.

If two main-sequence stars form a binary, their individual evolution may be influenced by the companion. The geometry of the gravitational potential created by the two stars close to each other is called the Roche geometry (Fig. 1.2). Close to the stars the equipotential surfaces are spheres within
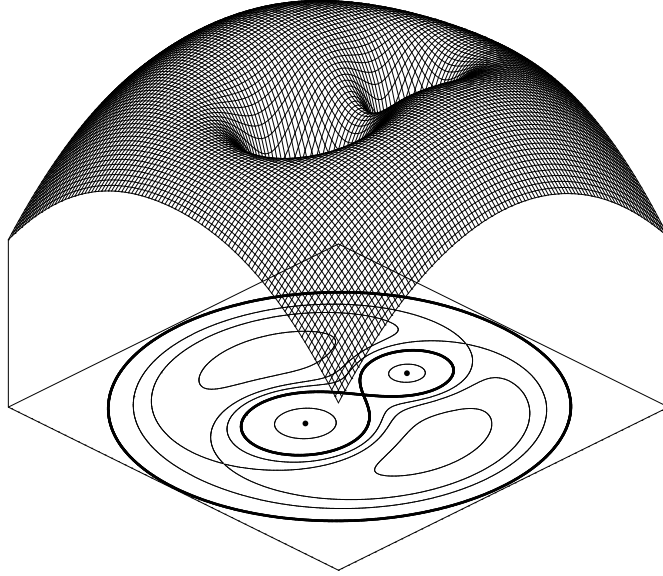
Figure 1.2: *The Roche geometry in a close binary with the Roche Lobes as the figure of eight. (Figure by Martin Heemskerk)*

which the material is gravitationally bound to each star. Further out the influence of the other star becomes more noticeable and the equipotential surfaces become distorted. The critical equipotential surface where a saddle point occurs between the two stars is called the Roche Lobe (see Fig. 1.2), and the saddle point itself is the inner Lagrangian point (L_1). The size of the Roche Lobe (R_L) of the more massive star (primary) can be determined by using the approximation formula of Eggleton (1983)

$$\frac{R_{\rm L}}{a} = \frac{0.49q^{\frac{2}{3}}}{0.6q^{\frac{2}{3}} + \ln(1 + q^{\frac{1}{3}})},\tag{1.1}$$

with $q = M_1/M_2$, where M_1 is the mass of the primary star and M_2 the mass of the less massive star (secondary), and a the orbital separation. The size of the Roche Lobe of the secondary is determined by using $q = M_2/M_1$.

When the initially more massive star turns into a giant and is located in a binary with an initial orbital period of $\leq$10 years (depending on the masses of the components, Taam & Sandquist 2000), the star becomes larger than

its Roche Lobe and mass transfer starts through the point connecting the two Roche Lobes, the inner Lagrangian point, to the secondary star. If the time scale for mass transfer is considerably shorter than the thermal time scale of the secondary in which it can adjust its structure, the accreted layer will heat up and fill the Roche Lobe of the secondary. This will result in a common-envelope which encompasses both stars (Paczyński 1976). A common envelope phase will start depending on several factors: the mass ratio of the two components at the moment the star fills its Roche Lobe, the evolutionary stage of the secondary star, and the depth of the convection layer in the mass-losing star (Iben & Livio 1993).

During the common-envelope phase the secondary star and the core of the giant will spiral-in towards each other due to friction between the stars and the envelope. The energetics with which the common-envelope is rejected are relatively uncertain (Iben & Livio 1993). A fraction of the orbital angular momentum that is lost in the spiral-in process is converted into angular momentum of the common-envelope which can eject (part) of the envelope from the system. A parameter α_{CE} is used to describe the fraction of the orbital energy that is used for the ejection of the common-envelope (Webbink 1984; de Kool et al. 1987; de Kool 1992):

$$\frac{GM_i(M_i - M_c)}{R_i} = \alpha_{\text{CE}}\lambda\left(\frac{GM_cM_2}{2a_f} - \frac{GM_iM_2}{2a_i}\right), \qquad (1.2)$$

with λ being a numerical value dependent on the structure of the star, M_c being the core mass of the giant, R_i being the radius of the giant at the start of mass transfer, and a_i and a_f being the separations between the stars at the start of the mass transfer and after the common-envelope phase, respectively. α_{CE} is usually $0 \leq \alpha_{\text{CE}} \leq 1$, but for double white dwarfs it is found to be ≥ 1 (Nelemans & Tout 2005); i.e. more energy is needed than is available in the orbit.

The physics of the common-envelope is not very well understood due to the intrinsically three-dimensional problem and the large number of physical processes that are involved. It is expected that the common-envelope phase is very short ($\leq 1\,000$ years, Taam & Sandquist 2000). Therefore it is virtually impossible to study this phase directly and is it better to focus on the results after it has taken place. The outcome of a common-envelope phase depends on the initial masses of the main-sequence binary, the initial

orbital period and the physics of the common-envelope phase. If a merger between the core of the giant and the secondary star can be avoided, a close binary containing a stellar remnant emerges. Examples of close binaries are cataclysmic variables where a main-sequence star loses mass to a white dwarf companion, X-ray binaries where a main-sequence star loses mass to a neutron star companion, and close detached binaries. White dwarf–red dwarf binaries are examples of detached binaries which are relatively simple to model due to the lack of mass transfer and are relatively easy to find due to their intrinsically equal luminosities, but one being blue and the other one being red. Therefore, white dwarf–red dwarf binaries are almost ideal probes to study binary evolution.

1.3   Known white dwarf–red dwarf binaries

At the start of this thesis a few hundred white dwarf–red dwarf binaries were known (including wide binaries and ones without known orbital periods) and they were found in several ways. A large fraction of these binaries was found in surveys as ultraviolet excess sources, such as the Palomar-Green survey (Green et al. 1986). Other discoveries were made by searching for infra-red excess in known white dwarfs in i.e. the Two Micron All-Sky Survey (Wachter et al. 2003). Both of these methods are biased towards binaries which are (very) blue, so binaries in which the white dwarf dominates. Another way to find white dwarf–red dwarf binaries is to use common proper motion studies (Silvestri et al. 2001). The binaries found with common proper motion searches usually have large orbital separations, which means that it is unlikely that they went through a common-envelope phase in their past. In order to be able to study binary evolution with the use of white dwarf–red dwarf binaries it is necessary to have a large, homogeneous sample.

Almost all the white dwarfs in the known white dwarf–red dwarf binaries have a hydrogen-rich atmosphere (DA white dwarfs). There were only a few binaries with non-DA white dwarfs known. These were GD 325 and CBS 47 with a DB white dwarf (Greenstein 1975; Wagner et al. 1988), and EG 388 with a DC white dwarf (Moffett et al. 1985). In the case of single white dwarfs it is found that 9-15% have helium dominated atmospheres (Kleinman et al. 2004) while the fraction in binaries is apparently much

Table 1.1: *Characteristics of the SDSS filters.*

Name	λ_{center} (Å)	FWHM (Å)
u'	3543	567
g'	4770	1387
r'	6231	1373
i'	7625	1526
z'	9134	950

lower. The reason for this difference is unknown.

1.4   Sloan Digital Sky Survey

In this thesis the Sloan Digital Sky Survey (SDSS; York et al. 2000) is intensively used to find white dwarf–red dwarf binaries. The SDSS is a survey of about a fifth of the full sky in five filter bands covering the whole optical wavelength range. The characteristics of the filters are given in Table 1.1 and schematically shown in Fig. 1.1. Furthermore, for about 1% of the objects a spectrum, covering the range between 3850 and 9150 Å, is also taken.

The main aim of the SDSS is to map and study the galaxies and quasars in the universe, and it covers mainly mid to high galactic latitudes. Large numbers of galactic objects are found as a by-product of the survey. A good classification can be made on the colours alone because of the five filters present in the SDSS. At the moment the SDSS is the deepest ($r \leq 22.3$; Grebel 2001) and largest optical survey undertaken.

White dwarf–red dwarf binaries are expected to form a bridge between the single white dwarfs and the single red dwarfs in a colour-colour diagram. Quasars occupy the same colour space, but do not show a measurable proper motion. Therefore, a combination of colours and proper motion is the best way to find white dwarf–red dwarf binaries. Figure 1.3 shows the location in a colour-colour diagram where to find these binaries based on a proper motion limit of $\leq$ 20 mas yr^{-1}. Each of the tracks corresponds to the location of binaries with a certain secondary spectral type combined with white dwarfs of different temperatures. Selecting binaries in this way does
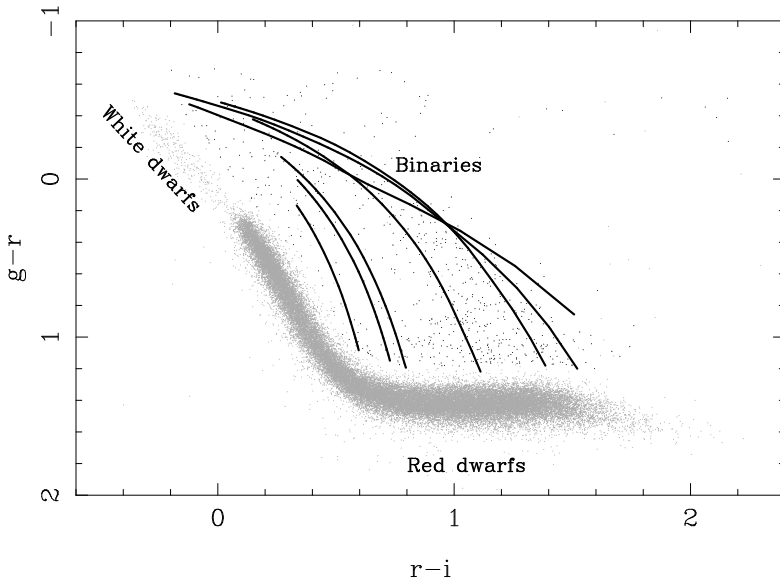
Figure 1.3: *Colour-colour diagram showing the positions of the single white dwarfs, single red dwarfs, and white dwarf–red dwarf binaries.*

not have biases towards either white dwarf dominated systems, red dwarf dominated systems or only wide binaries. This all together makes the SDSS a very good starting point for selecting a large and homogenous sample of white dwarf–red dwarf binaries.

1.5   This thesis

This thesis covers several studies on white dwarf–red dwarf binaries. Chapter 2 explores the fact that almost no binaries are found containing a non-DA white dwarf. In Chapter 3 a detailed study of the post-common-envelope, eclipsing white dwarf–red dwarf binary DE Canum Venaticorum is carried out. In Chapter 4 a method to select white dwarf–red dwarf binaries on the basis of their SDSS colours and proper motions by using the catalog of Gould & Kollmeier (2004) is presented. The objects with spectra in the SDSS are analysed and fitted with models in Chapter 5. The third chapter focussing on the proper motion and colour selected sample (Chapter 6)

discusses the implications for the galactic population of white dwarf–red dwarf binaries and the space densities for the thin disc, thick disc, and halo fractions.

Chapter 2

Identification of 13 DB + dM and 2 DC + dM binaries from the Sloan Digital Sky Survey[1]

E.J.M. van den Besselaar, G.H.A. Roelofs, G.A. Nelemans,
T. Augusteijn, P.J. Groot

Abstract

We present the identification of 13 DB + dM binaries and 2 DC + dM binaries from the Sloan Digital Sky Survey (SDSS). Before the SDSS only 2 DB + dM binaries and 1 DC + dM binary were known. At least three, possibly 8, of the new DB + dM binaries seem to have white dwarf temperatures well above 30 000 K which would place them in the so called DB-gap. Finding these DB white dwarfs in binaries may suggest that they have formed through a different evolutionary channel than the ones in which DA white dwarfs transform into DB white dwarfs due to convection in the upper layers.

2.1   Introduction

Our understanding of binary evolution is still severely lacking on a number of points, but most importantly on the physics of common-envelope (CE) evolution (Paczyński 1976). When binaries are close enough that during their evolution Roche lobe overflow can commence from a convective giant to a less massive main-sequence companion star, very quickly the system will evolve into a state where the envelope of the giant encompasses both objects. After the envelope has been expelled a close binary may result that will evolve into a white dwarf – main-sequence binary. Due to its short-lived phase and the intrinsic three-dimensional hydrodynamic nature of the CE phase the physics of this process is not well understood (e.g. Iben & Livio 1993).

One way of improving our knowledge of the CE phase is to determine the space densities and population characteristics of all CE products. Some of these products are white dwarfs (WD) with a low-mass main-sequence (dM) companion. WD + dM binaries (or pre-Cataclysmic Variables), containing a hydrogen-rich white dwarf (DA), are a fairly well known group of objects of which new members are readily found, among others by the efforts of the Sloan Digital Sky Survey (SDSS, York et al. 2000; Raymond et al. 2003). On the contrary, WD + dM binaries containing a helium-rich white dwarf (DB) showing composite spectra are extremely rare, and from literature before the SDSS only two such objects are known, namely GD 325 (Greenstein 1975) and CBS 47 (Wagner et al. 1988). Identification of objects in these classes may not only help in understanding the CE physics and the evolution of Cataclysmic Variables (CVs), but also in the formation of DBs in the first place.

For single WDs in the SDSS it is found that 9-15% of all systems have helium dominated atmospheres (Kleinman et al. 2004; Harris et al. 2003). In contrast, the fraction of WDs in known binaries that are DBs is $\ll 1\%$. DC white dwarfs (absorption lines less than 5% of the continuum; Wesemael et al. 1993) + dM binaries are an even rarer class with only one member known (EG 388; Moffett et al. 1985). We here report on the discovery of 13 new DB + dM binaries and 2 DC + dM binaries from the SDSS.
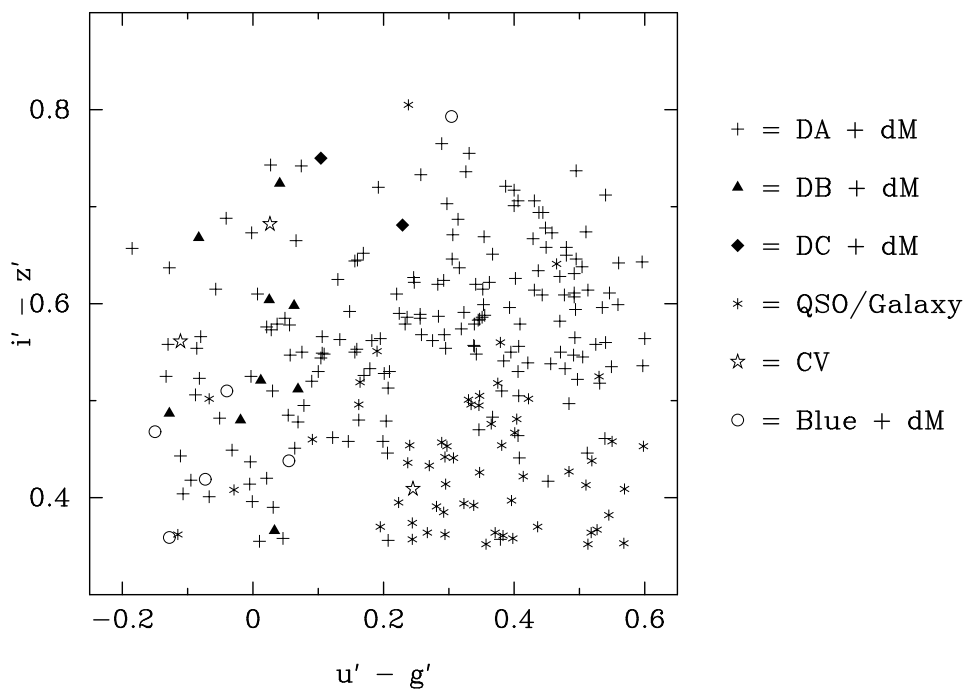
Figure 2.1: *A $u - g$ vs. $i - z$ diagram of our 260 objects together with their classification based on visual inspection of all the spectra satisfying our selection criteria.*

2.2   Observations

Colour selection of WD + dM binaries

We have used the spectroscopic data from the Third Data Release of the SDSS (DR3) to select WD + dM candidates. Because of their composite spectra these binaries stand apart from normal main-sequence stars in any colour – colour diagram (see e.g. Fig. 1 of Raymond et al. 2003). We have used the following colour criteria for selecting candidates: $-0.2 < u' - g' < 0.6$, $-0.2 < g' - r' < 0.3$, $0.35 < r' - i' < 0.85$ and $0.35 < i' - z' < 0.85$, where the magnitudes are the psf-magnitudes taken from the spectrophotometric table of DR3. These criteria were derived from colour – colour diagrams of an initial set of WD + dM binaries that were selected from the spectroscopic database.

Using these colour criteria, we selected 260 objects. We classified them on the basis of visual inspection of their spectra. Of these objects 58 were classified as quasars or galaxies. A further 6 were too noisy to be classified, leaving 196 dM binaries. These are further classified as 176 DA + dM binaries, 9 DB + dM binaries, 2 DC + dM binaries, 3 Cataclysmic Variables and 6 dM binaries with a blue component too noisy to classify. A $u' - g'$ vs. $i' - z'$ diagram is shown in Fig. 2.1.

Equivalent width selection of DB + dM binaries

A second, independent, search for DB + dM binaries was performed by looking for He absorption lines in all DR3 spectra. Apart from single DBs this should select all DB + dM binaries in which the DB dominates the blue part of the spectrum. In practice, this means selecting binaries in which the DB has a $T_{\text{eff}} \geq 20\,000$ K with a companion of spectral type M1 or later, and binaries in which the DB has a $T_{\text{eff}} \geq 14\,000$ K with a companion of spectral type M3 or later. For all spectra we calculated the equivalent width (EW) of the He I 4026, 4471, 4921 and 5876 Å lines. On the basis of the distributions of EWs in a sample of 160 bright DBs and requiring that all four lines are present, DB candidates were selected such that less than an estimated 5% of all DBs fall outside the selection due to weak absorption lines.

All resulting candidates from DR3 were visually inspected for DB + dM signatures. The 9 DB + dM binaries from our colour selection were
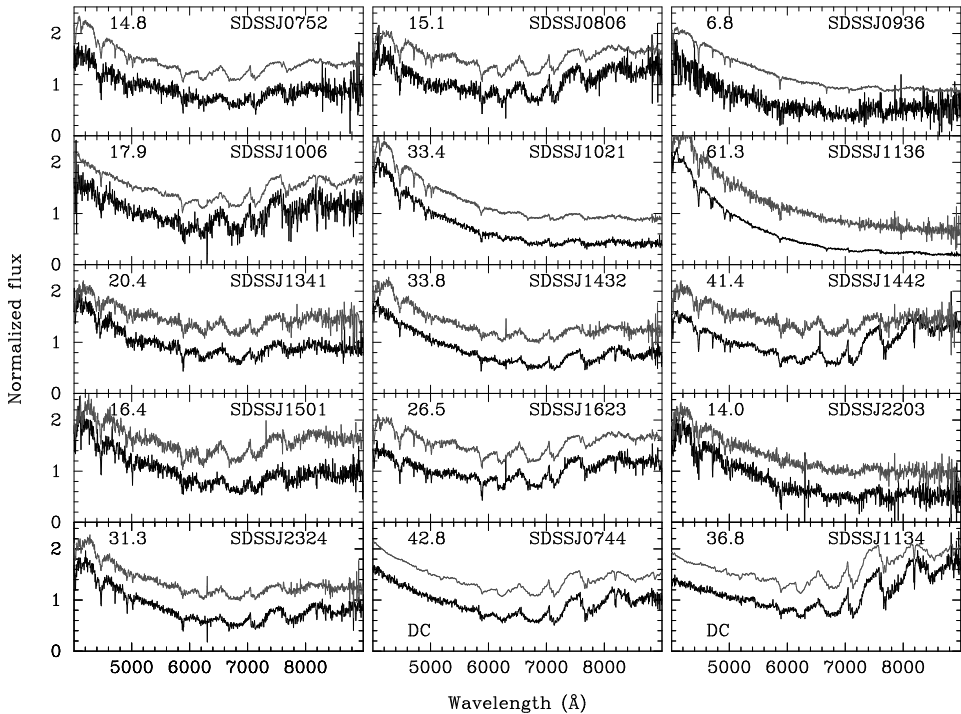
Figure 2.2: *The 13 DB + dM and 2 DC + dM (bottom row) systems (Table 2.1). The object spectra are shown as the lower spectra, the best template has been shifted upwards for clarity. The number in the upper left corner of each plot is the S/N in a 5 Å bin at 4600 Å.*

re-discovered and 4 additional systems (outside our colour selection) were identified, increasing the total number of these rare systems found in the SDSS to 13.

2.3 Results

We fitted the DB + dM spectra with a combined template DB and template dM spectrum using the χ^2 minimalization method. For the fit we have scaled the flux in the template spectra to a distance of 10 pc before combining them. The 17 template DB spectra and their corresponding temperatures, between 13390 and 38211 K, were taken from Kleinman et al. (2004). To

Table 2.1: *The characteristics of our thirteen DB + dM and two DC + dM binaries are given in this table. The uncertainties are about one subtype for the dM star and about 4000 Kelvin in WD temperature for a fixed dM spectral type.* [a] *See Sect. 2.3.* [b] *These temperatures are shown as given in Kleinman et al. (2004) for the best fit template WD. The objects are DC + dM binaries.*

Name	g	$u-g$	$g-r$	$r-i$	$i-z$	T_{WD}	dM	D (pc)	χ^2
SDSS J075235.79+401339.0	20.01	0.05	0.01	0.58	0.39	30252	M3V	1544	1.64
SDSS J080636.85+251912.1	19.61	0.07	0.21	0.79	0.60	24266	M3V	1045	1.68
SDSS J093645.14+420625.6[a]	20.37	−0.09	−0.14	0.42	0.07	15919	M5V	860	2.01
SDSS J100636.39+563346.8	19.42	0.10	0.28	0.72	0.49	14575	M4V	531	3.70
SDSS J102131.55+511622.9	18.27	−0.25	−0.37	0.14	0.35	30252	M4V	700	1.56
SDSS J113609.59+484318.9[a]	16.80	−0.38	−0.54	−0.16	0.14	38211	M6V	354	4.00
SDSS J134135.23+612128.7	19.14	−0.10	0.12	0.50	0.48	30694	M3V	1054	2.20
SDSS J143222.06+611231.1	18.53	0.02	−0.08	0.49	0.60	36815	M3V	879	3.56
SDSS J144258.47+001031.5[a]	18.35	0.04	0.08	0.80	0.72	30694	M3V	674	11.22
SDSS J150118.40+042232.3[a]	19.57	0.02	−0.01	0.49	0.48	26020	M3V	1220	2.42
SDSS J162329.50+355427.2	18.77	0.02	0.22	0.65	0.53	24266	M3V	695	3.46
SDSS J220313.29+113236.0	19.34	−0.08	−0.10	0.22	0.45	30694	M4V	1085	2.04
SDSS J232438.31−093106.5	18.64	−0.08	−0.16	0.41	0.66	36815	M3V	911	3.45
SDSS J074425.42+353040.8[a,b]	18.91	0.23	0.03	0.70	0.68	15700	M4V	481	7.14
SDSS J113457.72+655408.7[a,b]	18.15	0.10	0.10	0.02	0.75	12500	M4V	278	9.59

derive the temperature of the DC white dwarfs, we have fitted blackbody spectra with a temperature range of $8\,000 - 40\,000$ K. The 7 dM spectra ranging from type M0V to M6V were taken from Pickles (1998).

The best fit Kleinman-temperatures (or blackbody temperatures in case of a DC + dM), spectral types, and χ^2 for the 15 non-DA + dM binaries are given in Table 2.1. In most cases, the uncertainty in spectral type of the dM is 1 subtype or less. For a fixed dM the uncertainty on the temperature of the WD is estimated to be about 4000 K. However, there is a correlation between the WD temperature and the dM spectral type. For a fit with a dM one subtype later, the best template WD may have a $8\,000 - 10\,000$ K lower temperature with slightly increased χ^2. The spectra are shown in Fig. 2.2 (hereafter we will abbreviate names to the form SDSSJhhmm). The object spectra are the lower spectra, while the template spectra are the upper ones.

In this paper we give all the parameters as derived assuming a WD with a radius of 0.0123 R$_\odot$, identical to Raymond et al. (2003). The mass-radius relation from Eggleton as quoted by Verbunt & Rappaport (1988) gives a corresponding mass of 0.6 M$_\odot$ for this radius. We used several WD radii between 0.007 and 0.02 R$_\odot$ (a mass between 1.08 and 0.21 M$_\odot$, respectively) in all our fits. For the DB + dM binaries the WD temperature, dM spectral type and overall χ^2 change only very slightly with different radii. However, for the DC + dM binaries the fit improves for a WD with a radius of 0.008 R$_\odot$ (a mass of about 1 M$_\odot$).

SDSSJ0936

Due to the low signal-to-noise the blue component in SDSSJ0936 is tentatively classified as a DB, but a better spectrum is needed to confirm this.

SDSSJ1136

SDSSJ1136 shows He II absorption at 4686 Å and possibly at 5411 Å indicating a high WD temperature. Close inspection shows clear features of a cool companion to the WD. Our best fit to this spectrum is with the combination of a WD with a temperature of $38\,211$ K and an M6 companion which are our hottest template WD and coolest template dM spectra. The χ^2 is still rather high (see Table 2.1), suggesting at least a WD with a temperature $> 38\,000$ K and possibly a companion with a spectral type later than M6V.

SDSSJ1442

The best fit to this object is still rather poor. If we decrease the radius of the WD in the fit to 0.009 $R_\odot$, the fit result is significantly better. Raymond et al. (2003) have included this object in their paper but they only mention that it has He absorption. In their Table 1 they have given a temperature of 32 000 K, but this is based on a hydrogen WD model. In Table 1 of Harris et al. (2003) SDSSJ1442 is classified as a DB3.5 + M binary but it is not discussed further in their paper either. Furthermore, Raymond et al. (2003) have taken 2 follow-up spectra of this object, because it shows signs of chromospheric activity through strong Hα emission, and find a minimum radial velocity variation of 150 km s^{-1}. This suggests that SDSSJ1442 is a close binary.

SDSSJ1501

The object SDSSJ1501 is mentioned in the table of Raymond et al. (2003) but is not mentioned elsewhere in that paper. They have fitted a hydrogen WD model to this spectrum, which might (partly) explain the difference in temperature and dM spectral type between our results and theirs. SDSSJ1501 clearly shows He absorption and no hydrogen absorption and therefore should be classified as a DB + dM binary.

SDSSJ0744 & SDSSJ1134

The blue parts of the spectra of SDSSJ0744 and SDSSJ1134 show no absorption lines from the WD stronger than 5% of the continuum and are therefore classified as DC + dM binaries. The object SDSSJ1134 is mentioned in the table of Raymond et al. (2003) as well and was also fitted with a hydrogen WD model. If we use a smaller radius which corresponds to a WD mass of about 1 $M_\odot$ the fits improve to $\chi^2 \approx 4$. This results in later type M dwarf secondaries.

2.4   Discussion

We have identified 13 DB + dM binaries and 2 DC + dM binaries in the SDSS DR3 and we derived the WD temperature, dM spectral type and distance of these binaries.

Almost no single DBs have been found with temperatures between 30 000 and 45 000 K, the so called DB-gap (Liebert et al. 1986). Kleinman et al.

(2004) have found some DBs with temperatures above 30 000 K in the SDSS, but only 11 out of 171 single DBs. Although better spectra and modeling with WD atmospheric models is needed, 3 of our 13 DB + dM binaries appear to have temperatures well above this limit and another 5 have temperatures around 30 000 K. The fraction of DBs in the DB-gap for these binaries is therefore very high compared to the total DB population. From the fact that we do find cool DBs as well, it is clear that this is not due to our selection method. As mentioned before, if the fitted dM spectral type is 1 subtype too early, the temperature may drop with 8 000 – 10 000 K. Even in this worst-case scenario, still at least 3 binaries will have temperatures close to the DB-gap. SDSSJ1136 shows He II absorption which suggest a temperature of above 30 000 K, placing it in the DB-gap. Follow-up observations of all 13 DB + dM systems is needed to obtain high S/N spectra. Then we can model these spectra with WD atmospheric models to be certain which part of this sample is in the DB-gap.

It is thought that during the cooling sequence DAs can transform into DBs due to convective mixing in the H layer for temperatures below 30 000 K (e.g. Kalirai et al. 2005). WDs in close binaries might accrete some matter from their companions, making their H layers too thick for the transition to DBs. However, the fact that we do find DBs in (close) binaries may imply that they are formed in a different way so that they have lost their H (almost) completely. This could also explain their existence in the DB-gap and would suggest the DB/DA ratio in binaries might be different from that in single WDs.

The DB/DA fraction for single WDs in the SDSS is 9-15% (Kleinman et al. 2004; Harris et al. 2003). To derive the fraction of DB/DA in binary systems we can not use the EW selection. The He lines in DBs are very useful in an EW selection, but this is not possible for H lines due to the dominance of main-sequence stars. Therefore we use the sample based on the colour selection to derive the DB/DA ratio in binary systems, yielding 5%. Due to the colour selection this could be biased, but the nine DB + dM binaries that we selected from the colour selection show a similar spread in temperature as the other DB binaries in the sample. This indicates that our colour selection does not specifically bias towards binaries with certain WD temperatures, indicating that the ratio is different in binaries than in single stars, though a more detailed study is necessary.

Raymond et al. (2003) estimate that about 5% of the WD + dM are close

binaries with short orbital periods. They have taken 2 follow-up spectra of SDSSJ1442 from which a minimum radial velocity variation of 150 km s^{-1} can be derived. From this value it can be assumed that SDSSJ1442 is a close binary. Hα emission in close binaries can be enhanced due to faster rotation of the secondary or due to strong heating of the secondary by the WD, so Hα emission can be an indication of a close binary (e.g. Raymond et al. 2003). In our sample there are 3 systems (SDSSJ1341, SDSSJ1432 and SDSSJ1442) that show Hα emission. Follow-up observations of all the sources in our sample is needed to determine if they are close binaries, and to compare their periods to those of DA + dM binaries to investigate the formation channel.

Acknowledgements

DE Canum Venaticorum: A bright, eclipsing red dwarf–white dwarf binary[1]

E.J.M. van den Besselaar, R. Greimel, L. Morales-Rueda, G. Nelemans,
J.R. Thorstensen, T.R. Marsh, V.S. Dhillon, R.M. Robb, D.D. Balam,
E.W. Guenther, J. Kemp, T. Augusteijn, P.J. Groot

Abstract

Close white dwarf–red dwarf binaries must have gone through
a common-envelope phase during their evolution. DE CVn is a
detached white dwarf–red dwarf binary with a relatively short
($\sim$8.7 hours) orbital period. Its brightness and the presence
of eclipses makes this system ideal for a more detailed study.
From a study of photometric and spectroscopic observations
of DE CVn we derive the system parameters that we discuss
in the framework of common-envelope evolution. Photometric
observations of the eclipses are used to determine an accurate
ephemeris. From a model fit to an average low-resolution spec-
trum of DE CVn, we constrain the temperature of the white
dwarf and the spectral type of the red dwarf. The eclipse light
curve is analysed and combined with the radial velocity curve

---

of the red dwarf determined from time-resolved spectroscopy to derive constraints on the inclination and the masses of the components in the system. The derived ephemeris is $\mathrm{HJD_{min}} = 2\,452\,784.5533(1) + 0.3641394(2) \times \mathrm{E}$. The red dwarf in DE CVn has a spectral type of M3V and the white dwarf has an effective temperature of $8\,000$ K. The inclination of the system is $86^{+3°}_{-2}$ and the mass and radius of the red dwarf are $0.41 \pm 0.06\ M_{\odot}$ and $0.37^{+0.06}_{-0.007}\ R_{\odot}$, respectively, and the mass and radius of the white dwarf are $0.51^{+0.06}_{-0.02}\ M_{\odot}$ and $0.0136^{+0.0008}_{-0.0002}\ R_{\odot}$, respectively. We found that the white dwarf has a hydrogen-rich atmosphere (DA-type). Given that DE CVn has experienced a common-envelope phase, we can reconstruct its evolution and we find that the progenitor of the white dwarf was a relatively low-mass star ($\mathrm{M} \le 1.6 M_{\odot}$). The current age of this system is $3.3 - 7.3 \times 10^9$ years, while it will take longer than the Hubble time for DE CVn to evolve into a semi-detached system.

3.1 Introduction

Large gaps remain in our knowledge of binary stellar evolution that affect our understanding of not only evolved compact binaries, but also of phenomena such as supernovae type Ia explosions, the rate of neutron star–neutron star mergers, and the number of gravitational wave sources in our Galaxy. The poorly understood physics of the common-envelope (CE) phase results in considerable uncertainty in the binary evolution (Paczyński 1976). During the evolution of a binary, the more massive star turns into a giant. When the initial orbital period is small enough ($\lesssim 10$ years, Taam & Sandquist 2000), the envelope of the giant will encompass the secondary star. The secondary and the core of the giant will spiral in towards each other in a CE. When the envelope is expelled a close binary consisting of the core of the giant, which will evolve towards a white dwarf, and the un-evolved secondary star may emerge (see, e.g., Nelemans & Tout 2005).

The CE phase is expected to be very short ($\lesssim 1000$ years, Taam & Sandquist 2000) and is therefore virtually impossible to observe directly. To study the effects of this phase it is best to focus on objects that have most probably undergone a CE phase in their past. These we iden-

tify with binary systems containing at least one stellar remnant where the current orbital separation is smaller than the radius of the giant progenitor (usually with orbital periods ≤ 1 day).

Eclipsing close binaries offer the greatest possibility of deriving precise physical parameters of the stars. The masses, radii, and orbital separations give insight into the binary evolution and specifically tell us if a CE phase has happened sometime in their past. Some examples of detached, close white dwarf–low-mass main-sequence star (red dwarf) eclipsing binaries are: RR Cae (Bruch 1999), NN Ser (Haefner 1989), EC13471-1258 (O'Donoghue et al. 2003), GK Vir (Green et al. 1986), and RX J2130.6+4710 (Maxted et al. 2004). For a review on detached white dwarf–red dwarf binaries see, e.g., Marsh (2000) and Schreiber & Gänsicke (2003). The latest list of white dwarf–red dwarf binaries is in Morales-Rueda et al. (2005, with ten new systems compared to Marsh (2000)). It is necessary to study as many of these systems as possible to be able to compare their characteristics with population synthesis models and to find their space densities as a function of composition (e.g., white dwarf temperature, spectral type, age).

DE CVn (RX J1326.9+4532) is a relatively unstudied, bright ($V = 12.8$) eclipsing binary. It was first discovered as an X-ray source by ROSAT (Voges et al. 1999) and has a proper motion of $-0.198\pm0.002''$ yr^{-1} in right ascension and $-0.178\pm0.003''$ yr^{-1} in declination, as given in the USNO-B1 catalog (Monet et al. 2003). This object was first studied photometrically by Robb & Greimel (1997). From the light curve and the unequal maxima they derived an orbital period of 0.364 days. The asymmetry in their light curve needed a star spot to accurately model the light curve. Robb & Greimel (1997) measured eclipse depths of 0.054 ± 0.010 magnitude in the R-band and 0.128 ± 0.029 magnitude in the V-band.

Holmes & Samus (2001) obtained $UBVRI$ photometry for five nights in June 2000. They confirm the dependence of the eclipse depth with colours and found minimum depths of the eclipse of 0.10 magnitude in I, 0.15 in R, 0.30 in V, 0.60 in B, and 1.00 in U. The differences with wavelength band indicate that the two stars have very different colours.

We note a difference in the eclipse depths as quoted by Holmes & Samus (2001) compared to the values from Robb & Greimel (1997). Although Holmes & Samus (2001) give their values as being eclipse depths, when looking at the light curve we suggest that they have taken the difference

between minimum and maximum light instead of the difference between the start and minimum of the eclipse, which is used by Robb & Greimel (1997) and in the present work.

DE CVn consists of an M-type star with a spectroscopically unseen companion, presumably a white dwarf. Throughout this paper we will refer to the M dwarf as the secondary component and the probable white dwarf as the primary component. In Sect. 3.2 we describe our observations and reductions. The results are shown in Sect. 3.3, and the conclusions are given in Sect. 3.4.

3.2   Observations and reductions

3.2.1   Photometry

Our photometric dataset consists of various observations taken on a number of telescopes. Table 3.1 lists an overview of our photometric datasets taken with the 1.3-meter telescope of the Michigan-Dartmouth-MIT (MDM) Observatory (Arizona), with the 4.2-meter William Herschel Telescope (WHT) on La Palma with ULTRACAM (Dhillon & Marsh 2001), with the automatic 0.5-meter telescope of the Climenhage Observatory in Victoria, Canada (referred to as UVic), and with the 1.8-meter telescope of the Dominion Astrophysical Observatory (DAO) located in Victoria, Canada.

To reduce dead-time for the MDM observations, the CCD was binned 2×2, resulting in a scale of $1.02''$ per binned pixel, and only a subregion of 256×256 (binned) pixels was read. These observations were reduced with standard packages in the Image Reduction and Analysis Facility (IRAF)[2]. We derived differential photometry with respect to one comparison star (RA = 13:26:59.6, Dec = +45:33:05, J2000) that is bright enough in the sparse field. The UVic and DAO observations were reduced with standard packages in IRAF.

The ULTRACAM data were reduced with standard aperture photometry. Differential photometry was obtained with respect to two comparison stars located at RA = 13:26:28.08, Dec = +45:33:11.6 (J2000) and RA = 13:26:39.2, Dec = +45:34:56.1 (J2000). The coordinates of DE CVn are RA = 13:26:53.2, Dec = +45:32:46.1 (J2000).

---

[2]IRAF is distributed by the National Optical Astronomy Observatories, which are operated by the Association of Universities for Research in Astronomy, Inc., under coop-

Table 3.1: *Log of the photometric data of DE CVn.*

Date	Tel	Filter	T (s)	#
(1)	(2)	(3)	(4)	(5)
12 Apr 1997	UVic	R	99	173
21 Apr 1997	UVic	R	99	168
22 Apr 1997	UVic	R	120	176
24 Apr 1997	UVic	R	140	118
2 May 1997	UVic	R	99	175
8 May 1997	UVic	R	99	37
8 May 1997	UVic	V	120	39
9 May 1997	UVic	clear	34	164
10 May 1997	UVic	clear	33	476
1 Jul 1998	UVic	R	140	102
17 Mar 2000	UVic	clear	99	52
21 May 2001	UVic	R	120	160
26 May 2001	DAO	B	40	110
2 Jun 2001	UVic	clear	40	130
21 Jan 2002	MDM	B	60	193
24 Jan 2002	MDM	$BG38$	4	597
30 May 2002	DAO	B	30	39
1 Jul 2002	MDM	$BG38$	5	216
3 Feb 2003	MDM	B	10	350
22 May 2003	ULTRACAM	$u'g'i'$	1.3	$\sim$750
24 May 2003	ULTRACAM	$u'g'i'$	1.3	$\sim$2860
25 May 2003	ULTRACAM	$u'g'i'$	1.3	$\sim$3780
19 Jun 2003	MDM	B	10	166
4 May 2004	ULTRACAM	$u'g'i'$	1.3	$\sim$13000
5 Apr 2006	UVic	clear	33	359

Notes: Col. (1): observing date; Col. (2): used telescope, see text for explanations; Col. (3): used filter; Col. (4): integration time per observation; Col. (5): number of observations.

Table 3.2: *Log of spectroscopic observations.*

Date	Tel	λ (Å)	T (s)	#	R(Å)
(1)	(2)	(3)	(4)	(5)	(6)
11 May 1998	TLS	4300–5300	900	21	0.14
12 - 18 May 1998	TLS	5650–10 000	900	75	0.16
19 - 22 Jan 2002	Modspec	4250–7550	120	62	3.5
16 Feb 2002	Modspec	4250–7550	120	5	3.5
19 Feb 2002	Modspec	4250–7550	120	10	3.5
5 - 7 May 2002	CCDS	4180–5100	300	18	3.2
13 May 2002	CCDS	4180–5100	360	1	3.2
13 May 2002	CCDS	4180–5100	600	1	3.2
12 Jun 2002	MkIII	4250–7550	90	1	3.7
13 Jan 2004	Modspec	4250–7550	180	1	3.5
17 - 18 Jan 2004	Modspec	4250–7550	180	2	3.5
6 Mar 2004	Modspec	4250–7550	180	2	3.5
30 Jan 2006	ISIS	3000–8000	180	1	5
30 Jan 2006	ISIS	3000–8000	240	6	5
15 May 2006	DAO	3500–5150	720	6	4.8

Notes. Col. (1): observing date; Col. (2): used spectrograph, where TLS indicates the 'Karl Schwarzschild' Tautenburg Echelle Spectrograph mounted at the the 2m telescope of the Thüringer Landessternwarte; Modspec stands for the 2.4m Hiltner Telescope (MDM) Modular Spectrograph; CCDS is the 2.4m Hiltner Telescope CCD Spectrograph; MkIII is for the 2.4m Hiltner Telescope Mark III Spectrograph; and DAO stands for the Cassegrain Spectrograph at the 1.8m of the DAO. Col. (3): wavelength range of the spectra; Col. (4): integration time per observation; Col. (5): number of observations; Col. (6): resolution as derived from the FWHM of the arc lines.

3.2.2   Spectroscopy

A log of our spectroscopic data set is given in Table 3.2. The TLS echelle spectra are reduced with standard packages in IRAF. We could not correct the TLS spectra for flat fielding because the sky/twilight flat fields would introduce only more lines in the spectra. The wavelength calibration was done with ∼300 lines in the Th-Ar arc spectra with a root-mean-square

erative agreement with the National Science Foundation.

residual of $\sim$0.0036 Å. We checked the stability of the spectrograph by using sky lines and these are not shifted between the observations. Because of the unavailability of sky background or flux standards, the echelle spectra are not sky subtracted or flux-calibrated. These spectra were taken during grey time, so we do not expect problems with the background level. The MDM (using the Modspec, CCDS, MkIII spectrographs), DAO, and ISIS spectra were all reduced with standard packages in IRAF and these are, except for the DAO spectra, approximately flux calibrated (a seeing matched slit width was used, limiting the accuracy of the photometric calibration).

3.3   Results

3.3.1   Eclipse light curves

The first ephemeris of the primary eclipse in DE CVn is given in Robb & Greimel (1997). We take the mid-eclipse times as the mid-point between the start of the ingress and the end of the egress. From our photometric observations and the times of minima given in Tas et al. (2004) we have determined the ephemeris of the eclipse minima by fitting a straight line to the cycle numbers as derived from the ephemeris of Robb & Greimel (1997):

$$\mathrm{HJD_{min}} = 2\,452\,784.5533(1) + 0.3641394(2) \times \mathrm{E}. \qquad (3.1)$$

No significant aliases were found near this period. The uncertainties (last digits) are derived for $\Delta\chi^2 = 1$ when we scale the individual errors to obtain that the reduced $\chi^2 = 1$. The value of the orbital period is further confirmed by the radial velocity analysis described in Sect. 3.3.5. The availability of two eclipses separated by only two cycles (-6109 and -6107) leaves no cycle count ambiguity. Two mid-eclipse times of Tas et al. ($2\,452\,411.3156$ and $2\,452\,412.4078$) were rejected due to the large phase shifts ($\Delta\phi > 0.01$, in contrast to an average scatter of 0.004 for all other eclipses) with respect to the updated ephemeris of Robb & Greimel (1997), leaving 23 mid-eclipse times for determining the ephemeris. When calculating the phase difference with our new period, it turns out that these two data points indeed have a large phase difference ($\Delta\phi > 0.01$), so most probably the published times of the minima are incorrect. The times of the minima together with the cycle
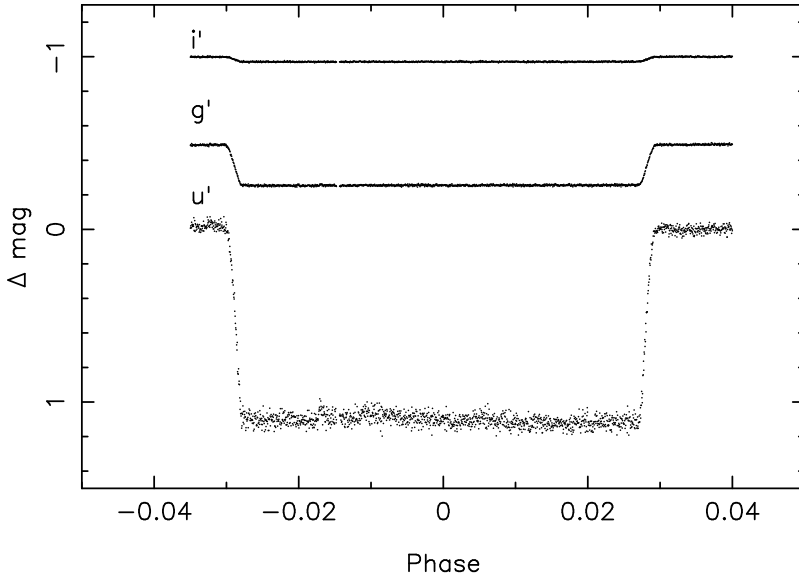
Figure 3.1: *Primary eclipse observed with ULTRACAM.*

number and the corresponding time difference are given in Table 3.3.

We observed a primary eclipse simultaneously in u', g', and i' with UL-TRACAM. These data show the largest eclipse depth of 1.11 ± 0.04 magnitudes in u'. The eclipse depths in g' and i' are 0.235 ± 0.004 and 0.028 ± 0.004 magnitudes, respectively, where we have fitted straight lines to the out-of-eclipse points and in eclipse points to derive these values. The difference is taken as the eclipse depth. The uncertainties are derived for $\Delta \chi^2 = 1$ when we scale the individual errors to obtain that the reduced $\chi^2 = 1$.

3.3.2 Apparent magnitudes

In Table 3.4 we give the magnitudes of DE CVn in and out of eclipse of the ULTRACAM data as obtained with the second comparison star as given in Sect. 3.2.1. Also the MDM magnitudes and the magnitudes of the comparison stars are given. The MDM photometry taken on January 21, 2001 was obtained near phase 0.7, well outside the eclipse. The transformation to standard magnitudes was derived using observations of four Landolt standard fields. Except for $U-B$, the transformations derived from the standard

Table 3.3: *Times of mid-eclipse for the binary DE CVn. The numbers in parentheses are the uncertainties on the mid-eclipse times in the last digits.*

HJD-2 450 000	cycle	Δ (HJD)
550.9214(16)[a]	−6134	−0.00060
560.0243(16)[a]	−6109	−0.00118
560.7531(20[a])	−6107	−0.00066
562.9374(22)[a]	−6101	−0.00120
570.9497(14)[a]	−6079	0.00004
576.7749(14)[a]	−6063	−0.00100
578.9606(6)[a]	−6057	−0.00013
995.9003(18)[b]	−4912	−0.00010
1620.7628(15)[b]	−3196	−0.00089
2050.8125(16)[b]	−2015	0.00012
2055.9103(7)[c]	−2001	−0.00003
2062.8289(7)[b]	−1982	−0.00008
2295.8782(4)[d]	−1342	−0.00003
2298.7914(1)[d]	−1334	0.00006
2411.3156(1)[eg]	−1025	0.00517
2412.4078(22)[eg]	−1022	0.00495
2413.4958(4)[e]	−1019	0.00053
2424.7839(6)[c]	−988	0.00031
2456.8279(4)[d]	−900	0.00004
2673.85488(14)[d]	−304	−0.00009
2705.5359(3)[e]	−217	0.00079
2727.3837(4)[e]	−157	0.00023
2784.553370(25)[f]	0	0.00000
2809.6788(1)[d]	69	−0.00019
3830.7256(4)[b]	2873	−0.00040

Notes: [a] Robb & Greimel (1997); [b] UVic photometry; [c] DAO photometry; [d] MDM photometry; [e] Tas et al. (2004); [f] ULTRACAM photometry; [g] Not used for determining the ephemeris.

Table 3.4: u', g', i' (ULTRACAM, May 24, 2003), and UBVI (MDM) magnitudes of DE CVn and the two comparison stars with the uncertainty on the last digits in parentheses.

	u'	g'	i'	V	$U-B$	$B-V$	$V-I$
DE CVn in eclipse	16.43(1)	13.74(1)	11.65(2)	-	-	-	-
DE CVn out-of-eclipse	15.31(1)	13.50(1)	11.62(2)	12.908(2)	0.070(15)	1.263(5)	2.244(2)
Comparison 1	15.16(1)	13.22(1)	12.29(2)	-	-	-	-
Comparison 2	15.77(1)	13.61(1)	13.34(2)	13.418(2)	0.155(13)	0.708(5)	0.784(4)
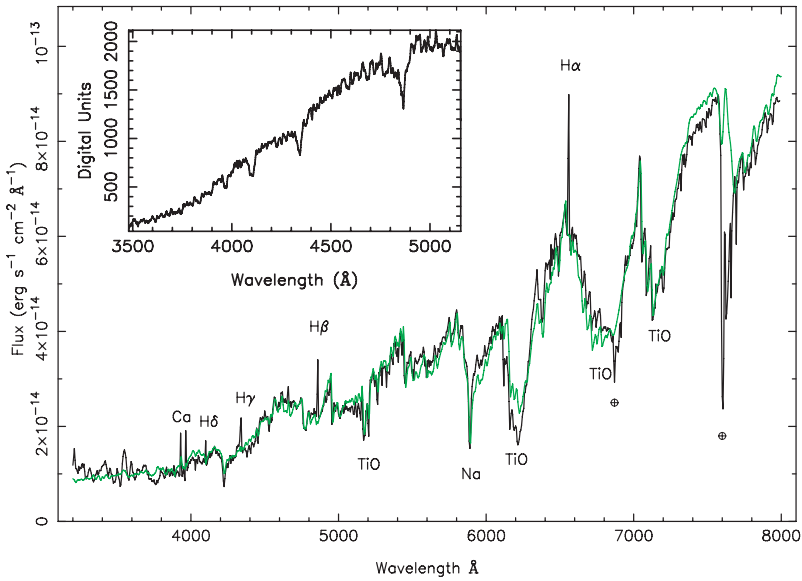
Figure 3.2: *A combined ISIS spectrum of DE CVn (black line) together with a composite template of an M3V star from Pickles (1998) and a DA white dwarf with a temperature of $8\,000$ K and $\log g = 7.5$ (grey/green line). Emission lines of $H\alpha$, $H\beta$, $H\gamma$, and $H\delta$ are visible in the spectrum as well as the Ca II H&K emission lines and the TiO absorption bands of the M dwarf. No spectral line signatures of the primary are visible. The difference between the in and out-of-eclipse spectra shows the underlying white dwarf, which is plotted in the upper left corner.*

stars all had scatter below 0.03 mag. For $U - B$ the scatter is below 0.08 mag.

We derived the u', g', and i' magnitudes of DE CVn in and out of eclipse in the ULTRACAM data of May 24, 2003. The part just before the actual eclipse is taken for the out-of-eclipse magnitudes. All the ULTRACAM magnitudes were derived by using the two comparison stars in the field as mentioned in Sect. 3.2.1. Smith et al. (2002) values were used to derive the u', g', and i' magnitudes. The magnitudes for DE CVn were the same using either comparison star within $\sim$0.01 mag in g' and i', and $\sim$0.02 mag in u' (1σ uncertainty).

3.3.3   The nature of the components

DE CVn has not been studied spectroscopically before. An average low resolution spectrum taken with the ISIS spectrograph on the WHT on La Palma is shown in Fig. 3.2. Clearly visible are the absorption bands of TiO indicating an M-type star. Emission lines of Hα, Hβ, Hγ, Hδ, and Ca II H&K are visible as well.

DE CVn is a single-lined spectroscopic eclipsing binary. We do not see any spectral features of the white dwarf in the overall spectrum. The six low dispersion DAO spectra referred to in Table 3.2 were observed consecutively before, during, and after an eclipse of the white dwarf by the red dwarf. The sum of the two spectra taken during the eclipse were then subtracted from the sum of the two spectra taken immediately before the eclipse. The resultant smoothed spectrum is plotted in Fig. 3.2. Using the spectra taken after the eclipse resulted in a similar spectrum. The strong hydrogen absorption lines are typical of a DA white dwarf, and by visually comparing our WD spectrum with the ones in Wesemael et al. (1993), we come to a spectral type of DA7 $\pm$ 0.5, which corresponds to a temperature of $7\,500 \pm 1\,000$ K. The lack of residual Ca II K and narrow hydrogen emission lines gives us confidence that the subtraction was done correctly and the spectra did not need to be scaled.

To determine the characteristics of the two components we fit the averaged ISIS spectrum with a composite model consisting of a white dwarf and a red dwarf. We first corrected the spectra for the radial velocity variations as a function of phase before averaging the ISIS spectra. The comparison spectra that were used to fit the data consist of a white dwarf model spectrum with a hydrogen atmosphere and temperatures between $1\,500$ and $17\,000$ K (kindly made available to us by P. Bergeron: Bergeron et al. 1991, 1995). From the most likely white dwarf mass and radius as derived from the eclipse fitting in Sect. 3.3.8, we derive a surface gravity for the white dwarf of $\log g \sim 7.8$. Therefore we have used only white dwarf template spectra with surface gravity $\log g = 7.5$. A red dwarf template (M0V to M6V in integer types) together with the corresponding absolute visual magnitude was taken from the library of Pickles (1998). We first scaled the individual spectra to 10 pc before adding them together. We calculated the reduced χ^2 of the fit to the average ISIS DE CVn spectrum for all the different model composite spectra to determine the nature of the components in this

binary. The composition of the model spectrum with the lowest reduced χ^2 is taken as the best combination. A more extended description of the fitting procedure will be given in a future paper.

For the fitting of DE CVn, we have excluded the wavelength regions around the emission lines of Hα, Hβ, Hγ, Hδ, and Ca II H&K and the earth atmosphere bands. The best fit consists of the combination of a red dwarf with spectral type M3V and a white dwarf with a temperature of $8\,000$ K, although the corresponding formal reduced χ^2 is high (511). The second best fit has a $\Delta\chi^2 = 50$. When we take all the combinations with a $\chi^2 < 1\,000$, the spectral type of the red dwarf stays the same, while the temperature varies between $7\,000$ and $9\,000$ K. Therefore we take an uncertainty on the temperature of $1\,000$ K. If we used $\log g = 8.0$ instead of $\log g = 7.5$, the spectral type of the secondary stayed the same, while the temperature changed to $10\,000 \pm 1\,500$ K. Combined with the temperature estimate from the eclipse (end of this section) and the difference spectrum (see above), we decided to use the results from the fitting with the $\log g = 7.5$ models.

The spectrum of DE CVn together with the best fit is shown in Fig. 3.2. Consistent results are found when fitting the MDM spectra, which cover a shorter wavelength range. The discrepancy between the data and the fit of the spectrum is likely due to flux calibration errors, different intrinsic properties of the red dwarf such as metallicity, and the non-removal of telluric features in our spectra.

Another method to derive the secondary spectral type is by using the TiO5 index. Reid et al. (1995) have given the best-fit linear relation between the spectral type of a late-type main-sequence star and its TiO5 band strength:

$$S_{\mathrm{p}} = -10.775 \times \mathrm{TiO5} + 8.2, \qquad (3.2)$$

where TiO5 is the band strength as defined by $F_{\mathrm{w}}/F_{\mathrm{cont}}$ with F_{w} the flux in the 7126–7135 Å region and F_{cont} as the flux in the 7042–7046 Å region. Using this definition we have calculated the TiO5 band strength and the corresponding spectral type for all the MDM spectra covering the wavelength range given above. The white dwarf contribution to this part of the spectrum is very small ($\leq 5\%$), so this will not affect the ratio. The corresponding average S_{p} is 2.17, corresponding to spectral type M2.

From the single M3 spectrum of Pickles (1998) we have calculated the

TiO5 band strength and corresponding spectral type as well. This gives a strength of 0.55 and a spectral type of 2.27. By comparing the value of the M3 spectrum with the intrinsic variation as seen in Fig. 2 of Reid et al. (1995), we see that this value is consistent with the values derived for DE CVn. From this we see that the different methods are consistent with a red dwarf of spectral type M3 as used by Pickles (1998).

From the apparent magnitudes of DE CVn in eclipse and outside eclipse, we can derive the colour of the unseen white dwarf that is being eclipsed. This gives $(u' - g')_{\mathrm{WD}} = 0.52 \pm 0.01$ and $(g' - i')_{\mathrm{WD}} = -0.26 \pm 0.02$. By comparing this with the values from the white dwarf models the $u' - g'$ colour indicates a temperature of $7\,000$–$9\,000$ K, while the $g' - i'$ colour indicates $6\,000$–$8\,000$ K. This is fully consistent with the spectral modelling.

Table 3.5: *Identified lines in the TLS echelle spectra and the ISIS ([a]) spectrum together with their equivalent widths.*

λ_{obs} (Å)	λ (Å)	Element	EW (Å)
(1)	(2)	(3)	(4)
3797.20^a	3797.91	H 10	−0.9
3832.45^a	3835.397	H 9	−1.8
3887.33^a	3889.05	H 8	−2.1
3932.47^a	3933.67	Ca II K	−6.2
3968.10^a	3970.874	Hϵ+ Ca II H	−7.5
4101.26^a	4101.735	Hδ	−2.8
4340.00^a	4340.465	Hγ	−3.7
4860.63^a	4861.327	Hβ	−4.1
5094.51	5093.646	Fe II	0.4
5099	5098.703	Fe I	<0.2
5164	5163.940/5164.70	Fe II/Fe I	<0.2
5167	5167.000	TiO	<0.2
5210	5209.900	Fe I	<0.2
5230	5229.857	Fe I	<0.2
5240	5240.000	TiO	<0.2
6102.78	6101.100	K IV	1.3
6122.01	6122.219	Ca I	1.8
6157.08	6159	TiO	0.9
6381.49	6384	TiO	0.8

Table 3.5: *Continued.*

λ_{obs} (Å)	λ (Å)	Element	EW (Å)
(1)	(2)	(3)	(4)
6388.01	6388.410	Fe I	0.8
6393.13	6391.214/6391.51	Mn I/Ti II	0.4
6421.11	6421.355	Fe I	0.3
6439.01	6439.073	Ca I	0.9
6449.78	6450.854	Ba I	1.0
6462.64	6462.566	Ca I	1.2
6471.56	6472.34	Sm II	0.5
6494.22	6493.78	Ca I	1.0
6499.39	6498.759	Ba I	0.5
6562.75	6562.76	Hα	−6.7
6572.81	6572.781	Ca I	0.5
6593.79	6595.326	Ba I	0.5
6626.22	6627.558	Fe I	0.3
6651.83	6651	TiO	0.4
6685.09	6681	TiO	0.9
6719.14	6715	TiO	1.3
6760.15	6760.61	Fe I	0.4
6764.56	6764.13	Fe I	0.3
6768.72	6768.65	Ti I	0.4
6773.05	6772.36	Ni I	0.3
6777.97	6777.44	Fe I	0.3
6806.81	6806.85	Fe I	0.3
6815.83	6815	TiO	0.5
6921.45	6920.16	Fe I	0.3
7055.51	7054	TiO	1.5
7060.87	7059.941	Ba I	0.6
7088.90	7088	TiO	1.0
7126.37	7126	TiO	1.3
7148.12	7148.147	Ca I	0.4
7326.21	7326.146	Ca I	0.6
7400.12	7400.87/7400.23	Fe I/Cr I	0.2
7462.33	7461	Fe I	0.3
7590	7589	TiO	blended

Table 3.5: *Continued.*

λ_{obs} (Å)	λ (Å)	Element	EW (Å)
(1)	(2)	(3)	(4)
7666	7666	TiO	blended
7674	7671	TiO	blended
7701	7704	TiO	blended
7800.24	7800.00	Si I	0.3
8047.31	8047.6	Fe I	0.3
8182.88	8183.256	Na I	1.4
8194.69	8194.79/8194.82	Na I	1.4
8325	8323.428	H	blended
8362	8361.77	He I	blended
8379	8377.6	Ne I	blended
8382	8382.23	Fe I	blended
8387	8387.78	Fe I	blended
8411	8412.97	Fe I	blended
8424	8424.14/8424.78	Fe I/O I	blended
8662.03	8661.908	Fe I	1.0
8674.98	8674.751	Fe I	0.3
8688.44	8688.633	Fe I	0.5
8806.51	8805.21	Fe I	0.4
8824.21	8820.45	O I	0.6

Notes: Col. (1): wavelength of the line as measured in the echelle spectra; Col. (2): wavelength corresponding to the element that we identify this line with (Col. (3)); Col. (4): equivalent width of the line. Lines without an equivalent width measurement are blended with sky lines. The typical uncertainty on the EW is ∼0.1 Å.

3.3.4   Spectral line variations

The spectra show emission lines of hydrogen up to H 10 and Ca II H&K emission. We have searched the normalised TLS echelle spectra for spectral lines showing radial velocity variations, either in phase with the Balmer and Ca II H&K lines or in anti-phase. All lines identified are listed in Table 3.5 together with their equivalent widths (EW). No lines were seen to move in anti-phase with the Balmer lines. The lines that do not have an EW value are blended with sky lines so that we cannot derive an accurate value

for the EW. The EW of the bluest H lines were measured in the average ISIS spectrum for which we first removed the phase shifts in the individual spectra.

3.3.5   Radial velocity curve

Radial velocities of the Hα lines in the TLS spectra were determined by fitting a single Gaussian line profile and a first-order polynomial to the emission line and the surrounding continuum. The radial velocities of the Hβ and Hγ lines in the TLS spectra were also measured in this way. The typical uncertainties on the radial velocities of the TLS spectra for Hα, Hβ, and Hγ are $\sim$0.3 km s^{-1}, $\sim$0.4 km s^{-1}, and $\sim$0.7 km s^{-1}, respectively. The MDM spectra were cross-correlated with an M dwarf spectrum over the 6000–6500 Å range. The uncertainties for these cross-correlated radial velocities are $\sim$2.2 km s^{-1}.

To derive the semi-amplitude of the radial velocity variations of the secondary and the systemic velocity we use the measurements of the Hα line in the TLS spectra because these are the most accurate measurements. There is no spectral line feature of the primary star visible in the spectra, so therefore we cannot derive the semi-amplitude of the white dwarf. We have used the function

$$f(\phi) = \gamma + K_2 \sin\left(2\pi(\phi - \phi_0)\right), \tag{3.3}$$

where K_2 is the semi-amplitude of the secondary star and γ the systemic velocity in km s^{-1} to fit the data. The best fit gives $\gamma = -7.5 \pm 3$ km s^{-1}, $K_2 = 166 \pm 4$ km s^{-1}, and $\phi_0 = -0.004 \pm 0.004$ for fitting only the TLS Hα variations. The uncertainties are derived from $\Delta\chi^2 = 1$ when the reduced $\chi^2 = 1$. The phase of the radial velocity curve is consistent with the time of mid-eclipse. The fit is shown in Fig. 3.3 together with the measured radial velocity variations of Hα. The residuals of Hα, Hβ, Hγ, and the TiO absorption features are shown Fig. 3.4. When fitting for an eccentric orbit, we find an insignificant eccentricity of $e = 0.02 \pm 0.02$, so assuming a circular orbit is justified. No differences in the radial velocity curves of Hβ, Hγ, and TiO absorption with respect to the Hα observations are observed.
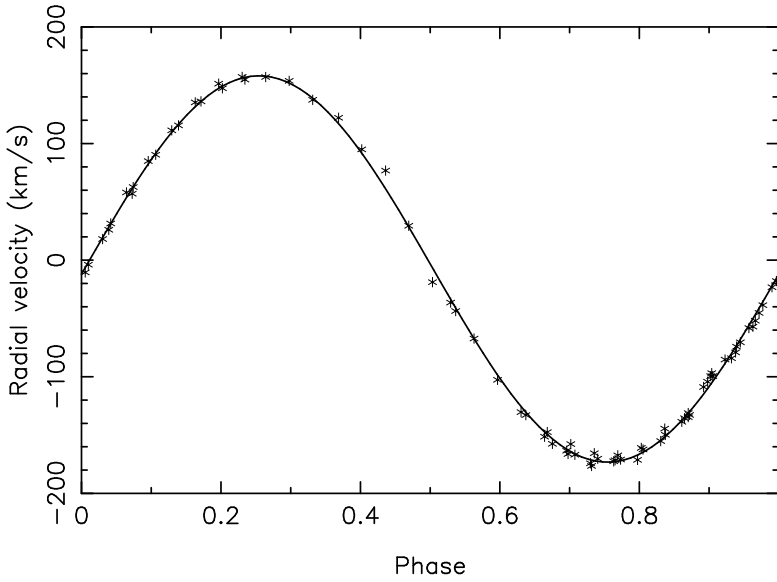
Figure 3.3: *Radial velocity measurements for the Hα lines. The solid line is the best fit to these velocities, as discussed in Sect. 3.3.5. The uncertainties on the points are smaller than the symbols.*
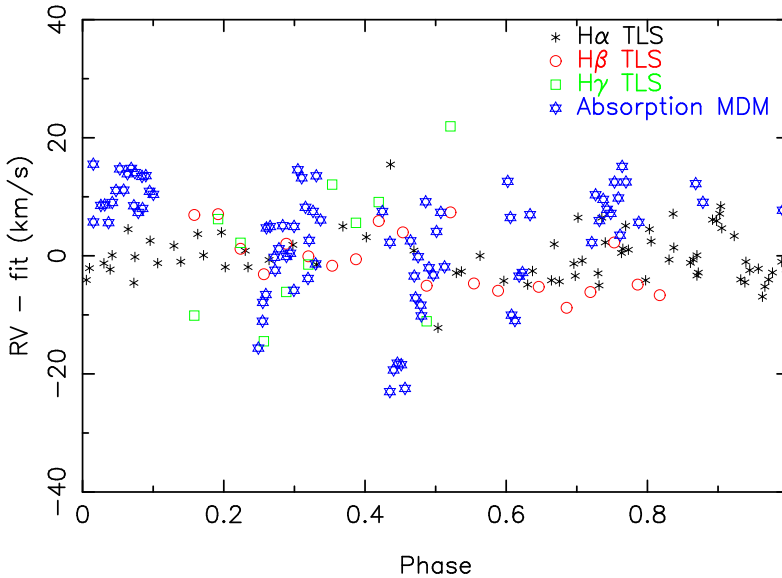
Figure 3.4: *Residuals of the Hα, Hβ, Hγ, and the MDM absorption lines as compared with the best-fit sinusoid to the Hα data.*
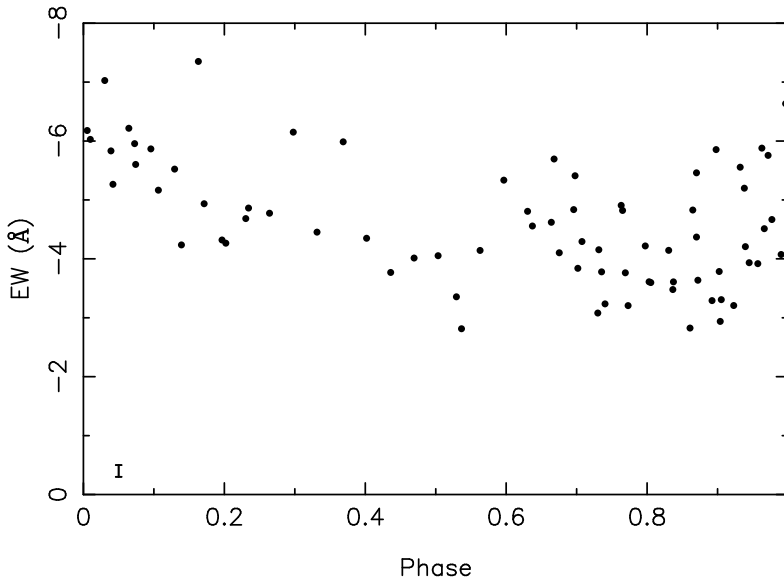
Figure 3.5: *The equivalent width of the Hα line in the TLS spectra. The variations are folded on the orbital period of DE CVn. A typical error bar is shown in the bottom left corner.*
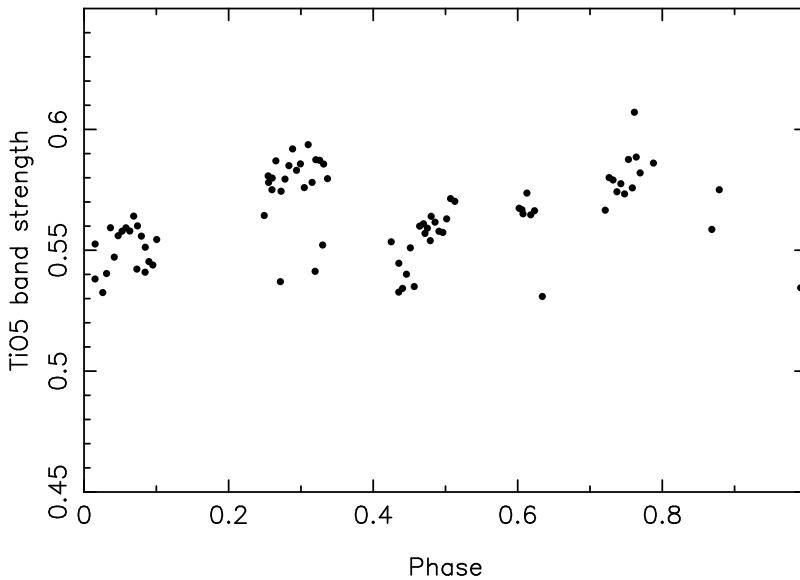
Figure 3.6: *TiO5 band strength of the MDM spectra as a function of orbital phase. The uncertainty on each point is smaller than the symbol.*

3.3.6 Irradiation

In close binary systems we may expect to see irradiation on the red dwarf due to heating of the close white dwarf. To investigate this effect we have measured the variations of the EW of the Hα line. In Fig. 3.5 we show the variations of the EW of this line folded on the orbital period. A typical error bar is shown in the bottom left corner of the figure. There is considerable variation of the Hα line, but this does not coincide with the time scale of the orbital period. During the eclipse, the EW is larger compared to the one outside the eclipse. If the Hα emission originates in the atmosphere of the secondary due to irradiation of the white dwarf, we would expect to see variations in the strength corresponding to the time scale of the orbital period.

In the similar system RR Cae, consisting of a white dwarf of 7 000 K and an M6 or later secondary, a similar effect of a larger EW during eclipse was seen (Bruch 1999). This was contributed to the emission lines being intrinsic to the secondary itself (Bruch 1999). In analogy, we therefore conclude that the Hα emission in DE CVn is also due to activity in the chromosphere of the M dwarf in contrast to being caused by irradiation. Furthermore, we can rule out Hα emission emerging from an accretion disc because of its regular radial velocity profile and the single peaked lines.

If the secondary star is irradiated by the white dwarf, we would also expect a variation of the TiO5 band strength (which is discussed in Sect. 3.3.3) with respect to the orbital period due to heating in the atmosphere of the secondary. We see variations (see Fig. 3.6), but not with the orbital period. Thus also in this case, we conclude that the variations are intrinsic to the secondary.

3.3.7 Flare

During one of the ULTRACAM observing runs (25 May 2003), a flare was observed in all three bands starting at about 23:23 UT. This part of the light curve is shown in Fig. 3.7. The observed part of the flare lasted $\sim$39 minutes. The flare has a complex structure with several peaks close together and a rebrightening during the decay part after the first peaks. Unfortunately the observation ended before DE CVn had returned to the quiescent (pre-flare) luminosity (most clearly seen in the u' band). From the observed count rates
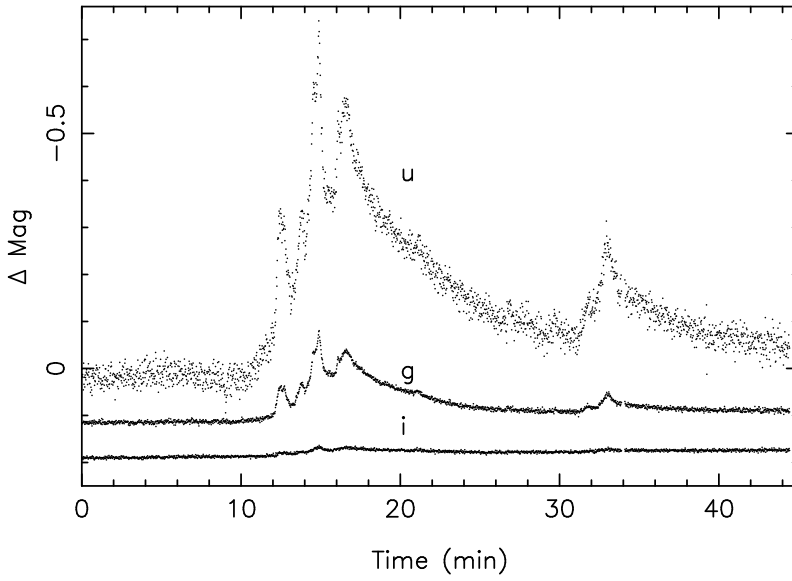
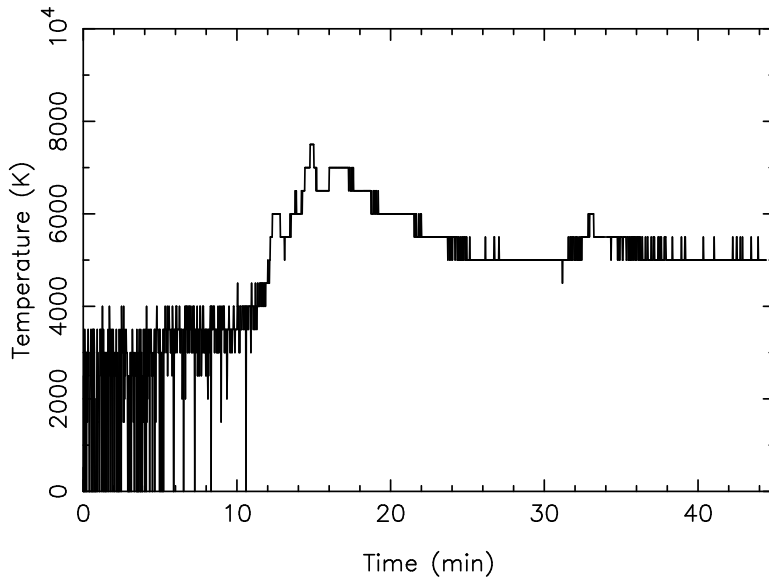Figure 3.7: *A flare of DE CVn observed with ULTRACAM.*

Figure 3.8: *Temperature variation of the flaring area during the flaring period. The flaring area has a radius of $0.038R_\odot$.*

during quiescence and the average count rate during the observed part of the flare, we calculated that DE CVn increased in brightness on average by 20%, 5%, and 1% of the quiescent flux (so white dwarf + red dwarf) during this flaring period in u', g', and i', respectively.

To model the flare, we have taken a blackbody spectrum added to the best-fitted template spectrum (see Sect. 3.3.3). A blackbody might not be a good approximation, but it is used in other analyses of flare stars as well (de Jager et al. 1986, 1989). We have assumed a constant (but not pre-determined) flaring area that is facing us with only temperature variations over time. We have assumed temperatures between 0 and 20 000 K in steps of 200 K and a constant radius for the flaring area.

For every point in time we have taken the three corresponding observed magnitudes. We have derived the u', g', and i' magnitudes for our model by convolving the filter curves with our model spectrum for each temperature. For each point in time we have calculated the reduced χ^2 for each temperature and we have taken the temperature with the lowest reduced χ^2 for this point. After this, the average reduced χ^2 over all the time points was calculated.

We performed this method for several constant flaring areas with radii between $0.010R_\odot$ and $0.053R_\odot$ with steps of $0.001R_\odot$. The result with the lowest average reduced χ^2 has a radius $0.038R_\odot$ and the temperature variations are shown in Fig. 3.8. The area that flares corresponds to 0.9% of the visible stellar disc of the red dwarf.

3.3.8 System parameters

Because spectral features from the white dwarf are not visible we can only measure the radial velocity curve of the secondary star. The inclination of the system is constrained by the eclipses in the photometric light curve. We have fitted the ULTRACAM g' light curve with a simple model light curve that results from using two overlapping circles representing a white dwarf and a red dwarf that is (partly) obscuring the white dwarf (see Van Ham et al. 2007, submitted). It is assumed that the light intensity is proportional to the visible part of the white dwarf. We have used the light curve in counts scaled to range between 1 (out of eclipse) and 0 (in eclipse). This way we only derive the radii of the two stars with respect to the orbital separation (a, i.e. R_{WD}/a and R_{RD}/a).

Limb darkening of the white dwarf could play a role. When we include limb darkening in our model the white dwarf radius increased by a few per cent. This is negligible with respect to the uncertainty in the inclination so therefore we have neglected the effect of limb darkening in our method.

From our model we obtain the combinations of the white dwarf and red dwarf radii with respect to the orbital separation for inclinations between $75°$ and $90°$ with a step size of $1°$. At lower inclinations we find that the red dwarf either fills its Roche lobe or is larger than its Roche lobe. As there is no evidence for mass transfer in the system, the red dwarf must be smaller than its Roche lobe. The reduced χ^2 for these fits to the eclipse light curve are not significantly different, illustrating the fact that another constraint on the system is required for a unique solution.

The semi-amplitude of the radial velocity variations of the secondary is derived from the spectra in Sect. 3.3.5. The spectral type of the secondary is determined in Sect. 3.3.3 by fitting model spectra to the spectrum of DE CVn. These parameters are taken as known input parameters in our two-circle model.

From the spectral type of the secondary and assuming zero-age main-sequence masses and temperatures, the mass of the red dwarf should be between 0.3 and $0.5 M_\odot$ (see, e.g., Kirkpatrick et al. 1991). For every possible inclination, we input the mass of the secondary in steps of $0.01 M_\odot$ between these values. Furthermore, we use Kepler's third law and the mass-radius relation for white dwarfs from Eggleton as quoted by Verbunt & Rappaport (1988):

$$R_{\mathrm{WD}} = 0.0114 \cdot \left(\left(\frac{M_{\mathrm{WD}}}{M_{\mathrm{CH}}} \right)^{-\frac{2}{3}} - \left(\frac{M_{\mathrm{WD}}}{M_{\mathrm{CH}}} \right)^{\frac{2}{3}} \right)^{\frac{1}{2}} \times$$

$$\left(1 + 3.5 \cdot \left(\frac{M_{\mathrm{WD}}}{M_{\mathrm{P}}} \right)^{-\frac{2}{3}} + \left(\frac{M_{\mathrm{WD}}}{M_{\mathrm{P}}} \right)^{-1} \right)^{-\frac{2}{3}}, \qquad (3.4)$$

where R_{WD} is in solar radii, M_{WD} in solar masses, $M_{\mathrm{CH}} = 1.44 M_\odot$, and M_{P} is a constant whose numerical value is $0.00057 M_\odot$.

For every inclination we obtain a value of R_{WD}/a from the eclipse fitting. By combining Kepler's third law and Eq. (3.4) we derive the mass and radius of the white dwarf for every inclination and secondary mass. With the radius of the white dwarf and the result of the eclipse fitting we derive the orbital

separation and the radius of the secondary star.

By assuming a circular orbit, which is justified by the radial velocity curve, we can constrain the inclination by using the mass function given in Eq. (3.5) to derive the semi-amplitude of the red dwarf for every inclination and secondary mass, and the system parameters derived from the procedure described above. With these parameters and assuming a circular orbit we can use the following function for the mass function:

$$\frac{M_1^3 \sin^3 i}{(M_2 + M_1)^2} = \left(1.0361 \times 10^{-7}\right) \; K_2^3 \; P \tag{3.5}$$

with $M_{1,2}$ in $M_\odot$, K_2 in km s^{-1} and P in days.

We take a 3σ uncertainty on the measured semi-amplitude of the radial velocity variation of the secondary and compared these with the semi-amplitudes for each possible solution. We selected only those solutions that satisfied the radial velocity criterion. This constrains the inclination of DE CVn to $\geq 82°$. The combined radial velocity and eclipse constraints lead to system parameters where the mass of the white dwarf is between 0.48 and $0.65 M_\odot$ and the radius between 0.0117 and $0.0140 R_\odot$. The red dwarf has a mass between 0.30 and $0.50 M_\odot$ and a radius between 0.36 and $0.51 R_\odot$. The orbital separation of the system is between 2.00 and $2.25 R_\odot$.

By comparing our white dwarf radii with the corresponding masses for carbon core or oxygen core white dwarfs from Panei et al. (2000), our minimum and maximum mass for the white dwarf would be at most 5% larger. Furthermore, all the red dwarf masses that we used in deriving the system parameters are possible solutions. In our ULTRACAM data set, we see hints for small out-of-eclipse light curve variations and variations between the different observations, but this data set does not cover the complete orbital period. In our eclipse fitting procedure, we only use the section between phases -0.035 and 0.04, so here the effect of these variations can be neglected.

3.3.9   Space velocity and distance

The fitting procedure described in Sect. 3.3.3 also determines a distance to DE CVn of 28 ± 1 pc. The proper motion is known as well (see Sect. 3.1), and the systemic velocity is derived from fitting the radial velocity curve in Sect. 3.3.5. Johnson & Soderblom (1987) give the equations to calculate

the space velocities (U, V, W) and we use $(U_\odot, V_\odot, W_\odot) = (10.00 \pm 0.36, 5.25 \pm 0.62, 7.17 \pm 0.38)$ in km s^{-1} as the velocity of the Sun with respect to the local standard of rest as given by Dehnen & Binney (1998). The space velocities of DE CVn, defined as

$$(u, v, w) = (U, V, W) - (U_\odot, V_\odot, W_\odot) \tag{3.6}$$

are $(u, v, w) = (-15.8 \pm 0.4, -40.7 \pm 1.4, -3.3 \pm 2.8)$ km s^{-1}. U is defined as positive in the direction of the galactic center, V is positive in the direction of the galactic rotation, and W is positive in the direction of the galactic North Pole. The derived space velocities for DE CVn are consistent with being a thin disc object (Fuhrmann 2004).

3.4 Discussion and conclusions

3.4.1 Binary parameters

We have analysed various spectroscopic and photometric observations of the eclipsing binary DE CVn. The light curves show total eclipses of the primary by the secondary star. The low resolution average ISIS spectrum is fit with model composite spectra to determine the spectral type of the M dwarf and the temperature of the white dwarf. The best fit is derived for an M3V secondary star and the temperature of the white dwarf (with $\log g = 7.5$) of $8\,000 \pm 1\,000$ K. This is consistent with the temperature estimates derived from the eclipse depths (Sect. 3.3.2) and difference spectrum (Sect. 3.3.3), and the spectral type from the TiO5-index (Sect. 3.3.3).

From the echelle spectra taken with the TLS we have obtained radial velocity curves of Hα, Hβ, and Hγ, and also TiO absorption bands from the MDM spectra. These curves show a semi-amplitude for the secondary of 166 ± 4 km s^{-1}. Combining the eclipse constraints with the radial velocity amplitude results in a set of solutions satisfying the constraints as described in Sect. 3.3.8. Determining the most likely value with an uncertainty on it is very complex. Due to the interdependency of the relations used, calculating the uncertainties is not straightforward. As an example, we show the histogram of the possible solutions for the white dwarf mass in Fig. 3.9, which shows an asymmetrical distribution. The average or the mean does not coincide with the peak of the distribution. We take the most likely value as the highest point in the distribution. To determine the uncertainty on the
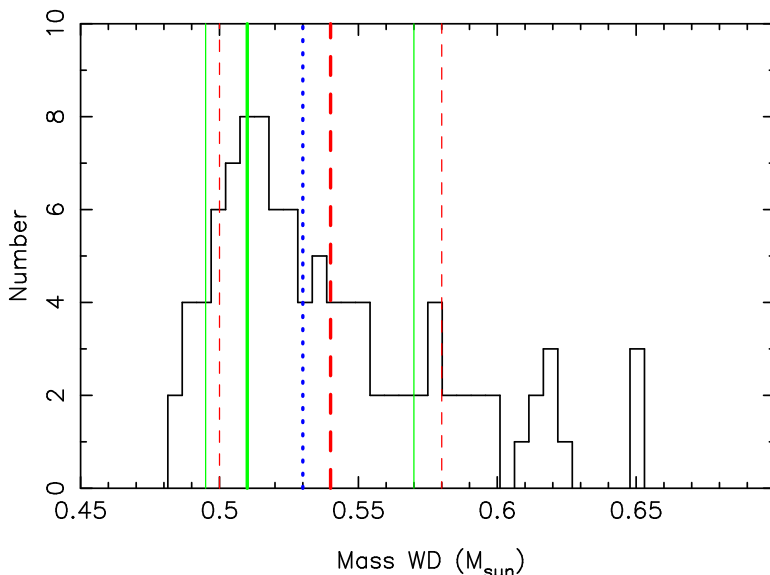
Figure 3.9: *Distribution of the possible solutions for the mass of the white dwarf. The thick solid line (green/grey) is the most likely value that we have used. The thin solid lines (green/grey) are the values between which 68% of the possible solutions are located. The thick dashed line (red/darker grey) is the average value with the standard deviation in thin dashed lines (red/darker grey). The median of the distribution is shown as the dotted line (blue/dark grey).*

most likely value, we have taken the value for which 68% of the solutions are enclosed around the most likely value. The difference between these values is taken as our uncertainty. We have done this separately for each side of the distribution. For the white dwarf mass and radius this resulted in $0.51^{+0.06}_{-0.02}$ $M_\odot$ and $0.0136^{+0.0008}_{-0.0002}$ $R_\odot$. In the same way, the distributions of the red dwarf mass and radius result in 0.41 ± 0.06 $M_\odot$ and $0.37^{+0.06}_{-0.007}$ $R_\odot$, respectively. The orbital separation is $2.07^{+0.09}_{-0.04}$ $R_\odot$ and the inclination is 86^{+3}_{-2} °. These most likely values are consistent with each other within the uncertainties.

3.4.2 Progenitor

From the current small orbital separation we conclude that there was most probably a CE phase in the past in which the orbit has shrunken signifi-

Table 3.6: *Parameters of different white dwarf progenitors at the time the core mass reaches 0.52$M_\odot$.*

M_0 ($M_\odot$) (1)	M_i ($M_\odot$) (2)	R_i ($R_\odot$) (3)	t_{evol} (yr) (4)	a_i ($R_\odot$) (5)	P_i (d) (6)	$\alpha_{CE}\lambda$ (7)	t_{tot} (yr) (8)
1.051	0.923	231.165	$6.51 \cdot 10^9$	513.052	1166.530	0.03	$2.61 \cdot 10^{10}$
1.191	1.085	224.726	$4.95 \cdot 10^9$	483.386	1007.611	0.05	$2.45 \cdot 10^{10}$
1.319	1.230	218.584	$3.87 \cdot 10^9$	459.140	890.428	0.08	$2.34 \cdot 10^{10}$
1.439	1.365	212.881	$3.10 \cdot 10^9$	438.689	799.406	0.11	$2.27 \cdot 10^{10}$
1.555	1.494	207.045	$2.54 \cdot 10^9$	419.770	722.411	0.14	$2.21 \cdot 10^{10}$
3.400	3.399	40.222	$2.74 \cdot 10^8$	71.425	35.849	5.83	$1.99 \cdot 10^{10}$

Notes: Col. (1): initial mass of the main-sequence progenitor; Cols. (2) and (3): mass and radius of the star when it has reached the required core mass. Col. (4): time between the birth of the binary and the start of the CE phase; Cols. (5) and (6): initial orbital separation and initial orbital period; Col. (7): fraction of the orbital period used for ejection of the CE, where λ is a numerical value dependent on the structure of the star; Col. (8): time from a main-sequence binary to a CV.

cantly. At the onset of the CE phase, the initially more massive star has evolved to a star with giant dimensions. We assume that the core of the giant star at the start of the CE phase had the same mass as the present-day white dwarf. This can be used to reconstruct the evolution of DE CVn to find the possible progenitors.

To do this we take single main-sequence stars with masses of 1 to $8M_\odot$ in steps of $0.1M_\odot$. We evolve these stars with the method described in Hurley et al. (2000). When the core mass (M_c) of the stars has reached the mass of the white dwarf that we observe in DE CVn ($0.51M_\odot$), the evolution is stopped. Then we check if the radius of the star at this point (R_i) corresponds to the largest radius during the evolution up to this point. We assume that the star fills its Roche lobe in the giant phase.

The most likely mass of the white dwarf of DE CVn falls in a mass range where many progenitor stars cannot fill their Roche lobe with this core mass. The reason is that on the first giant branch their core grows to $\sim 0.48M_\odot$, when the helium flash happens. Then the star contracts while the core mass still increases. When the star expands again to ascend the asymptotic giant branch (AGB), the core mass has become larger than the most likely white dwarf mass in DE CVn. However, this is very sensitive to the core mass: for a core mass of $0.51M_\odot$ we find only one progenitor, while for $0.52M_\odot$ we find six. We therefore use $0.52M_\odot$, as a compromise between staying close to the most likely mass yet allowing as many progenitors as are allowed by the inferred mass range.

The possible progenitors are given in Table 3.6. The first three columns in this table are the initial mass of the main-sequence progenitor of the white dwarf (M_0) and the mass and radius of the star at the time the evolution is stopped (M_i and R_i). The evolution time of the star until this point is given as $t_{\rm evol}$. The first five possibilities are stars that reach the required core mass while on the AGB, while the last one is peculiar: it reached the required core mass when it had a non-degenerate core. If the progenitor were such a star, the system would have come out of the common-envelope phase as a helium-burning star (most likely observable as a subdwarf B star) with a low-mass companion. Only after most helium was burned to carbon and oxygen would the star have turned into a white dwarf.

There are no possible progenitors with initial masses between 1.6–$3.4M_\odot$. For mass $> 1.6M_\odot$, the core mass of the giant on the red giant branch (RGB) has not yet grown to the required mass. After the RGB phase, the

star contracts again, while the core mass is growing. When the star reaches the AGB phase, the core mass is already larger than the required mass. This results in no possible progenitor star. At the moment of sufficient core mass, the star needs to be larger than any time previously in its evolution, otherwise the star would have started Roche lobe overflow earlier in its evolution when the core mass was not yet massive enough. For stars $>$ $3.4M_\odot$ the core of the giant at the start of the RGB phase is already larger than the required core mass, leaving no possible progenitor for the present-day white dwarf. The progenitor with an initial mass of $3.4M_\odot$ is just on the edge of being a possible progenitor for the present-day white dwarf in DE CVn.

3.4.3   Common-envelope phase

We assume that a possible progenitor fills its Roche lobe at the start of the CE phase. By using the formula for the Roche lobe of Eggleton (1983)

$$\frac{R_{\mathrm{L}}}{a} = \frac{0.49q^{\frac{2}{3}}}{0.6q^{\frac{2}{3}} + \ln(1 + q^{\frac{1}{3}})} \tag{3.7}$$

(with $q = M_i/M_2$), we can calculate the orbital separation (a_i) (and thus the orbital period P_i) at the moment the evolution was stopped. These values are given in Table 3.6 as well. From the initial orbital period (P_i, Table 3.6) and the present-day orbital period, we note that a large orbital shrinkage has taken place. Together with the rather extreme initial mass ratios, this implies that DE CVn went through a common-envelope phase during its evolution.

We take the parameters of the giants derived above as the ones at the start of the common-envelope phase. With the use of (de Kool et al. 1987)

$$\frac{GM_i(M_i - M_c)}{R_i} = \alpha_{\mathrm{CE}}\lambda\left(\frac{GM_cM_2}{2a_f} - \frac{GM_iM_2}{2a_i}\right), \tag{3.8}$$

we calculate $\alpha_{\mathrm{CE}}\lambda$, where λ is a numerical value dependent on the structure of the star and α_{CE} the fraction of the orbital energy that is used for ejection of the common envelope (de Kool 1992), for every possible progenitor. α_{CE} is usually $0 \leq \alpha_{\mathrm{CE}} \leq 1$, but for double white dwarfs it is found to be ≥ 1

(Nelemans & Tout 2005). The $\alpha_{\mathrm{CE}}\lambda$ values for the possible progenitor stars are given in Table 3.6 as well.

The most massive progenitor has $\alpha_{\mathrm{CE}}\lambda$ of 5.83. Dewi & Tauris (2000) give λ values as a function of the radius of the giant for stars with $M \geq 3M_\odot$. From their table we conclude that for our possible progenitor of mass $3.4M_\odot$ λ is around 0.6–0.9, indicating $\alpha_{\mathrm{CE}} \gtrsim 6$, which is very unlikely. Therefore we rule out such a star as the possible progenitor.

The other possible progenitors have $\alpha_{\mathrm{CE}}\lambda < 1$, indicating a rather inefficient ejection of the CE (e.g., a large fraction of the binding energy is not used for ejection of the CE). These values are in agreement with the values found for other white dwarf–red dwarf binaries (e.g., Nelemans & Tout 2005; Morales-Rueda et al. 2005), and we conclude that the progenitor star of the present-day white dwarf was a main-sequence star with $M \leq 1.6M_\odot$.

3.4.4 Time scales

Now that we can reconstruct the evolution of DE CVn we can determine the corresponding time scales. From the possible progenitors of the white dwarf we find that the time it took before the CE phase started is 2.5–6.5×10^9 years. The temperature of the white dwarf is $8\,000 \pm 1\,000$ K. From the cooling tracks of Wood (1995) as shown in Fig. 4 of Schreiber & Gänsicke (2003), we can determine a cooling age (t_{cool}) of the white dwarf of $\sim 8 \times 10^8$ years. The current age of the system is therefore 3.3–7.3×10^9 years.

Due to angular momentum loss, the system will evolve towards a semidetached cataclysmic variable (CV) phase. To determine the time that it will take for DE CVn to become a semi-detached binary, we first need to know the orbital period at which mass transfer starts (P_{sd}). This period follows from the Roche geometry and Kepler's third law:

$$P_{\mathrm{sd}} = 2\pi \left(\frac{R_2^3}{GM_2\left(1 + \frac{M_1}{M_2}\right)\left(\frac{R_{\mathrm{L}_2}}{a}\right)^3} \right)^{0.5}. \tag{3.9}$$

For DE CVn we derive an orbital period at the start of mass transfer of 3 hours.

The orbital period will shrink due to loss of orbital angular momentum. For low-mass stars it is often assumed that the dominant mechanism is (disrupted) magnetic breaking (Verbunt & Zwaan 1981; King 1988). In short,

disrupted magnetic breaking occurs in a close binary when the tides force the secondary star to be co-rotating with the binary, while magnetic fields in the secondary force the stellar wind to co-rotate with the secondary star. When this exerts a spin-down torque on the secondary star, it must extract angular momentum from the binary orbit. At a mass of $\sim 0.3 M_\odot$, the secondary becomes fully convective and therefore loses its dynamo (or at least changes it) so that magnetic breaking is no longer the dominant source of angular momentum loss.

By assuming that the angular momentum loss is due to disrupted magnetic braking only until the secondary becomes fully convective at a secondary mass of at least $0.3 M_\odot$, the time it will take before mass transfer starts is (Schreiber & Gänsicke 2003):

$$t_{\rm sd}^2 = \frac{2.63 \cdot 10^{29} G^{\frac{2}{3}} M_1}{(2\pi)^{\frac{10}{3}} (M_1 + M_2)^{\frac{1}{3}}} R_2^{-2} \times (P_{\rm orb}^{\frac{10}{3}} - P_{\rm sd}^{\frac{10}{3}}), \qquad (3.10)$$

where M_1 and M_2 are in $M_\odot$ and R_2 in $R_\odot$. This corresponds to a time of 1.9×10^{10} years before DE CVn becomes a CV, which is just longer than the Hubble time. Systems such as DE CVn will not contribute to the current sample of CVs, unless the loss of angular momentum in the current detached white dwarf–red dwarf phase is much higher than that given by magnetic braking alone (see, e.g., Brinkworth et al. 2006, where an angular momentum loss mechanism ~ 100 times greater in strength than the currently accepted value seems to be required to explain the rate of period decrease in NN Ser).

Acknowledgements

Chapter 4

White dwarf–red dwarf binaries in the Sloan Digital Sky Survey I: Sample definition[1]

T. Augusteijn, R. Greimel, E.J.M. van den Besselaar
P.J. Groot, L. Morales-Rueda

Abstract

A significant fraction of binary stars consisting of a white dwarf and a low-mass main-sequence star (red dwarf) are expected to be close binaries that are the end product of common-envelope (CE) evolution. To gain a better understanding of CE evolution we want to study white dwarf–red dwarf binaries. For this it is fundamental to establish a well defined sample. To reduce contamination by more distant sources, such as quasars, we have selected candidate white dwarf–red dwarf binaries from the catalogue of proper motion stars drawn from the intersection of the Sloan Digital Sky Survey (SDSS) and the USNO-B1.0 catalogue. To separate single from binary sources, and to cut-out spurious sources we define selection criteria based on a combination of the $(u - g)$, $(g - r)$ and $(r - i)$ colours. We evaluate and discuss the selection criteria on the basis of the publicly available

SDSS spectra, and on the basis of the predicted colours of white dwarf–red dwarf binaries. We define a sample of 651 binary candidates. However, we find that for r magnitudes brighter than $\sim$16.5 the proper motion catalogue is heavily contaminated with sources that have incorrect colour due to the r magnitudes being relatively too faint, most likely due to saturation effects. We show that the level of contamination can be reduced by either excluding sources brighter than $r = 16.5$ mag, or by excluding sources bluer than $(u-g) = -0.5$ or $(g-r) = -0.6$ and brighter than $r = 16.0$ mag. We expect $\sim$85% of the remaining sources to be genuine white dwarf–red dwarf binaries. We estimate that we miss $\sim$5-10% of all white dwarf–red dwarf binaries covered by our selection criteria.

4.1   Introduction

Most stars in the Galaxy are part of a binary or a multiple system (Abt 1983). In many binaries the orbital separation is sufficiently small ($P_{\mathrm{orb}} <$ few $\times$ 100 days) such that the expanding envelope of an evolving star will engulf its companion creating a common-envelope (CE). Due to friction the binary components will lose angular momentum and the core of the giant and the companion will spiral in toward each other. Eventually, the envelope is ejected, and the system will reappear as a binary system consisting of the original secondary and the core of the primary (e.g. Paczyński 1976). The removal of its envelope will affect the evolution of the primary, limiting the mass of its core. In most cases the core will appear as a hot subdwarf which will subsequently cool to a white dwarf. However, the detailed physics of the CE phase (e.g., the efficiency of energy transport through the envelope, the distribution of mass ejection [e.g., spherical or in the plane], possible additional energy sources [e.g., from accretion or recombination], etc.; see e.g., Iben & Livio (1993)) is not well understood, and there are large uncertainties in the precise outcome of the CE phase.

In general, one would expect that there are many binaries which contain a white dwarf and a low-mass main-sequence star (red dwarf), a significant fraction of which are expected to have evolved through a CE phase and should be close binaries (see, e.g., de Kool & Ritter 1993). The white dwarf
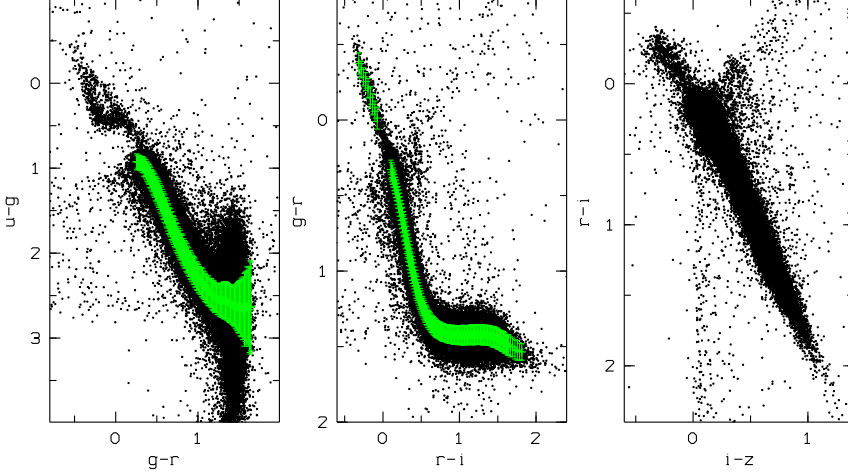
Figure 4.1: *The $(u-g)$ vs. $(g-r)$, the $(g-r)$ vs $(r-i)$ and the $(r-i)$ vs $(i-z)$ colour-colour diagrams for every 3rd source in the SDSS $\cap$ USNO-B proper motion catalogue Gould & Kollmeier (2004). In the $(u-g)$ vs $(g-r)$ and $(g-r)$ vs $(r-i)$ colour-colour diagrams the average position and width of the main locus of stars is indicated (see Sect. 4.4).*

and red dwarf in these binaries are not expected to have changed much since the CE phase, and the components have well defined properties and are well understood. Therefore, the population of white dwarf–red dwarf binaries provides an ideal sample for testing models for CE evolution through the study of the properties of the population (e.g., number density, orbital period distribution) and the individual components (e.g., masses, surface temperatures).

Currently there are several hundred detached white dwarf–red dwarf binaries known (Silvestri et al. 2006, and references therein), and for $\sim$100 sources the binary period has been determined (Ritter & Kolb 2003). The sample of white dwarf–red dwarf binaries is very inhomogeneous, but most

commonly white dwarfs selected on their (E)UV brightness were searched for a red (or infrared) excess (Wachter et al. 2003; Green et al. 2000). This leads to a strong selection towards young, hot white dwarfs and relatively early type secondaries. E.g., among the binaries consisting of either a white dwarf or a white dwarf precursor primary and a red dwarf which have a known orbital period, more than half contain a (hot) sub-dwarf (Ritter & Kolb 2003), while one would expect the intrinsic population to be dominated by cooler white dwarfs.

White dwarf–red dwarf binaries are expected to show a large range in (photometric) properties, depending mostly on the temperature of the white dwarf and the spectral type of the red dwarf. In general, the white dwarf will dominate in the blue and the red dwarf in the red but the overall spectral energy distribution can vary strongly depending on the characteristics of the components. To be able to both detect white dwarf–red dwarf binaries with a hot white dwarf and a late-type red dwarf, and with a cool white dwarf and an early-type red dwarf one needs a broad coverage in wavelength. This is complicated by the fact that white dwarf–red dwarf binaries are intrinsically faint objects which makes it hard to distinguish both components if there is a large difference in luminosity between them.

The Sloan Digital Sky Survey (SDSS; York et al. 2000) is potentially a powerful tool to detect large numbers of white dwarf–red dwarf binaries as it provides deep ($r < 22.3$ mag), accurate photometry in five pass-bands (u, g, r, i and z; Fukugita et al. 1996), covering a large range in wavelength. However, quasars cover a similar range in colours as white dwarf–red dwarf binaries (see, e.g., Fan 1999). It is not simple to separate these populations on colours alone, and any sample of white dwarf–red dwarf binaries will be highly contaminated. Here we present a sample of white dwarf–red dwarf binary candidates selected from the catalogue of proper motion stars (Gould & Kollmeier 2004) drawn from the intersection of the SDSS and the USNO-B1.0 catalogue (Monet et al. 2003). Using this catalogue, the contamination by more distance sources (quasars, binary giants) should be small. In addition, we have defined a set of refined colour limits to include as much as possible all types of white dwarf–red dwarf binaries that are covered by the SDSS. The aim of this paper is to provide a well defined sample of white dwarf–red dwarf binaries drawn from the SDSS. Such a sample is intended as, and is essential for, a proper study of common-envelope evolution.
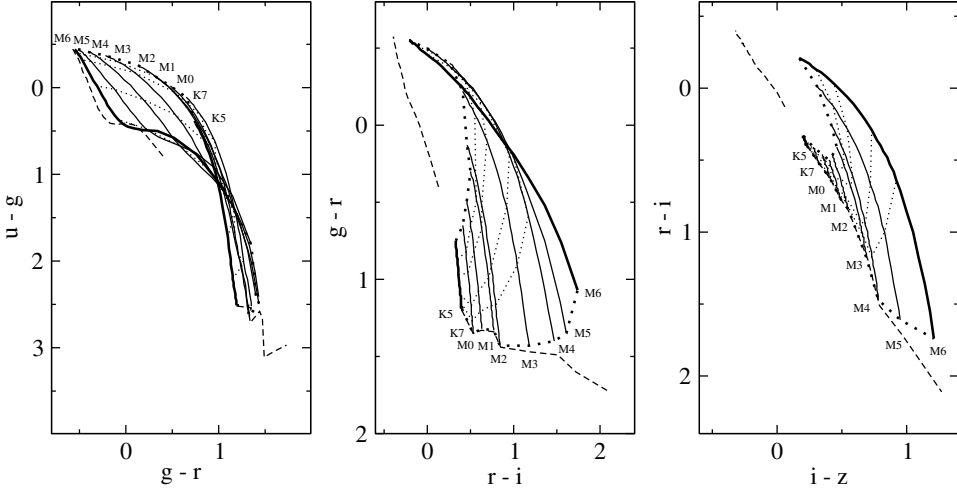
Figure 4.2: *The expected position of white dwarf–red dwarf binaries with a DA white dwarf in the different CCDs. The different solid lines correspond to binaries with a specific spectral type of the secondary as indicated in the figure. The surface gravity of the white dwarfs is fixed at $\log g = 8.0$. The dotted lines correspond to binaries with the same temperature white dwarfs, where we show (from top to bottom) effective temperatures of 80 000, 50 000, 34 000, 22 000, 14 000 and 6 000 K, respectively. The dashed line in the upper left part of each panel indicates the position of single white dwarfs and the dashed line in the lower right part of each panel indicates the position of single red dwarfs.*

Below we discuss and evaluate the selection criteria on the basis of SDSS spectra of the sources, and on the basis of the predicted colours of white dwarf–red dwarf binaries. We will show that the contamination of the final sample is minimal while we exclude very few genuine sources. In two accompanying papers we present a more detailed analysis of the sources in our sample with existing SDSS spectra (van den Besselaar et al. 2007a, hereafter Chapter 5), and of the whole photometric sample (van den Besselaar et al. 2007b, hereafter Chapter 6).

4.2   The SDSS ∩ USNO-B proper motion catalogue

The SDSS ∩ USNO-B proper motion catalogue (Gould & Kollmeier 2004) consists of 390 000 objects with a proper motion $\mu \geq$20 mas yr^{-1} and magnitudes $r \leq 20$. In Fig. 4.1 we present the $(u - g)$ vs $(g - r)$, the $(g - r)$ vs $(r - i)$ and the $(r - i)$ vs $(i - z)$ colour-colour diagrams (CCDs) of the sources in the catalogue. The main stellar locus in all the diagrams is the main-sequence. In the $(u - g)$ vs $(g - r)$ CCD the separate group of sources in the top-left are mostly single white dwarfs. In the $(g - r)$ vs $(r - i)$ and the $(r - i)$ vs $(i - z)$ CCDs these single white dwarfs form the extension of the main-sequence in the top-left, while the sources below the main-sequence in the $(g - r)$ vs $(r - i)$ CCD are most likely dwarf carbon stars (Margon et al. 2002). The sources above and to the right of the main stellar locus are expected to be white dwarf–red dwarf binaries. The precise position in these diagrams depends on the combination of the temperature of the white dwarf and the spectral type of the red dwarf.

4.3   White dwarf–red dwarf binaries

To explore the distribution of white dwarf–red dwarf binaries across the CCDs we have investigated the expected position of such binaries. For this we need the absolute magnitudes of the components in the binary in the different SDSS passbands to be able to combine their contributions and derive the expected colours. Here we have used values for single white dwarfs and single red dwarfs. This assumes that both components in the binary have the same brightness and colour as a single star of identical type, which should give a good representation for non-interacting binaries. The objective of this is to determine the expected brightness and colour of a white dwarf–red dwarf binary as a function of temperature and surface gravity (and chemical composition of the atmosphere) of the white dwarf, and the spectral type of the red dwarf.

4.3.1   Binary components

To derive the absolute magnitudes for white dwarfs as a function of their properties, specifically their effective temperature and surface gravity, we have used a model grid of H-rich (DA) and He-rich (DB) white dwarfs
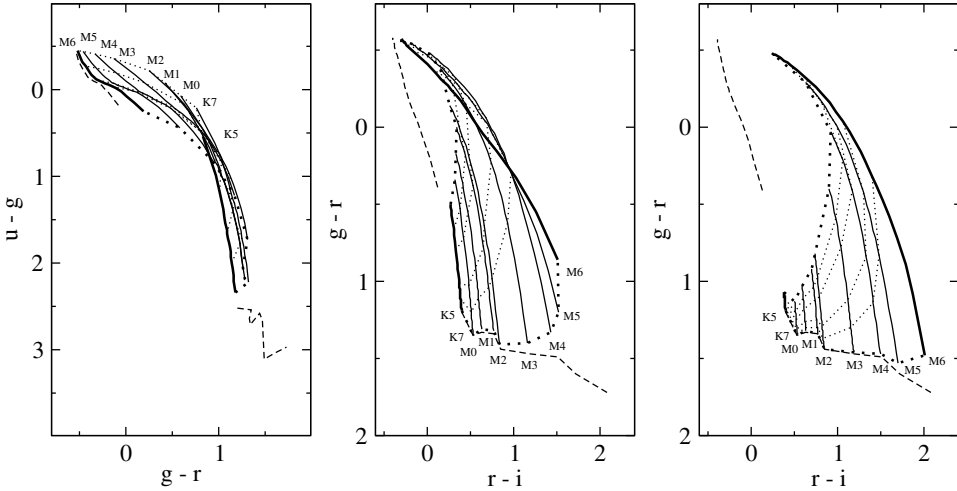
Figure 4.3: *The middle and right panel show the $(g-r)$ vs $(r-i)$ CCDs in the same way as in Fig. 4.2, but now for white dwarf–red dwarf binaries with a DA white dwarf with $\log g = 7.0$ (middle panel), and $\log g = 9.0$ (right panel). The left panel shows the $(u-g)$ vs $(g-r)$ CCD with the expected position of white dwarf–red dwarf binaries with a DB white dwarf with $\log g = 8.0$. The dotted lines correspond to binaries with the same temperature white dwarfs, where in this case we show (from top to bottom) effective temperatures of $50\,000$, $34\,000$, $22\,000$, $15\,000$ and $10\,000$ K, respectively.*

kindly made available to us by Detlev Koester (see for details Chapter 5). To derive the absolute magnitudes for the red dwarfs we have used the flux calibrated spectra provided by (Pickles 1998).

We specifically use these spectra as they were also used in the analysis of the spectra in our sample (Chapter 5). To convert the Eddington fluxes of the WD models to observed fluxes (in erg s^{-1} cm^{-1} Å^{-1}) we have used the mass-gravity relations of (Napiwotzki et al. 2005). For the scaling of the red dwarf spectra we used the filter response curve and the absolute V magnitude provided by Pickles (1998), and the zero point flux for the V filter provided by (Bessell et al. 1998). Absolute magnitudes for the SDSS filters were obtained using the filter response curves provided on the SDSS

web page[2] where we applied corrections of $+0.04$ and -0.02 to the magnitudes in the u and z filter, respectively, to convert the resulting "true" AB magnitudes to SDSS catalogue magnitudes[3].

4.3.2   Binary colours

From the absolute magnitudes defined above for white dwarfs and red dwarfs it is straightforward to derive the expected colours of a white dwarf–red dwarf binary which can be compared to the CCDs for the sources from the proper motion catalogue. In Fig. 4.2 we present the resulting CCDs for white dwarf–red dwarf binaries with a DA white dwarf for a range in spectral type of red dwarfs (K5V to M6V), and a range in white dwarf temperatures (6 000–80 000 K) for a fixed surface gravity of $\log g = 8.0$. Also indicated in the figure are the colours we derived for single white dwarfs and single red dwarfs.

Comparing Fig. 4.2 to the CCDs of the sources in the catalogue presented in Fig. 4.1 it is clear that, except for binaries with the latest types of red dwarfs ($\gtrsim$M3), it is not possible to separate white dwarf–red dwarf binaries from the main locus of stars in the $(r-i)$ vs $(i-z)$ CCD. However, except for the earliest type of red dwarfs ($\lesssim$K7), the $(g-r)$ vs $(r-i)$ CCD does provide a clear separation of the white dwarf–red dwarf binaries from the main locus of stars. White dwarf–red dwarf binaries are also well separated from single red dwarfs (even for the earliest type of red dwarfs if the temperature of the white dwarf is $\gtrsim$15 000 K) in the $(u-g)$ vs $(g-r)$ CCD, but for binaries with late-type red dwarfs ($\gtrsim$M5) the colours overlap with those of single white dwarfs. The tracks with the range in properties for the white dwarfs and red dwarfs presented in Fig. 4.2 provide distinct areas in the CCDs where we expect to find white dwarf–red dwarf binaries. One can actually discern the population of white dwarf–red dwarf binaries in both the $(u-g)$ vs $(g-r)$ and $(g-r)$ vs $(r-i)$ CCDs in Fig. 4.1 (see also Smolčić et al. 2004). However, looking at Fig. 4.1 it is also clear that there is a lot of contamination of likely spurious sources in the data of the catalogue. These spurious sources are those radiating from, or parallel to the main locus of stars in the different CCDs.

We have also investigated the effect of varying the surface gravity of the

---

[2]http://www.sdss.org/dr5/instruments/imager/index.html#filters
[3]http://www.sdss.org/dr5/algorithms/fluxcal.html

white dwarf on the expected colours of a white dwarf–red dwarf binary. In Fig. 4.3 we present the $(g - r)$ vs $(r - i)$ CCDs for white dwarf–red dwarf binaries with a DA white dwarf and a surface gravity of $\log g = 7.0$ and $\log g = 9.0$. As expected, the tracks for a given spectral type of the red dwarf will move to the upper left for $\log g = 7.0$, i.e., a bigger white dwarf, as the contribution of the white dwarf to the overall emission from the binary will be larger for the same effective temperature, while for $\log g = 9.0$ the tracks will move to the lower right. In general, one would expect white dwarf–red dwarf binaries which are bluest in $(r - i)$ to contain a low surface gravity white dwarf, while the reddest binaries in $(r - i)$ are expected to contain a high surface gravity white dwarf.

With the exception of the $(u - g)$ colour, due to the fact that there is no Balmer jump in DB white dwarfs, the magnitude and colours for DA and DB white dwarfs are very similar. In Fig. 4.3 we also present the resulting CCDs for white dwarf–red dwarf binaries with a DB white dwarf for a range in white dwarf temperatures ($10\,000$–$50\,000$ K) and a fixed surface gravity of $\log g = 8.0$. Although the tracks have a somewhat different shape than those of white dwarf–red dwarf binaries with a DA white dwarf there is not much qualitative difference. The tracks in the other CCDs for white dwarf–red dwarf binaries with a DB white dwarf are virtually the same as the tracks with DA white dwarfs (see Fig. 4.2).

In general, we can conclude from Figs. 4.2 and 4.3 that for a large range of surface gravities and temperatures for both DA and DB white dwarfs, and a large range of spectral types for the red dwarf, white dwarf–red dwarf binaries are well separated from the main locus of stars in both the $(u - g)$ vs $(g - r)$ and $(g - r)$ vs $(r - i)$ CCDs.

4.4 The main stellar locus

The main problem in defining the sample of high proper motion white dwarf–red dwarf binaries is to separate the candidate binaries from single stars and to filter out spurious sources in a well-defined, objective way. From the results presented in the previous section we can conclude that white dwarf–red dwarf binaries can in principle be separated from single main-sequence stars and single white dwarfs in a $(g - r)$ vs $(r - i)$ CCD. On the other hand, these binaries can be separated from single main-sequence stars in a $(u - g)$

vs $(g - r)$ CCD, but there is a significant overlap between the expected position of white dwarf–red dwarf binaries and that of single white dwarfs. The $(r - i)$ vs $(i - z)$ CCD can not be used to find white dwarf–red dwarf binaries as there is a large overlap between their expected position in this CCDs and the main stellar locus. As a first step we will define the position of the main stellar locus in each CCD by calculating the average value of $(u - g)$ as a function of $(g - r)$, and of $(g - r)$ as a function of $(r - i)$, respectively. To do this, the data were binned as a function of $(g - r)$ in the $(u - g)$ vs $(g - r)$ CCD, and as a function of $(r - i)$ in the $(g - r)$ vs $(r - i)$ CCD.

In the $(u - g)$ vs $(g - r)$ CCD the white dwarfs are well separated from the main-sequence but show a more complicated structure as DA and DB white dwarfs have a different distribution. Here we only define the position of the main locus of main-sequence stars limited over the colour range $(g - r)$=0.25 to 1.65 and using a bin-size of 0.01 mag. The main stellar locus in the $(g - r)$ vs $(r - i)$ CCD consists mainly of white dwarfs for $(g - r) \leq 0.2$, and main-sequence stars for redder colours. To define the main stellar locus, we have used for the main-sequence stars a bin-size of 0.01 mag over the range $(r - i)$=0.10 to 1.65 and, as the number of sources becomes smaller, a bin size of 0.03 mag over the range $(r - i)$=1.65 to 1.83. As the number of objects in the part of the main locus dominated by white dwarfs is small we have used a bin size of 0.03 mag over the range $(r - i)$=−0.33 to −0.06. To remove any extreme outliers we have only considered sources that have $-1 < (u - g) < 6$, $-0.7 < (g - r) < 1.8$, $(r - i) < 2.4$ and $(g - r) < \frac{20}{9} \times (r - i) + 0.5$ (the latter to exclude the relatively many sources that are just below the top part of the main locus in the $(g - r)$ vs $(r - i)$ CCD).

To define the location of the main stellar locus and exclude as much as possible the contribution from stars that are not on the locus, we have tried various iterative schemes to determine the average value in each bin along the abscissa in each CCD. As the catalogue is dominated by stars in the main stellar locus, all schemes converge very rapidly, and the simplest scheme giving consistent results consists of doing a single step 2-sigma clipping before deriving the final position and width of the locus in each bin. Varying the bin size does not have any significant effect on the measured averages and widths (σ) along the main stellar locus. In the transition region between the white dwarfs and main-sequence stars in the $(g - r)$ vs $(r - i)$ CCD (i.e.

from $(r-i)=-0.06$ to 0.10) it is difficult to determine the average and width of the main stellar locus in a well-defined way. One might construct more sophisticated ways to calculate the averages and widths in this region, but we decided to just simply interpolate over it. We will later use the location and width of the main stellar locus of stars to select white dwarf–red dwarf binaries. The specific way we define these values in this region does not have any effect on the sample we select.

The result of these procedures is indicated in Fig. 4.1 as a set of points at the centre of each bin along the abscissa. These points show the average and sigma of the sources included in each bin, for each bin of the ordinate values.[4]

4.5 Selection criteria

A major issue in deriving the sample of white dwarf–red dwarf binaries is to define the separation between the main stellar locus of stars and the binary candidates. The basic idea is to use the position and width of the main stellar locus determined above to derive a well-defined limit. One would expect to have a wide range of colours for white dwarf–red dwarf binaries depending on the effective temperature and size of the white dwarf, and the spectral type of the secondary. As there will be cases in which either the white dwarf or the red dwarf can completely dominate the (optical) emission, the main issue is to limit the contamination by single stars and spurious sources. To explore this in detail we have used the available SDSS spectra (Adelman-McCarthy 2007, Data Release 5) for sources from the proper motion catalogue to study the effect of varying the separation between the main locus and the binary candidates.

As a first step we concentrated on the $(g-r)$ vs $(r-i)$ CCD because we expect this to best separate the white dwarf–red dwarf binaries from single stars. To limit the number of objects, we have only studied those sources that are 1-σ above the main locus in the $(g-r)$ vs $(r-i)$ CCD. The limiting value in $(g-r)$ as a function of $(r-i)$ is calculated by taking, for each bin in $(r-i)$, the average plus 1-σ in $(g-r)$ and linearly interpolating between

---

[4]The detailed results of the determination of the position of the main stellar locus of stars can be obtained from the authors in tabular form, listing the average and width for each combination of colours.
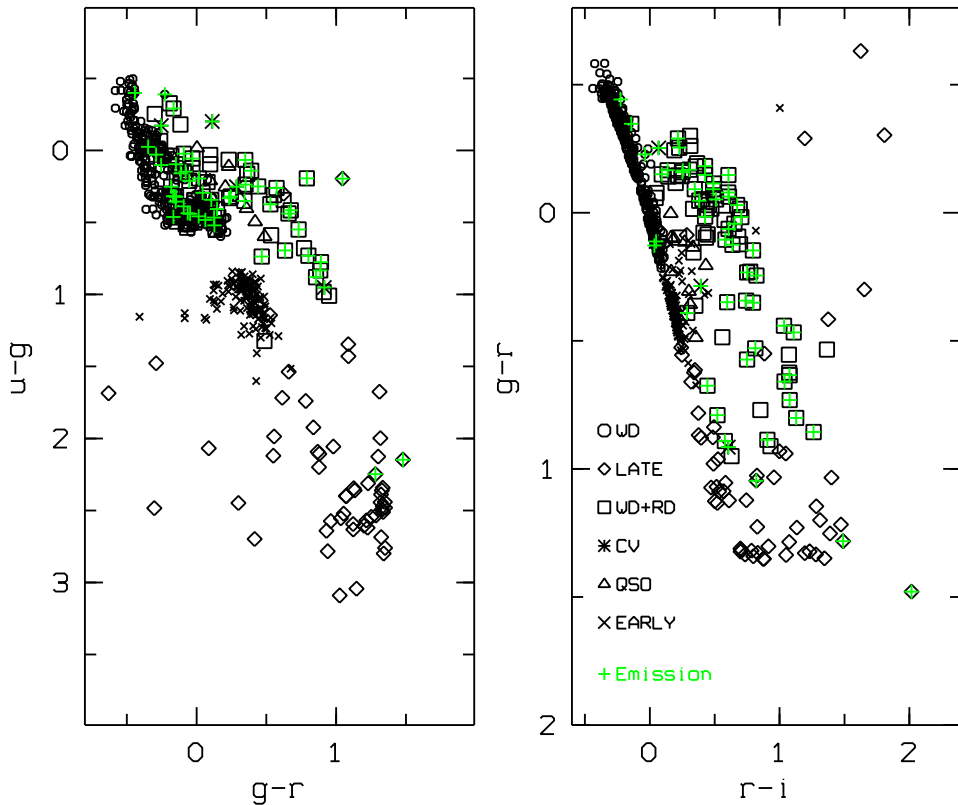
Figure 4.4: *The $(u - g)$ vs $(g - r)$ and $(g - r)$ vs $(r - i)$ CCDs of the sources that are 1-σ above the main locus in the $(g - r)$ vs $(r - i)$ CCD and have a spectrum taken as part of the SDSS. The different symbols indicate the visual classification that was made.*

these values. At the extremes, we extrapolated the limits as a function of $(r - i)$ at a constant level in $(g - r)$, corresponding to the value of the average plus 1-σ in the last bin in $(r - i)$. In this way we have selected a total of 63 602 sources from the catalogue. Out of these, a total of 554 already have a spectrum taken as part of the SDSS. Given the very conservative limits, we expect this sample to still contain a large fraction of main-sequence stars from the main stellar locus but at the same time does not exclude any likely white dwarf–red dwarf binaries.

As a next step three of the authors (TA,RG,EvdB) have independently classified the spectra visually in a number of broad groups being: white dwarfs, early-type ($\sim$A-G) dwarfs, late-type ($\sim$K-M) dwarfs, white dwarf–red dwarf binaries (WD+RD), cataclysmic variables (CVs) and quasars (QSOs). We also noted separately if a source showed Hα emission. There was a very large overlap between the classification of the sources, and a consensus was easily reached for all. The identification of Hα emission is slightly more arbitrary as it was not always straightforward to decide whether there is truly emission. This is especially the case when there might be a combination of Hα emission and (Hα or other nearby) absorption and/or when the signal-to-noise of the spectrum is relatively low. One important thing to note is that here we only look at the features in the spectrum to classify sources, and we do not specifically take their photometric colours into account.

The resulting distribution in the CCDs of the sources classified in this way is shown in Fig. 4.4 where the different symbols indicate the different classifications and a plus sign indicates the (likely) presence of emission. As expected, the plots still show the contours of the main stellar locus with the white dwarf–red dwarf binaries above it (where the relatively sharp lower-envelope in the $(g-r)$ vs $(r-i)$ CCD is the result of the 1-σ selection we have made). However, the $(g-r)$ vs $(r-i)$ CCD also shows sources in the top-right with colours well beyond what is expected for white dwarf–red dwarf binaries, while the $(u-g)$ vs $(g-r)$ CCD shows sources to the left of the main stellar locus where one does not expect sources at all. Looking at the classification of these sources and their position in the CCDs, it appears that these are likely regular main-sequence sources with an incorrect r-band magnitude.

To improve on this further we will use the information provided by the $(u-g)$ vs $(g-r)$ CCD (see Fig. 4.4). As the white dwarf, even for moderate temperatures, is in many cases expected to dominate in the blue, and there is a significant overlap between the expected position in the CCD of white dwarf–red dwarf binaries and that of single white dwarfs (see Fig. 4.2), we simply have included all sources bluer than $(u-g) = +0.85$ (the blue cut-off of the main-sequence). In the $(u-g)$ vs $(g-r)$ CCD we only take into account the separation between white dwarf–red dwarf binaries and main-sequence stars using the position and width of the main locus as defined in Sect. 4.4.
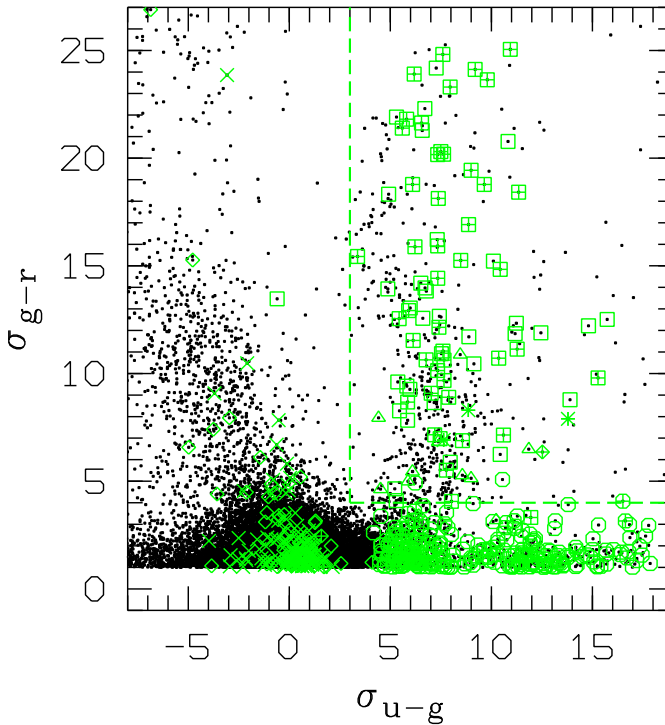
Figure 4.5: *The distance to the main stellar locus in units of σ for the sources that are more than 1-σ above the main locus in the $(g - r)$ vs $(r - i)$ CCD. The small symbols correspond to all the objects that are 1-σ above the main locus in the $(g - r)$ vs $(r - i)$ CCD. The large symbols correspond to those objects that have a spectrum taken as part of the SDSS where the different symbols indicate the classification as in Fig. 4.4.*

Given the position and width of the main stellar locus in both CCDs we can determine how distant any object is from the main locus in each case. We define these numbers in units of the width (σ) of the main locus, where we interpolate the values of the average and width in the ordinate as a function of the value of the abscissa in each case. This results in two numbers for each object, which define its locus with respect to the main stellar locus.

The results for all the sources that are more than 1-σ above the main locus in the $(g - r)$ vs $(r - i)$ CCD are shown in Fig. 4.5 as dots. The

distance of a source in $(u - g)$, as a function of $(g - r)$, is shown along the abscissa, and the distance in $(g - r)$, as a function of $(r - i)$, is shown along the ordinate. Note that the distance in $(g - r)$ is limited to values greater than 1.0 as this was imposed to limit the number of objects to investigate. Also shown in Fig. 4.5 are the sources we have classified from their existing SDSS spectra, where the different symbols indicate the classification as in Fig. 4.4. As expected, there is a strong concentration of single ('early' $\sim$A-G and 'late' $\sim$K-M) stars at low values in both colours. Single white dwarfs are concentrated at low values in σ_{g-r} and relatively high values in σ_{u-g}, while the sources classified as white dwarf–red dwarf binaries are mostly at higher, positive values. CVs and QSOs are in between the white dwarf–red dwarf binaries, though they do not reach very high distances away from the main loci.

4.5.1 Selection in the $(g - r)$ vs $(r - i)$ colour-colour diagram

The sources at high values in σ_{g-r} ($\geq$5) and negative values in σ_{u-g} are probably wrong measurements. As these are mostly classified as normal stars, it is likely that the r magnitude is incorrect (too faint) which moves them, in the $(g - r)$ vs $(r - i)$ CCD, to a position above the main locus, in the area where we also expect white dwarf–red dwarf binaries. In the $(u - g)$ vs $(g - r)$ CCD, the incorrect r magnitude moves them from the main stellar locus to the blue, and well below the location of the main locus. This clearly shows that limiting the selection to only the $(g - r)$ vs $(r - i)$ CCD would still cause a significant level of contamination in the sample (see Fig. 4.4).

Investigating Fig. 4.5 in detail one can see that to define a proper sample from the whole proper motion catalogue, a cut in σ_{g-r} is needed to separate the white dwarf–red dwarf binaries from the single stars, and a cut in σ_{u-g} is needed to remove contamination with sources that have incorrect colours. The sources we have classified as white dwarf–red dwarf binaries from their SDSS spectra do show a well defined distribution with a relatively abrupt boundary in σ_{u-g} and a more gradual variation as a function of σ_{g-r}. To explore the latter in a quantitative way we have taken all the sources with $\sigma_{u-g} > 3$ (the precise limit does not affect the following, see below) and looked at the number of sources that we have classified as white dwarf–red dwarf binaries compared to the total number of sources that were classified

Table 4.1: *The number of white dwarf–red dwarf binaries and sources with emission for* $\sigma_{u-g} > 3$. *In parenthesis the fraction (%) of the total is given.*

Type	σ_{g-r}				
	1.0	2.0	3.0	4.0	5.0
All	373	178	117	95	88
white dwarf–red dwarf	81(22)	81(46)	80(68)	79(83)	76(86)
Emission	49(13)	48(27)	48(41)	46(48)	44(50)

as a function of σ_{g-r}.

One potential problem is that any white dwarf–red dwarf binary which is dominated in brightness by one of the two components will have colours close to the main stellar locus, and might not be recognised as a binary from our visual classification. This could under-estimate the relative number of white dwarf–red dwarf binaries close to the main locus. In principle, any source classified as a single white dwarf or red dwarf might be an unrecognised white dwarf–red dwarf binary, but knowing that does not provide a way to check if we are specifically including or excluding them. For that reason we have taken all those sources that were classified as white dwarfs, red dwarfs or white dwarf–red dwarf binaries with emission. The reasoning behind this is that for any of these sources the Hα emission might indicate that the source is actually a binary, where the emission is due to heating of part of the atmosphere of a red dwarf by a relatively hot white dwarf. The relative size and temperature of the components determine if the spectrum is dominated by either component, but this sample should not be biased against white dwarf–red dwarf binaries which are dominated in brightness by one of the two components. If any white dwarf or red dwarf in this sample is just a single star with emission, you would expect them to be concentrated towards the main locus, so this would tend to over-estimate the fraction of sources at low values of σ_{g-r}.

The resulting fractions for both the sources classified as white dwarf–red dwarf binaries and the sources with Hα emission are given in Table 4.1. The changes in percentage as a function of σ_{g-r} is very similar for both groups of sources which indicates that we are unlikely to exclude any large fraction of unrecognised white dwarf–red dwarf binaries. In both cases the fraction steadily increases and then levels off. Based on these results, and as
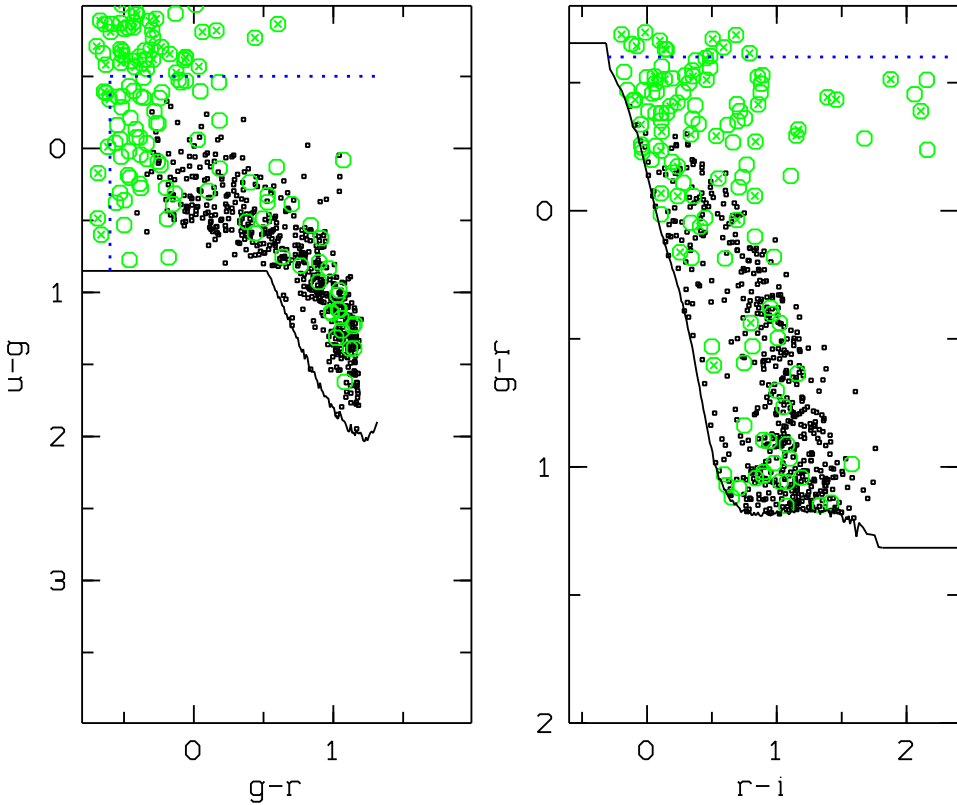
Figure 4.6: *The $(u-g)$ vs $(g-r)$ and $(g-r)$ vs $(r-i)$ CCDs of the final sample. The solid line in the CCDs shows the applied selection criteria used to define our sample. The sources brighter than $r = 16.5$ are indicated with a circle. The dashed line shows the additional colour selection (see text), where the points excluded by this selection are indicated with crosses.*

a balance between including white dwarf–red dwarf binaries and excluding any contamination, we decided to take $\sigma_{g-r} = 4$ as the limit.

4.5.2 Selection in the $(u-g)$ vs $(g-r)$ colour-colour diagram

The sources we have classified from their existing SDSS spectra do not provide a limit as well defined for σ_{u-g} as for σ_{g-r} as there is only one source in the range $\sigma_{u-g} = 0 - 4$. However, the overall distribution of all

sources presented in Fig. 4.5 follows a similar pattern to that of the sources that have been classified, with the group of sources starting off at $\sigma_{u-g} \sim 7$, $\sigma_{g-r} \sim 4$ and going up in σ_{g-r} which are all likely to be white dwarf–red dwarf binaries. The main complication when defining a limit as a function of σ_{u-g} is that this group of sources bends toward low values of σ_{u-g} for higher values of σ_{g-r}. This is due to the location of white dwarf–red dwarf binaries in the $(u - g)$ vs $(g - r)$ CCD getting closer to that of early-type main-sequence stars; see Figs. 4.1 and 4.2.

The sources at low σ_{g-r} are likely to be contaminating single early-type stars or single white dwarfs from the main stellar locus (depending on the precise choice of σ_{u-g}). Assuming that in the range of $\sigma_{u-g} \simeq 0 - 4$ the sources with $\sigma_{g-r} > 10$ are likely white dwarf–red dwarf binaries and sources with $\sigma_{g-r} < 10$ are likely contamination, we can study the fraction of white dwarf–red dwarf binary candidates to be included as a function of σ_{u-g}. For $\sigma_{g-r} > 4$ the ratio of likely white dwarf–red dwarf binaries and contaminating sources (basically those above and below $\sigma_{g-r} = 10$) is 4/33 for $1 < \sigma_{u-g} < 2$, 7/19 for $2 < \sigma_{u-g} < 3$ and 22/6 for $3 < \sigma_{u-g} < 4$. There is a marked change in the ratio going from $2 < \sigma_{u-g} < 3$, which is dominated by contaminating sources, to $3 < \sigma_{u-g} < 4$, which is dominated by likely white dwarf–red dwarf binaries, thus we selected the best limit to be $\sigma_{u-g} = 3$.

4.6 The sample

The best balance between including white dwarf–red dwarf binaries, and excluding single stars and spurious measurements, is obtained by combining the selection in both CCDs. In the $(u - g)$ vs $(g - r)$ CCD we include the sources which are more than 3-σ in $(u-g)$ above the main locus of stars, and in the $(g - r)$ vs $(r - i)$ CCD those that are more than 4-σ in $(g - r)$ above the main locus (indicated by the dashed lines in Fig. 4.5). By applying these limits we arrive to a sample of 651 sources.[5] The CCDs of the final sample are shown in Fig. 4.6. In the $(u - g)$ vs $(g - r)$ CCD, the sample is limited on the red side in $(g - r)$ as given in the $(g - r)$ vs $(r - i)$ CCD (where we have drawn the limits up to the highest value of $(g - r)$ allowed). In the $(g - r)$ vs $(r - i)$ CCD the sample is limited at $(r - i) = 2.4$ as defined at

---

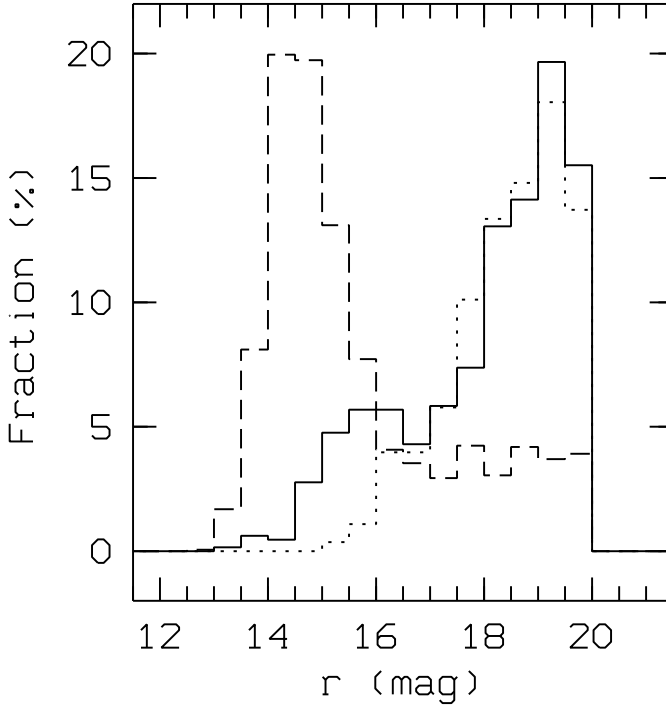[5]A list of the complete sample can be obtained from the authors upon request.

Figure 4.7: *A histogram of the r magnitudes of the sources that are included in the $(g-r)$ vs $(r-i)$ CCD but excluded in the $(u-g)$ vs $(g-r)$ CCD ($\sigma_{u-g} < 3$ and $\sigma_{g-r} > 4$; dashed line), of the sources that are included in both CCDs ($\sigma_{u-g} > 3$ and $\sigma_{g-r} > 4$; solid line), and the sources that are included in both CCDs, but have $(u-g) > 0.85$ (dotted line).*

the start of Sect. 4.4.

4.6.1 Magnitude distribution

As mentioned before, the distribution of points in Figs. 4.1, 4.4 and 4.5 seems to indicate that there are many sources that have incorrect r magnitudes. To investigate this in more detail we looked at the distribution in r magnitudes of sources in the sample. These are basically sources that are above the main locus of stars in both the $(u-g)$ vs $(g-r)$ and $(g-r)$ vs $(r-i)$ CCDs, i.e. with $\sigma_{u-g} > 3$ and $\sigma_{g-r} > 4$ (solid line in Fig. 4.7), and sources that

are above the main locus in the $(g-r)$ vs $(r-i)$ CCD but in, or below the main locus in the $(u-g)$ vs $(g-r)$ CCDs, i.e., with $\sigma_{u-g} < 3$ and $\sigma_{g-r} > 4$ (dashed line in Fig. 4.7).

The distribution of the sample itself (solid line in Fig. 4.7) shows the monotonic increase towards fainter magnitudes that one would expect, with a turnover at $r \sim 19.5$ mag indicating the completeness limit of the sample. However, there is also an unexpected increase in the distribution towards the bright end, starting at $r \sim 16.5$ mag, which indicates some contamination. The sources that were excluded from the sample (dashed line in Fig. 4.7) have a very different distribution from that of the sample, being dominated by sources with very bright ($r \sim 14 - 15$) magnitudes, and a more or less flat distribution down to the limiting magnitude of the catalogue at $r = 20$. This is not what one would expect of a magnitude limited sample, but is consistent with the idea that most of these sources have incorrect colours (r magnitudes that are relatively too faint). These incorrect r magnitudes move the sources from the main locus, up into the area covered by white dwarf–red dwarf binaries in the $(g-r)$ vs $(r-i)$ CCD, and to the left of the main locus in the $(u-g)$ vs $(g-r)$ CCD, away from the area covered by white dwarf–red dwarf binaries.

The increase in the distribution of the sample towards bright magnitudes coincides more or less with that seen in the distribution of the sources that were excluded, indicating that the sample is affected for magnitudes brighter than $r \sim 16.5$. If these sources are similar to the majority of sources that were excluded, then the main reason why these sources are not excluded by the selection procedure is likely to be because we include all sources with $(u-g) < 0.85$ in the $(u-g)$ vs $(g-r)$ CCD. While sources with redder $(u-g)$ colours and (relatively) too faint r magnitudes will be excluded as they move to the left, below the main locus of stars, this is not the case for the bluer sources. To verify this we have also looked at the magnitude distribution of only those sources in our sample which have $(u-g) > 0.85$. These are shown as the dotted line in Fig. 4.7. For comparison, this curve was scaled such that the area for $r > 16.5$ mag is the same as that for the complete sample. The resulting distribution shows, as one would expect, a monotonic rise from the bright end towards fainter magnitudes. This indicates that the peak at brighter magnitudes ($r \sim 16$) in the distribution of the whole sample is limited to sources with $(u-g) < 0.85$, which are likely contaminating sources that have an r magnitude that is (relatively)

too faint. In Fig. 4.6 the sources with magnitudes $r < 16.5$ are indicated with a circle.

One remaining question to address is the cause for the contaminating sources. One option is that these are completely spurious sources, e.g. an artifact of the data or the reduction. However, at least some of the sources with incorrect colours are real sources that are just displaced in colour (see specifically Fig. 4.4). The brightness of all the sources with $r < 16.5$ mag in the different filters turns out to be relatively bright in all bands, and it seems likely that the incorrect magnitudes are due to some saturation effect. The spread in magnitude of the sources that are affected can be understood as due to variations in sky transparency and seeing during the observations, which will cause the source magnitude at which the detector will show saturation effects to vary.

One might expect for a bright source, the magnitude in any of the passbands to (also) be affected. However, saturation of a source in the u or i band is very unlikely and if the magnitude of a source would be fainter than its true value in either of these bands it would move a source down from the main stellar locus and the source would actually be excluded. The effect of saturation in the g band resulting in a too faint magnitude is precisely opposite to that in the r band. In this case the source would move from the main locus up into the area covered by white dwarf–red dwarf binaries in the $(u-g)$ vs $(g-r)$ CCD, but it would be down below the main locus in the $(r-i)$ vs $(g-r)$ CCD, away from the area covered by white dwarf–red dwarf binaries. The main difference between sources that are too faint in the g or the r band is that, in contrast to the $(u-g)$ vs $(g-r)$ CCD, the exclusion of sources in the $(r-i)$ vs $(g-r)$ CCD also includes the area covered by white dwarfs and sources with too faint g magnitudes that belong to the main locus of stars.

As the contaminating sources with bright r magnitudes seem to be spread-out also in the $(g-r)$ colour (see Fig. 4.6) it is not possible to exclude them. However, as white dwarf–red dwarf binaries are not expected to have $(u-g)$ and $(g-r)$ colours bluer than any single white dwarf, their number can be limited by excluding sources which are bluer than $(u-g) = -0.5$ or $(g-r) = -0.6$ (which corresponds to the blue cut-off for single white dwarfs identified in the SDSS; Kleinman et al. 2004).

The distribution in r magnitudes of sources in the sample is shown in Fig. 4.8 with a solid line. Also shown, with the dotted line, is the distribution
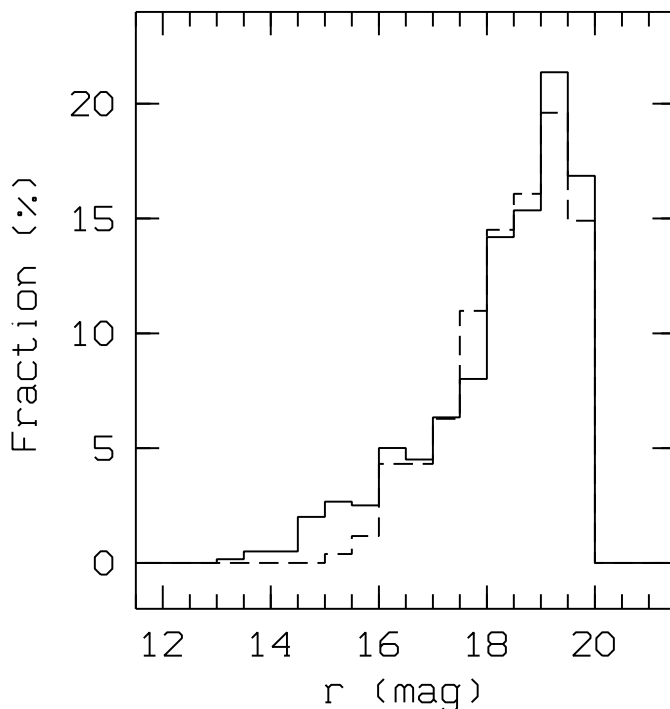
Figure 4.8: *A histogram of the r magnitudes of the sources in the final sample (solid line), and the sources in the sample that have $(u - g) > 0.85$ (dashed line).*

for sources with $(u - g) > 0.85$, where this curve was scaled such that the area for $r > 16.5$ mag is the same as that for the complete sample. The distributions are now more similar than before (see Fig. 4.7), but there still is a systematic difference starting at $r \sim 16$ mag. In Fig. 4.6 the sources with colours bluer than $(u - g) = -0.5$ or $(g - r) = -0.6$ or magnitudes $r < 16.0$ are indicated with a crosses. It can be seen that these sources largely overlap with the sources that have $r < 16.5$. On the other hand, sources that are relatively red and have colours more in line with what is expected for white dwarf–red dwarf binaries are less affected. Increasing the brightness limit to exclude contamination should also reduce the fraction of true white dwarf–red dwarf binaries that are excluded (see Sect. 4.7.3).

4.7 Discussion

4.7.1 Sample properties

From Fig. 4.6 one can see that the distribution of our sample of white dwarf–red dwarf binaries, drawn from the proper motion catalogue (Gould & Kollmeier 2004), is well defined in both CCDs. It is very different from the distribution of all the sources in the catalogue (see Fig. 4.1) which, away from the main stellar locus of stars, is dominated by contaminating sources. Also, the shape of the distribution of the sample is as expected (compare Fig. 4.6 to Fig. 4.2), and we should detect white dwarf–red dwarf binaries with a large range in white dwarf temperatures *and* secondary spectral type. In particular, our sample does not suffer from the strong bias toward high temperature young white dwarfs, nor from the strong limitations posed by 'contamination' from distant sources (QSOs, Compact Emission line Galaxies and binary giants).

The distribution of sources with existing SDSS spectra in Fig. 4.4 actually shows a strong bias towards white dwarf–red dwarf binaries with hot white dwarfs (see also the discussion below), which is not apparent in our sample (see Fig. 4.6). However, although we specifically attempt to limit any biases in our sample some selection biases will also exist. One can get some idea of these selection biases by comparing the predicted colours of white dwarf–red dwarf binaries shown in Figs. 4.2 and 4.3 with those in Fig. 4.6. E.g., we specifically select against white dwarf–red dwarf binaries with relatively early-type red dwarfs and low temperature ($T_{\text{eff}} \leq 10,000\,K$) white dwarfs because they overlap with the main stellar locus, which is excluded.

The predicted colours of white dwarf–red dwarf binaries, which at least should give a qualitative description, also provide some predictions of the general properties of the sample. E.g., the sample seems to be limited to white dwarf–red dwarf binaries with red dwarfs of spectral type no later than ∼M6, as defined by Pickles (1998). This is reasonable as it is the same as the cut-off spectral type for single red dwarfs present in the whole catalogue (see Fig. 4.1). The colour tracks do show that white dwarf–red dwarf binaries with the latest type red dwarfs should stand-out in a $(r-i)$ vs $(i-z)$ CCD. As also shown by the tracks, one would actually not find white dwarf–red dwarf binaries with very late-type red dwarfs in the bottom-right of a $(g-r)$ and $(r-i)$ CCD, but in the top-left, just to the right of the

main locus for single white dwarfs.

Fig. 4.2 indicates that for white dwarf–red dwarf binaries with a relatively hot white dwarf and late-type red dwarf, the $(u-g)$ vs $(g-r)$ CCD should provide a direct way to differentiate white dwarf–red dwarf binaries, as a function of white dwarf temperature and red dwarf spectral type. The same is true for white dwarf–red dwarf binaries with a relatively cool white dwarf and early-type red dwarf in the $(g-r)$ vs $(r-i)$ CCD. In fact, individual tracks of the predicted colours of white dwarf–red dwarf binaries with a certain spectral type red dwarf and a varying white dwarf temperature define 3-dimensional tracks in $(u-g)$, $(g-r)$ and $(r-i)$, which are used in an accompanying paper (Chapter 5) to characterise white dwarf–red dwarf binaries based on photometry. Fig. 4.3 also indicates that white dwarf–red dwarf binaries that are on the far left in the $(g-r)$ vs $(r-i)$ CCD are likely to have a white dwarf with a low surface gravity, and white dwarf–red dwarf binaries that are on the far right are likely to have a white dwarf with a high surface gravity.

A particularly interesting thing to note of the sources in our sample which already have a spectrum, is the high incidence of sources with Hα emission lines. These sources are spread-out over the CCDs (see Fig. 4.4) which indicates that they are systems with a wide range in white dwarf temperatures and red dwarf spectral types. There are two possible explanations for this emission: either it is due to heating of the red dwarf by the white dwarf; or it is due to chromospheric activity of the red dwarf. In the former case, this directly implies that the system must be a close binary. As for the latter case, chromospheric activity is correlated with fast rotation and in a close binary the red dwarf will rotate fast due to tidal interaction (Schrijver & Zwaan 2000, and references therein), i.e., also in this case the emission might point to the system being a close binary.

4.7.2 Comparison with other samples

The SDSS itself also includes a search for white dwarf–red dwarf binaries (Raymond et al. 2003; Silvestri et al. 2006). The original criteria for target selection as part of the spectroscopic follow-up within the SDSS were $(u-g) < 0.45$, $(g-r) < 0.7$, $(r-i) > 0.30$, and $(i-z) < 0.40$ (Raymond et al. 2003), which were later modified to $[(u-g) - 1.314\,(g-r)] < 0.61$, $(r-i) > 0.91$, and $(i-z) < 0.49$ (Silvestri et al. 2006), with a magnitude

cut-off of $g < 20$. The applied colour selection criteria limits the level of 'contamination', and a large fraction of the selected sources are indeed white dwarf–red dwarf binaries. On the other hand, these colour criteria cover only part of the region in colours where white dwarf–red dwarf binaries are expected. It should be noted that these limits are only used to select targets for spectroscopy, and that these targets have a low priority for spectroscopic follow-up. However, the colours of white dwarf–red dwarf binaries overlap with many other objects targeted by the SDSS. This heavily affects the final spectroscopic sample as "the majority of systems in this sample were serendipitously targeted for spectroscopy by other higher priority pipelines (e.g, quasars, white dwarfs). Therefore, our spectroscopic compilation of close binary systems is not well defined photometrically nor is it statistically complete" (Silvestri et al. 2006).

These ill defined and variable selection criteria make it hard to draw any firm conclusion from this sample. E.g., comparing the colour limits used for spectroscopic targeting of white dwarf–red dwarf binaries to the expected position of white dwarf–red dwarf binaries, as shown in Fig. 4.2, one can see that these criteria select white dwarf–red dwarf binaries with relatively late-type secondaries and relatively cool white dwarfs. This could explain the low number of binaries with early-type red dwarfs compared to single red dwarfs found by (Silvestri et al. 2006). However, these authors also noted a relatively high number of white dwarf–red dwarf binaries with hot white dwarfs in their sample, compared to single white dwarfs, which can not be explained by these selection criteria. On the other hand, targeting selection criteria for single white dwarfs and QSOs (see Fan 1999), which were the primary spectroscopic targets, include mostly only white dwarf–red dwarf binaries with relatively late-type red dwarfs and relatively hot white dwarfs. The reason for this is basically that the colours of white dwarf–red dwarf binaries with an early-type red dwarf, or with a low temperature white dwarf and a late-type red dwarf, will be too red to be included in either sample. The resulting effect of these, very different, selection biases might explain the distribution of white dwarf temperatures and red dwarf spectral types found for the white dwarf–red dwarf binaries in the SDSS sample presented by Raymond et al. (2003) and Silvestri et al. (2006). For a comparison of the properties of the sample from Silvestri et al. (2006) with our sample we refer to Chapter 5.

A separate study of white dwarf–red dwarf binaries in the SDSS was

presented by Smolčić et al. (2004). This was based on the discovery of a 'bridge', containing these binaries, connecting the white dwarfs and red dwarfs in a $(u-g)$ vs $(g-r)$ CCD of the complete SDSS Data Release 1 catalogue. This 'bridge' can also been seen in Fig. 4.1 and is directly predicted by the expected colours of white dwarf–red dwarf binaries shown in Fig. 4.2. In principle this does provide a better defined sample than that presented by Raymond et al. (2003) and Silvestri et al. (2006), as it also includes white dwarf–red dwarf binaries with relatively cool white dwarfs. However, the primary limitation remains the presence of 'contamination' from distant sources (mostly QSOs), and significant areas of the CCDs covered by white dwarf–red dwarf binaries are excluded to limit this. The specific colour criteria used in their paper also include a large part of the area covered by single M stars which increases the relative amount of contamination.

A different search for (white dwarf–red dwarf) binaries in the SDSS was made by (Pourbaix et al. 2004) using 'Colour-Induced Displacement'. This method relies on the variation in centroid position as a function of wavelength for binaries with different colour components. This method is specifically biased towards binaries with a significant separation and with components of similar brightness, which covers only a fraction of the intrinsic population of white dwarf–red dwarf binaries and as such does not provide a proper sample. However, this method can be used as a tool to separate close and wide binaries in any sample.

4.7.3   Limitations of the sample

One specific problem discussed in Sect. 4.6.1 is the contamination of bright sources with incorrect colours. A rough estimate of the degree of contamination can be made by comparing the distributions in Fig. 4.7, where we assume that the distribution for sources that have $(u-g) > 0.85$ (dotted line) is not contaminated by these bright sources (see Sect. 4.6.1). For the whole sample, 20% of the sources have magnitudes brighter than $r = 16.5$, from which we estimate that $\sim$75% (nearly 15% of the whole sample) are contaminating sources. If we exclude all sources brighter than magnitude $r = 16.5$ we estimate that we exclude $\sim$5% of the proper candidates in the sample. When we exclude the sources bluer than $(u-g) = -0.5$ or $(g-r) = -0.6$ and compare the distributions in Fig. 4.8, we find that 8% of the sources have magnitudes brighter than $r = 16.0$, of which we estimate that $\sim$80%

(nearly 7% of all the sources included) are contaminating sources. If we exclude the bluer sources and all sources brighter than magnitude $r = 16$ we estimate that we exclude less than $\sim 2\%$ of the proper candidates in the sample.

A different kind of problem is that there are still QSOs present in our sample. This is shown by the fact that we have classified 9 out of the 95 sources with an existing SDSS spectrum as QSOs. Clearly there is a problem with the determination of the proper motion for these sources. As noted in the proper motion catalogue (Gould & Kollmeier 2004), some contamination is still expected, especially towards fainter magnitudes. Indeed, 7 out of the 9 QSOs that were included have magnitudes fainter than $r = 19$, while 8 out of the 9 have a measured proper motion below 30 mas yr^{-1}, i.e., relatively close to the lower limit of 20 mas yr^{-1} of the sample. We also note that the position of the QSOs in Fig. 4.4 indicates that it might be possible to exclude a relatively large fraction of these sources applying more complicated/arbitrary colour selections in the $(g-r)$ vs $(r-i)$ CCD. It should also be noted that QSOs are targeted in particular for spectroscopic follow-up. This is likely to increase the fraction of these sources among those with an existing SDSS spectrum. We conclude that the contamination by QSOs in the whole sample is likely to be well below 10%.

If there are serious problems with the proper motion measurements, one might also expect binary giants (which are expected to have similar colours to that of white dwarf–red dwarf binaries) in the sample, and among the sources with existing spectra. However, the surface density of binary giants, down to the magnitude limit of the catalogue, compared to that of QSOs is probably low and we do not expect any significant contamination by these sources.

CVs are interacting white dwarf–red dwarf binaries and we do not specifically select against them, but they are effectively a kind of contamination. Of the 4 CVs among the sources with existing spectra, 3 are included in the final sample. This corresponds to 3% of all sources in the sample with spectra. This fraction goes down to 2% if we either only take the sources fainter than $r = 16.5$, or when we exclude the sources bluer than $(u - g) = -0.5$ or $(g - r) = -0.6$ and take the sources fainter than $r = 16.0$. In this case there is only one CV which is then excluded.

The last remaining potential sources of contamination are single white dwarfs and single red dwarfs. Among the sources with existing spectra,

there are 3 that were classified as white dwarfs, one of which shows Hα emission, and there is one red dwarf with Hα emission. These objects are only a minor source of contamination (at a level of ∼1–3%), which shows that our selection criteria are effective at separating the white dwarf–red dwarf binary candidates from single stars. This is especially true if we consider that both the sources with Hα emission are strong candidates to be true white dwarf–red dwarf binaries. However, it should be noted that none of the sources with an existing spectrum in our sample are close to the boundary with the area where single red dwarfs are located in the CCDs (see Fig. 4.6).

A separate question is what the fraction of true white dwarf–red dwarf binaries is in the sample. Taking the sources that have been classified, and given the discussion in Sect. 4.5, specifically the results presented in Table 4.1, one can estimate that at least 83% (85% if we include the source classified as a single white dwarf with Hα in emission and the one classified as a single red dwarf with Hα in emission as white dwarf–red dwarf binaries) of the final sample are genuine white dwarf–red dwarf binaries. The fraction is 85% (86%) if we only take the sources fainter than $r = 16.5$, and it is 84% (86%) if we exclude sources which are bluer than $(u - g) = -0.5$ or $(g - r) = -0.6$ and only take the sources fainter than $r = 16.0$.

One specific thing to note here is that the selection effects on the sample of sources with a spectrum is probably different from our sample, so it is not entirely clear if the above estimates can be generalised to the whole sample. However, except for the lowest magnitude bin, which has relatively few sources, the magnitude distribution of the sources with spectra is similar to the distribution for the whole sample for magnitudes fainter than $r = 16.5$, and similar to the distribution for the whole sample for magnitudes fainter than $r = 16.0$ and excluding sources which are bluer than $(u - g) = -0.5$ or $(g - r) = -0.6$ (see Sect. 4.6). From this we conclude that for the sample either excluding sources brighter than $r = 16.5$, or excluding sources brighter than $r = 16.0$ and bluer than $(u - g) = -0.5$ or $(g - r) = -0.6$, we estimate that ∼85% of the remaining sources are true white dwarf–red dwarf binaries.

We also need to know how many genuine white dwarf–red dwarf binaries are *excluded*. Of the 82 sources with an existing spectra that were classified as white dwarf–red dwarf binaries, 79 were included in the final sample. Of the sources that were excluded, 2 are in the region of single white dwarfs in the CCDs, and one is among the white dwarf–red dwarf binaries in the $(g-r)$

vs $(r - i)$ CCD, but in the region of early type single stars in the $(u - g)$ vs $(g - r)$ CCD (see Fig. 4.4 and Fig. 4.5). The latter source might have some incorrect magnitude measurement (at $r = 19.83$ and $u = 21.64$ mag it is one of the faintest in the whole sample), while the other two are probably in their proper place, but have colours that makes them impossible to separate from single white dwarfs without increasing the contamination of the sample. By simply taking the numbers of white dwarf–red dwarf binaries, we can estimate that our selection criteria exclude ∼4% of all genuine white dwarf–red dwarf binaries. If we also include single white dwarfs and red dwarfs with Hα emission, we estimate that we exclude ∼8%. Again, it should be noted that none of the sources with an existing spectrum in our sample is close to the boundary with the single red dwarfs region in the CCDs, but we do not expect that to alter our estimates very much.

If the sample is limited to sources fainter than $r = 16.5$ mag, or at sources redder than $(u - g) = -0.5$ or $(g - r) = -0.6$ and fainter than $r = 16.0$, the total number of white dwarf–red dwarf binaries that are excluded will be slightly higher (see above) and we estimate that we miss ∼10% of the white dwarf–red dwarf binaries.

As we use the proper motion catalogue of Gould & Kollmeier (2004) we have obviously a selection effect due to the proper motion limit as well. This would favor the inclusion of close, intrinsically faint binaries (late-type red dwarfs with relatively cool white dwarfs) and this would exclude binaries with a hot white dwarf and early-type red dwarf that are moving slow and are far away. In an accompanying paper Chapter 6 we will correct for this selection effect when we determine the space density for white dwarf–red dwarf binaries.

In summary, in the following papers of these series, we will use the final sample we obtain by performing the following cuts: $\sigma_{u-g} \geq 3$ and $\sigma_{g-r} \geq 4$ (Section 4.6). These selection criteria leave us with a sample of 651 white dwarf–red dwarf binary candidates that will be analysed in detail in Chapter 5 and Chapter 6.

Acknowledgements

Chapter 5

White dwarf–red dwarf binaries in the Sloan Digital Sky Survey II: Characterization[1]

E.J.M. van den Besselaar, T. Augusteijn, R. Greimel,
P.J. Groot, L. Morales-Rueda, D. Koester

Abstract

In an accompanying paper we have selected a white dwarf–red dwarf binary sample on the basis of their proper motions and the Sloan Digital Sky Survey colours. Here we will look at this sample in more detail. The aim of this paper is to spectroscopically characterize the objects found in that sample and to determine if we can use the photometry alone to study the sample as a whole. We have developed a method in which we fit both the white dwarf and the red dwarf in these binaries simultaneously. The white dwarf–red dwarf binary models are composed of single white dwarf templates added to single red dwarf templates. From the goodness of the spectral fit we can determine if an object is most likely a white dwarf–red dwarf binary or not. The parameters from the spectral fit are in good agreement with the results found from the photometry alone. Our selection and fit-

---

ting procedures are good ways to characterize white dwarf–red dwarf binaries. We can reliably characterize white dwarf–red dwarf binaries with our tracks from their photometry alone by using a proper motion and colour selected sample. This technique will be used in a forthcoming paper.

5.1   Introduction

Understanding the evolution and population of compact binaries is important, since they dominate the high energy Universe through phenomena as diverse as X-ray binaries, Type Ia supernovae, and strong gravitational wave emitters. At this moment the modelling of close binary evolution is uncertain on a small number of crucial points. One of these is the common-envelope evolution phase (Paczyński 1976). During the evolution in a binary system, the more massive star will evolve into a giant. When the two components are close enough (orbital period $\leq$10 years, depending on the masses of the components; Taam & Sandquist 2000), unstable mass transfer on a dynamical timescale may start. In this case the secondary star cannot accommodate all the mass transferred to it and an envelope will encompass both components. Due to friction, the secondary star and the core of the primary will spiral in towards eachother. After ejection of the envelope (the energetics of which is still relatively uncertain), a compact binary may emerge consisting of the core of the former primary star and the main-sequence secondary. The core will cool and eventually a white dwarf–main-sequence binary will form.

If the secondary is a low-mass (late-type) main-sequence star (red dwarf), these detached binaries are almost ideal probes of stellar evolution. They are easy to recognize observationally, are abundant, and relatively easy to model numerically. Large scale sky surveys, especially the Sloan Digital Sky Survey (SDSS; Raymond et al. 2003; Silvestri et al. 2006), are now producing large observational samples of these binaries. Other studies of detached white dwarf–red dwarf binaries can be found in Schreiber & Gänsicke (2003), Morales-Rueda et al. (2005), and Marsh (2000).

Starting with Augusteijn et al. (2007, hereafter Chapter 4) we have started a study of detached white dwarf–red dwarf binaries in the SDSS. The aim of this study is to come to a better determination of the space

density and spectral characterization of these binaries in a relatively unbiased sample that can be used later to study common-envelope evolution. In Chapter 4 we extracted a large (651) sample of white dwarf–red dwarf binaries on the basis of their colours in the SDSS and their proper motion, by using the catalogue of Gould & Kollmeier (2004). On the basis of spectral models we constructed photometric tracks to determine the position of these systems in colour-colour diagrams.

In this paper we continue our study of this sample. The aim will be to test whether it is possible to characterize the objects in our photometric sample in terms of temperature and mass of the white dwarf, spectral type of the secondary, and distance based on the photometry alone, and to come to a sample that is statistically correct, even though identifications for single objects may have large uncertainties. To do this we have extracted from the SDSS Data Release 5 (DR5) those objects from our sample that also have their spectra observed. Based on white dwarf atmosphere models and template red dwarf spectra we determine the characteristics for these objects (Sect. 5.4). In a next step we compare these characteristics with the literature (Sect. 5.5) and with the photometric tracks constructed in Chapter 4 (Sect. 5.6). However, before we can do this, we first investigate the ability to correctly derive the white dwarf mass and temperature with our technique on single objects (Sect. 5.3.2) and the ability to correctly deduce the red dwarf spectral type for single objects (Sect. 5.3.3). In Sect. 5.7 we give our conclusions. In an accompanying paper (van den Besselaar et al. 2007b, hereafter Chapter 6) we will discuss the astrophysical implications of the selected photometric sample of detached white dwarf–red dwarf population.

5.2   Selection

The SDSS (York et al. 2000) covers about one fifth of the whole sky in five filter bands. The full photometric database contains of the order of 200 million detections. Additionally, the SDSS provides spectra of about 1% of all the objects as well. Gould & Kollmeier (2004) combined the USNO-B catalogue and the SDSS DR1 database to obtain a catalogue of proper motion stars. In an effective area of 1474 square degrees (Gould 2007) $390\,476$ objects are found with proper motions in excess of 20 mas yr^{-1}. In Chapter 4 we used this database to find a large sample of detached white dwarf–red

dwarf binaries by determining the position and width of the main-sequence in the $(u-g)$ vs $(g-r)$ and the $(g-r)$ vs $(r-i)$ colour-colour diagrams. Objects with positions more than 3σ above the main-sequence in the $(u-g)$ vs $(g-r)$ colour-colour diagram *and* more than 4σ above the main-sequence in the $(g-r)$ vs $(r-i)$ colour-colour diagram were selected as candidate white dwarf–red dwarf binaries. From a visual inspection of those objects with available spectra (95 in total) it was concluded that indeed the majority of objects selected are white dwarf–red dwarf binaries. In the present paper we will use the 72 objects that have a definite spectral classification as a detached white dwarf–red dwarf binary. The proper motion information is crucial to discriminate against quasars that dominate the colour space also occupied by our targets. In this paper we take this spectroscopic sample and characterize these objects by fitting spectral models to them.

5.3 Spectral fitting

5.3.1 Procedure

In order to obtain confidence in our method for the combined white dwarf–red dwarf binary fitting, we first test it on spectra of single white dwarfs and single red dwarfs for which we specifically choose to use SDSS spectra as well to limit systematic effects.

To determine the white dwarf temperatures and surface gravities we have used a model grid of H-rich (DA) white dwarfs (Finley et al. 1997; Koester & Wolff 2000; Homeier et al. 1998; Friedrich et al. 2000). The model grid spans the range $6\,000$–$80\,000$ K in effective temperature (in steps of $1\,000$ K between $6\,000$–$20\,000$ K, $2\,000$ K between $20\,000$–$30\,000$ K, and $5\,000$ K above $30\,000$ K) and $7.0 \leq \log g \leq 9.0$ (in steps of 0.5) in white dwarf surface gravity.

To convert the fluxes of the models (which are four times the Eddington flux) to observed fluxes (in $\mathrm{erg\,s^{-1}\,cm^{-2}\,\mathring{A}^{-1}}$) we have used the mass-gravity relations of Napiwotzki et al. (2005). Stellar radii are calculated using the mass–radius relation of Eggleton as quoted by Verbunt & Rappaport (1988). Although this relation is for pure helium white dwarfs, comparing the masses and radii with the corresponding values of Panei et al. (2000) for white dwarfs with a different composition, result in a deviation of less than 10%. Since we will show that the mass of the white dwarf will be difficult to

determine in this study, we choose to use this simple relation. For the red dwarfs we use the template spectra and absolute magnitudes of Pickles (1998) in the range M0–M6 (integer types), in combination with the V-band zero-point as given by Bessell et al. (1998).

To be consistent in our fitting of the single white dwarfs and single red dwarfs, with the eventual fitting of the white dwarf–red dwarf binaries, we use exactly the same recipe for all three samples. In this fitting procedure the models are all scaled to a distance of 10 parsec. The white dwarf models and SDSS input spectra are rebinned on to a 5 Å bin, which is set by the lowest resolution spectra: the red dwarf template spectra of Pickles (1998).

The best model fit is determined by minimizing the following χ^2 relation:

$$\chi^2 = \sum_{\lambda=3850\ \mathring{A}}^{9150\ \mathring{A}} \left(\frac{R_\lambda - \bar{R}}{dR_\lambda}\right)^2 /(N-1) \tag{5.1}$$

where R_λ is the ratio between the model flux and the flux of the input spectrum at a certain wavelength, $\bar{R}$ is the average ratio over the whole wavelength range and N is the number of wavelength points. dR_λ is defined as:

$$\sqrt{R_\lambda^2 \left(\frac{dF_{\text{input},\lambda}}{F_{\text{input},\lambda}}\right)^2} \tag{5.2}$$

where $dF_{\text{input},\lambda}$ is the uncertainty on the flux of the input spectrum at a certain wavelength and $F_{\text{input},\lambda}$ is the flux of the input spectrum at a certain wavelength. The uncertainties on the model spectra are set to zero.

5.3.2 Single white dwarf tests

By fitting spectral models over the wavelength range 3900–6800 Å, Eisenstein et al. (2006, hereafter ELH) recently determined the effective temperatures and surface gravities for a large number of single white dwarfs from the SDSS DR4. To test our fitting procedure we have taken from the ELH's sample those objects with a DA classification and for which the effective temperatures and surface gravities lie within our grid. A sample of 2480 DA white dwarfs was thereby selected, and from this sample a comparison of the methods is made.

To investigate any systematic errors in our fitting procedure, we compare our results with those of ELH in four different ways. In the first run we let all parameters free to directly compare our best result with that of ELH, taking into account the coarser grid that we are using. The coarser grid we justify by the fact that the majority of the SDSS spectra have signal-to-noise ratios that exclude a high precision determination of the white dwarf temperature and surface gravity, as well as that in the fitting of the white dwarf–red dwarf binaries, the presence of the red dwarf adds another uncertainty. The surface gravities derived here are also made uncertain by the (largely unknown) effect of reddening and uncertain flux calibration on the spectra and colours (see Sect. 5.4.1).

In the second run we fixed the temperature to the one on our grid that was closest to the ELH determination, and let $\log g$ free. In the third run we fixed $\log g$ to our value closest to the ELH one and let the effective temperature free. In the fourth run we fixed both values to the ones that are closest to the ELH values.

The reduced χ^2 distribution of the first and the fourth run for all 2480 objects is shown in Fig. 5.1. The distributions for the second and third are very similar to those of the first run (top panel of Fig. 5.1). It can be seen from the distributions in this figure that they both show a clear peak near $\chi^2 \approx 1.5$. It is not surprising that this is not actually at 1 for a number of reasons. First, ELH not only fitted a white dwarf model, but also a polynomial function to correct for uncertain or unknown reddening. We have chosen not too include this in order not too make the combined white dwarf–red dwarf fitting more uncertain. The effect of this uncertain reddening is further discussed in Sect. 5.4.1. Second, our model grid is coarser than that of ELH. This will in general result in a slightly worse fit, i.e. a higher χ^2 value. Third, no errors were included on our model fits. Especially for the high signal-to-noise spectra this increased the χ^2 value for the best fit model substantially (see later on in this section and Sect. 5.4). In Fig. 5.2 we show an example of one of our white dwarf model fits with a χ^2 value of 1.34, together with the χ^2 landscape.

To investigate any systematic effects in more detail we compared our effective temperature and surface gravity results with those of ELH on an individual basis (Fig. 5.3) for our results of the first run (our best result with all parameters free versus that of ELH). It can be seen in Fig. 5.3 that the temperature determination shows a large scatter around the ELH
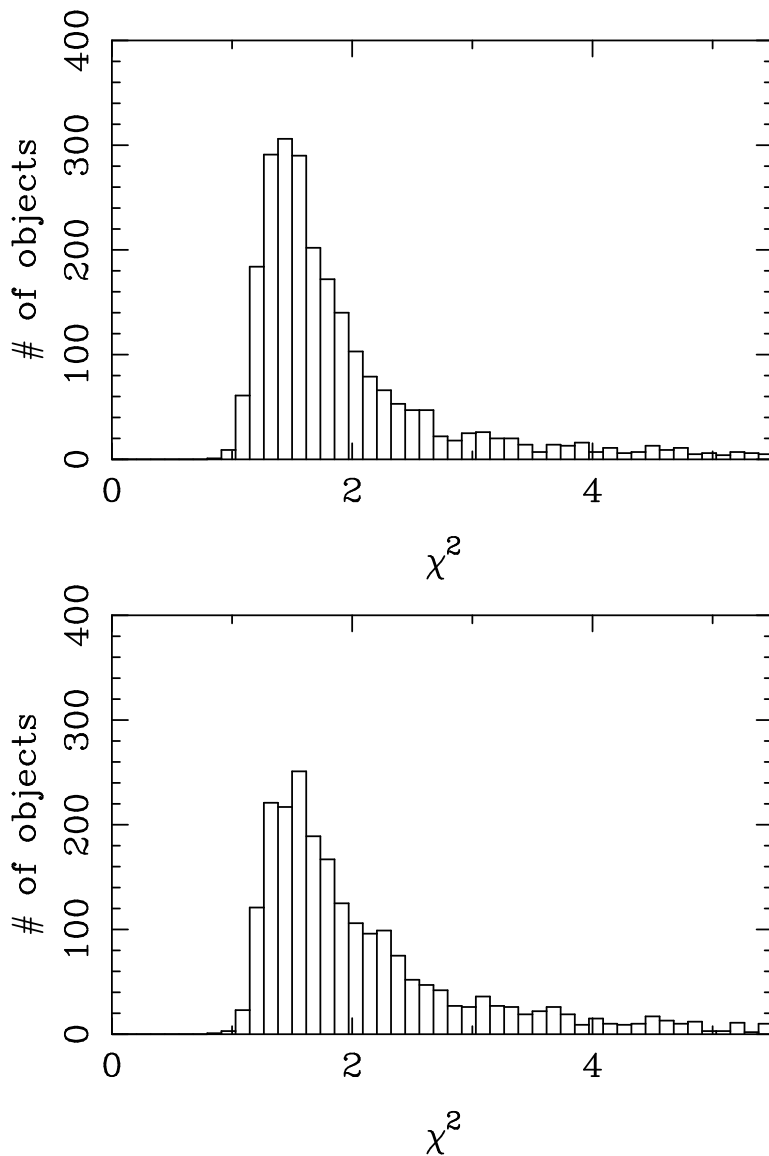
Figure 5.1: χ^2 *distributions obtained after fitting the ELH DA white dwarfs with using all our models (top) and using the models corresponding to the best results measured by Eisenstein et al. (2006) (bottom).*
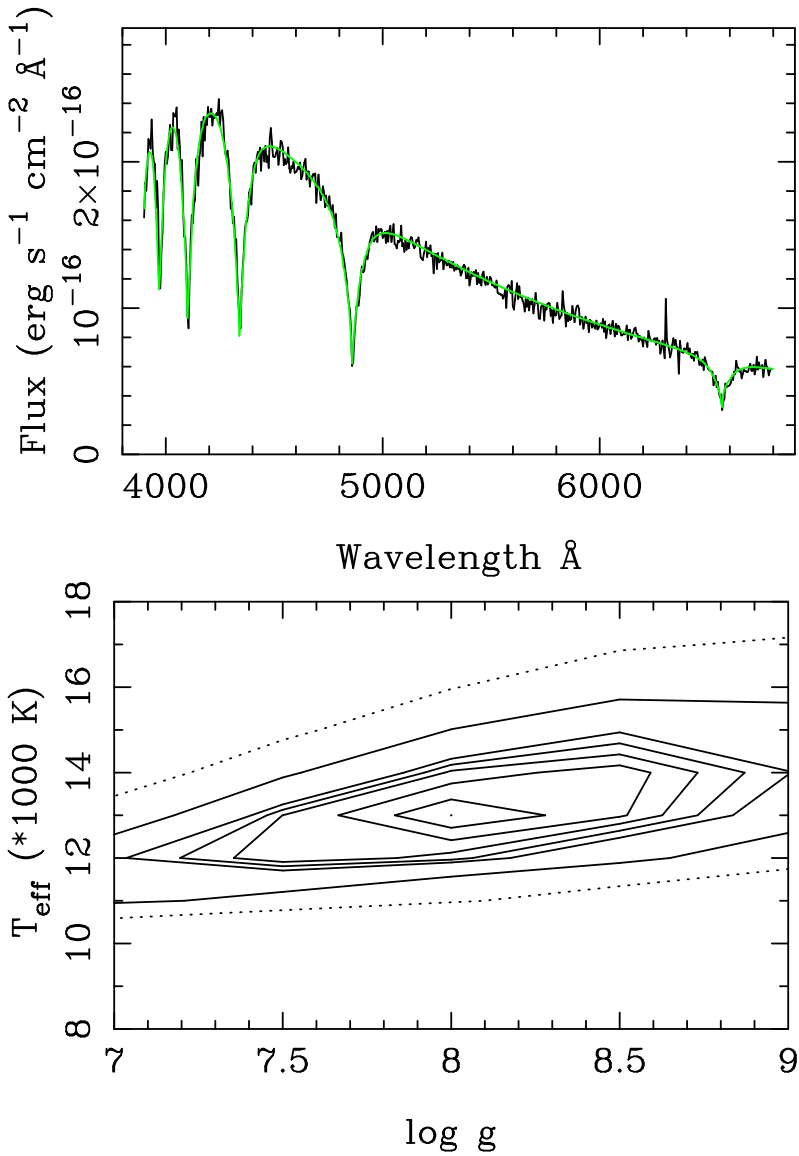
Figure 5.2: *Top: Example fit of SDSS J005620.25+140714.3 using all our models. The best fit has a temperature of 13 000 and* $\log g$ *of 8.0. The* χ^2 *of this fit is 1.34. Bottom: The corresponding* χ^2 *landscape where the* χ^2 *values are normalized. The dotted lines is normalized* $\chi^2 = 2$ *and the outer most solid line is normalized* $\chi^2 = 1.5$.

fits, as well as a small systematic offset. The scatter is mostly due to our limited temperature grid. The average of our temperature lies at a value that is ~ 0.95 times that of ELH. This effect is due to the uncertain flux calibration and uncertain and uncorrected reddening that are not taken into account. Its effect will be further discussed in Sect. 5.4.1. By comparing the surface gravities shown in Fig. 5.3, a clear systematic is seen, where at low surface gravities we underestimate the gravity and at high surface gravities we overestimate the gravity, i.e., our surface gravity distribution is wider than that of ELH. This is a direct consequence of the coarse grid in $\log g$ we have used. This effectively acts as a smearing function that will broaden the overall distribution, exactly as seen.

We notice that for spectra that have a relatively high signal-to-noise ratio ($\gtrsim 15$) our resulting χ^2 values are on average (much) higher than for objects with a lower signal-to-noise. This can be expected if the true temperature is not exactly on a grid point, combined with the fact that our models do not have uncertainties. In Fig. 5.4 we show the χ^2 vs signal-to-noise of the spectrum in the r-band wavelength range for the DA white dwarfs. We will allow objects with a high signal-to-noise to have a higher χ^2 compared to objects with low signal-to-noise, and still consider them good fits. The objects with fits below the solid line are considered good. We will discuss this in more detail in Sect. 5.4.

5.3.3 Single red dwarf tests

Recently, Bochanski et al. (2007, hereafter BWH) published red dwarf templates using multiple red dwarf spectra from the SDSS DR3. Templates were derived over the spectral range M0 to M9 (in integer types), and separated into active stars, non-active stars, and all stars combined for each spectral type. A star was considered active on the basis of the equivalent width of the Hα line.

We fitted all the BWH templates (using their full range) with the procedure described in Sect. 5.3.1. As in the binary fitting the red dwarf will not contribute much of the combined flux in the blue, we investigate whether inclusion of the bluer part of the wavelength region has an influence on the spectral type derived. To this end, we fitted the single red dwarfs over the wavelength regions of 4000–9150, 5000–9150 and 6000–9150 Å (The SDSS spectra cover $\sim$3850-9150 Å). To test the influence of possible Hα emission
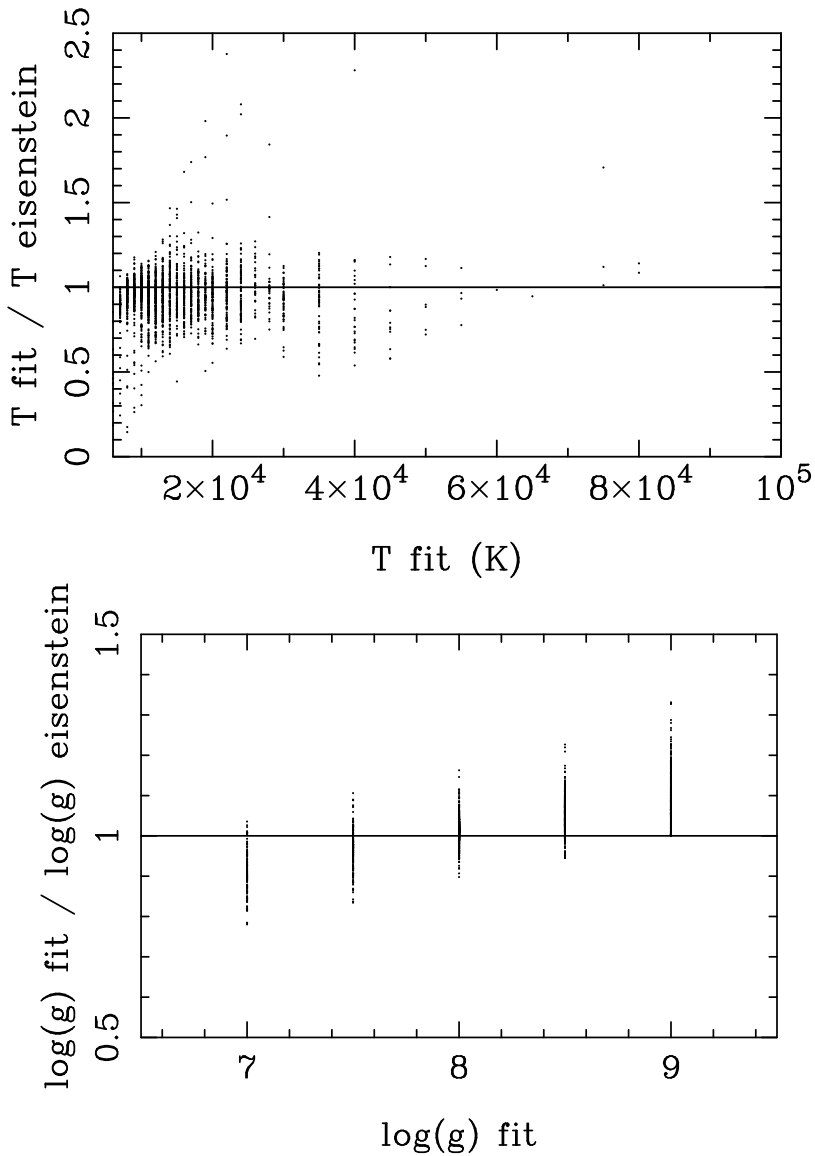
Figure 5.3: *Top: Diagram showing our white dwarf temperature divided by the temperature of ELH vs our white dwarf temperature. Bottom: Diagram showing our* $\log g$ *divided by the* $\log g$ *of ELH vs our* $\log g$.

Table 5.1: *Fit results for fitting the templates from BWH. We have used several starting wavelengths, indicated by 4000, 5000 and 6000 Å in the table. The results in the columns with Hα on top of them are the fits excluding the Hα region.*

Template	4000 Å	Hα	5000 Å	Hα	6000 Å	Hα
			Active stars			
M0	M0	M0	M0	M0	M0	M0
M1	M2	M2	M2	M2	M1	M1
M2	M2	M2	M2	M2	M3	M3
M3	M3	M3	M3	M3	M3	M3
M4	M4	M4	M4	M4	M4	M4
M5	M5	M5	M5	M5	M5	M5
M6	M5	M5	M6	M6	M6	M6
M7	M6	M6	M6	M6	M6	M6
			Non-active stars			
M0	M0	M0	M0	M0	M0	M0
M1	M2	M2	M1	M1	M1	M1
M2	M2	M2	M2	M2	M2	M2
M3	M3	M3	M3	M3	M3	M3
M4	M3	M3	M4	M4	M4	M4
M5	M5	M5	M5	M5	M5	M5
M6	M5	M5	M5	M5	M6	M6
M7	M6	M6	M6	M6	M6	M6
			All stars			
M0	M0	M0	M0	M0	M0	M0
M1	M2	M2	M1	M1	M1	M1
M2	M2	M2	M2	M2	M2	M2
M3	M3	M3	M3	M3	M3	M3
M4	M4	M4	M4	M4	M4	M4
M5	M5	M5	M5	M5	M5	M5
M6	M5	M5	M6	M6	M6	M6
M7	M6	M6	M6	M6	M6	M6
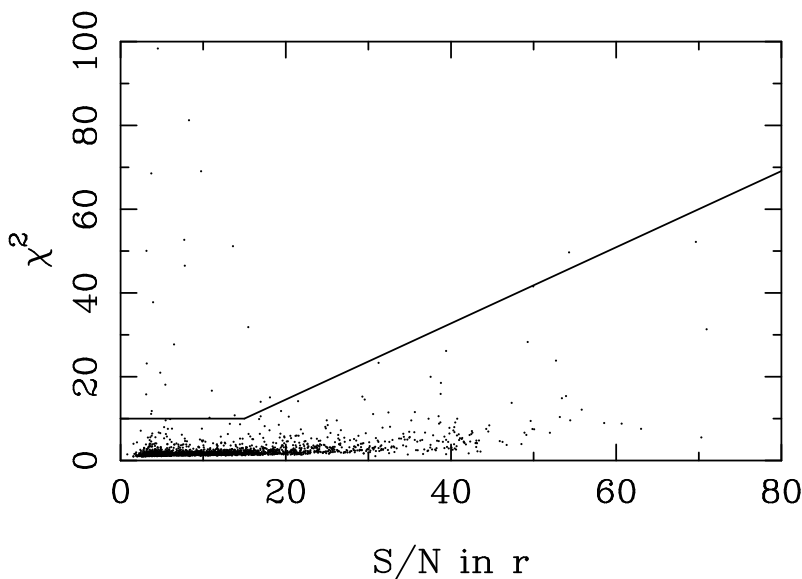
Figure 5.4: χ^2 *vs signal-to-noise in the r band. All our white dwarf fits below the solid lines are considered good fits.*

we also tested our fitting procedure both by including and excluding the Hα wavelength range.

The results of our fitting procedure are given in Table 5.1. It can be seen that our procedure returns a spectral type that is at most one subtype away from the BWH classification. Perhaps even more important than the exact correspondence between the BWH classification and our classification is the steepness of the χ^2 profile. Please note that our fitting templates only go up to spectral type M6. In Fig. 5.5 this profile is shown for a typical example. Although the minimum χ^2 value is rather high (typically $\sim$50), the rise in χ^2 between subtypes is very steep and even a classification one subtype away is almost always clearly excluded. The high minimum χ^2 is due to a number of reasons. First, there is a large intrinsic scatter in the strength of the molecular bands in red dwarfs within one subtype, due to metallicity changes and/or low-level magnetic activity (BWH, and references therein). Second, our template spectra are 'noiseless', which will add to a high χ^2 value if fitted to high signal-to-noise spectra (as also seen by the single
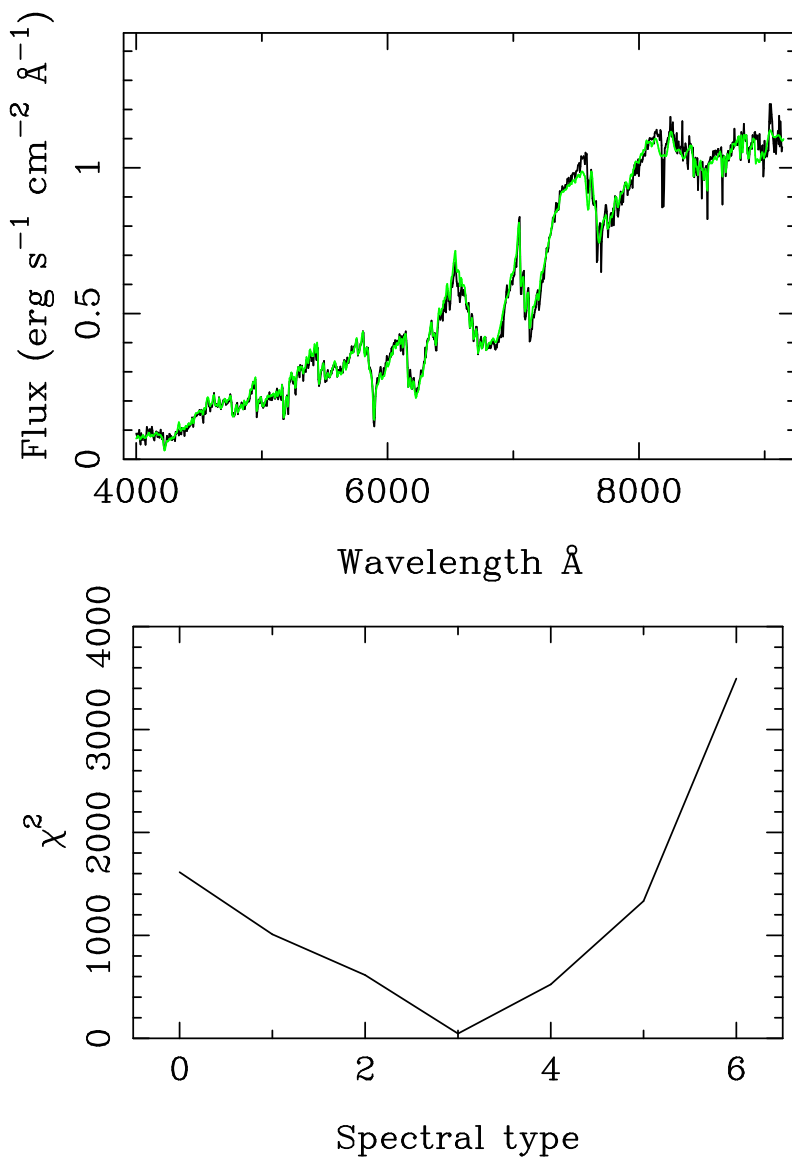
Figure 5.5: *Top: Example fit to the M3 spectrum of BWH where they used both the active and inactive stars. Our best fit is with an M3 spectral type with a χ^2 of 45.97. Bottom: χ^2 vs spectral type obtained when fitting this spectrum with our models. Note the large range on the y-axis.*

white dwarfs in Sect. 5.3.2) when combined with the first effect.

From the results in Table 5.1 we see that the inclusion of the blue part of the spectrum does not change the results very much. In the white dwarf–red dwarf binary fitting we will have a blue component from the white dwarf, so we do not expect any problems with fitting the whole wavelength range.

5.4   Application to white dwarf–red dwarf models

After having obtained confidence in the ability of our procedure to determine correct results for the single white dwarfs and single red dwarfs, we now apply the method to our white dwarf–red dwarf binary sample. To do this we have added all the possible combinations of the white dwarf models and red dwarf templates to produce the grid of white dwarf–red dwarf models that we use here. In Chapter 4 we have described our procedure to extract likely white dwarf–red dwarf candidates from the SDSS database, using additional proper motion information from Gould & Kollmeier (2004). Ninety-five of the 651 candidate systems have spectra available in the SDSS database. Of these 95 spectra, 72 were visually identified as definite white dwarf–red dwarf binaries, where four of these were classified as having a non-DA white dwarf spectrum by van den Besselaar et al. (2005, hereafter Chapter 2) and/or Silvestri et al. (2006). Since we are concerned with the population as a whole, we choose to ignore this small fraction and fitted DA models only. Our ultimate aim will be to characterize the white dwarf–red dwarf binary population only on the basis of their photometry and proper motion information. To first make a blind test of the fitting procedure, we have applied it to *all* the 95 available spectra, without making a distinction between visually identified binaries or not.

In Fig. 5.6 we show an example of our model fit, which shows an overall good agreement with the observed spectrum, and the χ^2 contours in the T_{eff}–secondary spectral type plane. Figure 5.6 shows a general behaviour of our fits with a correlation between the secondary spectral type and the white dwarf temperature. If the red dwarf spectral type is one subtype earlier or later, this raises the temperature of the white dwarf by 5 000–15 000 K (in a few exceptional cases as much as 25 000 K). For a given the spectral type, the uncertainty on the white dwarf effective temperature is a few thousand Kelvin. This effect can be easily understood by realizing
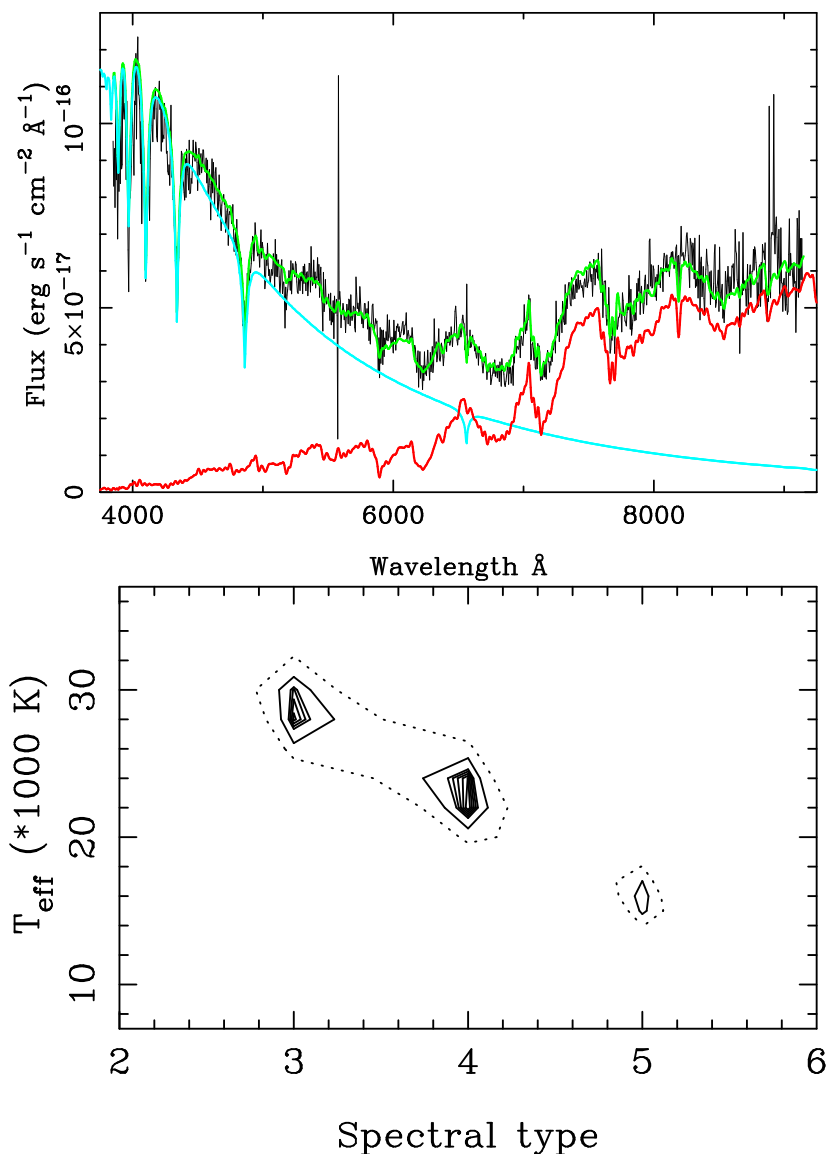
Figure 5.6: *Top: Example fit of SDSS J145527.72+611504.6. The single white dwarf has a temperature of 22 000 K and log g of 7.5 (dominating in the blue part). The single red dwarf is a main-sequence star of spectral type M4 (dominating in the red part). The grey/green line on top of the black line is the composite spectrum composed of the two single stars. Bottom: χ^2 contour plot obtained when we fix log g to 7.5. The dotted line is normalized $\chi^2 = 2$ and the outer most solid lines are normalized $\chi^2 = 1.5$.*

that we have forced both components to be at the same distance. A higher luminosity (earlier spectral type) of the secondary will therefore have to be matched by a higher luminosity (in this case a higher temperature) of the white dwarf. The fitting results for the 72 objects that were classified as binaries are given in Table 5.2 and 5.3.

Since we have fitted *all* the available spectra with white dwarf–red dwarf spectra, one would expect that those objects that are not white dwarf–red dwarf binaries (e.g. quasars or cataclysmic variables) to have large χ^2 values. Since this is also dependent on the signal-to-noise ratio in the spectra, the correlation between χ^2 value, signal-to-noise and visual classification is shown in Fig. 5.7. It is clear from this figure that indeed high χ^2 values at low signal-to-noise ratios indicate non-binaries. However, as also noted for the single white dwarfs, as the signal-to-noise ratio increases, the χ^2 value also tends to increase, even for genuine white dwarfs or binaries. This is due to the effects mentioned in Sect. 5.3; the non-inclusion of errors on the models, the effects of uncertain reddening and uncertain flux calibration, and the intrinsic spectral variety in red dwarfs. Based on Fig. 5.7, we have determined the full solid line

$$\chi^2 = \left\{ \begin{array}{ll} 0.9 \cdot \mathrm{SNR}_r - 3.6 & \text{if } \mathrm{SNR}_r \geq 15 \\ 10 & \text{if } \mathrm{SNR}_r < 15 \end{array} \right. \tag{5.3}$$

as a separation between acceptable fits and bad fits. SNR_r means the signal-to-noise in the r-band. Although this in/excludes genuine/false binaries on both sides of the line, in a statistical population study this will not change our results.

5.4.1   Systematic effect of reddening

A special mention has to be made of reddening. Already in Sect. 5.3.2, we noted that we did not include an extra polynomial order in the white dwarf fitting to account for uncertain and uncorrected reddening and uncertain flux calibration in the spectra. Fig. 5.8 shows the average of all the flux ratios between all input spectra and their corresponding best fit model. Indeed we see that the blue input flux is lower than that based on the model spectra. This effect caused the average temperature of single white dwarfs to be slightly lower than the ELH values. This can be well understood, since reddening, possibly combined with uncertain flux calibration, will preferen-
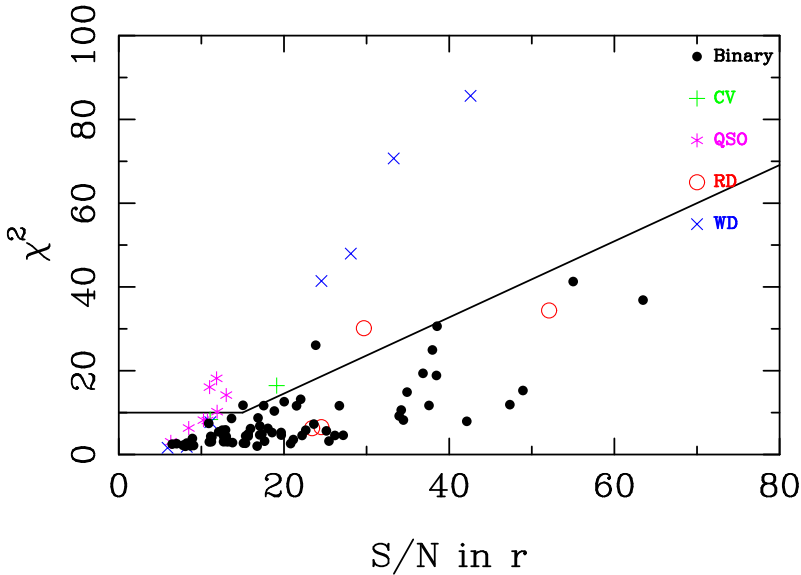
Figure 5.7: χ^2 *vs signal-to-noise in the r band for the 95 objects with spectra in our final sample. The solid line is the boundary that we have chosen to consider a fit good or bad. Objects lying below this line are included while the ones above are discarded.*

tially suppress the bluest wavelengths, making the spectrum less steep, i.e. apparently cooler. Although this lower temperature would be hard to quantify in the white dwarf–red dwarf models, it would have a noticeable effect. A lower white dwarf temperature would lower its overall luminosity. However, since we force the distance of the white dwarf and the red dwarf to be the same, and the luminosity of the red dwarf is not affected (to first order) by the reddening, the model fit will try to match the white dwarf luminosity to that needed in a physical binary. The only way that this is possible is to *lower* $\log g$, thereby making the white dwarf larger. For an underfitted temperature this would raise the luminosity to the required level. Indeed we notice that the $\log g$ values derived from our fitting are on average lower than that of the overall single white dwarf population: closer to $\log g = 7.5$ than to $\log g = 8.0$. Although this could in principle be a physical effect of binary evolution, we believe that this is due to the reddening effect and uncertain flux calibration.
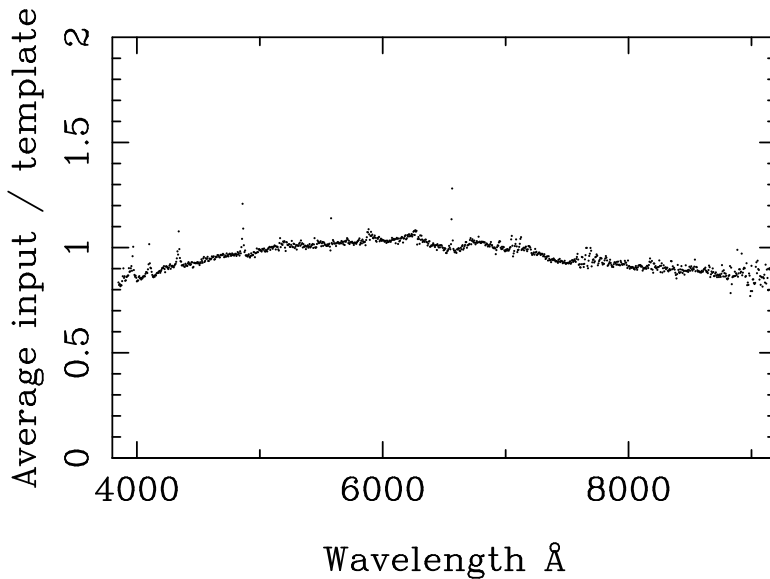
Figure 5.8: *Average flux ratios between the input spectrum and the best model.*

We have fitted the curve in Fig. 5.8 with two second order polynomials, one below 6500 Å and one above this wavelength. To test if this indeed leads to an underestimate of $\log g$ we have generated fake white dwarf–red dwarf spectra using our models, all having $\log g = 8.0$ and having various temperatures. These we have multiplied with the two second order polynomials derived from Fig. 5.8. To each wavelength, noise was added to simulate observed spectra. These fake spectra were then fitted with exactly the same procedure as our real spectra. In Fig. 5.9 we show the resulting values of the change in spectral type as a function of the difference in derived temperature, and the change in $\log g$ as a function of the difference in derived temperature. It can be clearly seen that the spectral type is mostly unaffected by this, and if it is affected, it results in an underestimate of the spectral type. However, the change in $\log g$ is much more pronounced, and indeed it is clear that even though all input spectra were produced using $\log g = 8.0$, the majority is fitted with $\log g < 8.0$. We conclude that because of this, we will systematically underestimate the surface gravity (and thereby mass) of our systems in this study. Although we cannot exclude a

real effect of binary evolution, the current dataset cannot be used to study this. We note that this reddening will also affect the photometry, which will we come back to in Sect. 5.6.

5.5   Comparison with literature

From our sample of 72 white dwarf–red dwarf binaries, 59 have a white dwarf temperature, white dwarf surface gravity, and secondary spectral type given in the tables of Silvestri et al. (2006). Silvestri et al. (2006) fit the white dwarf models and red dwarf templates separately, which does not necessarily require that the white dwarf and red dwarf are at the same distance, thus forming a physical binary. They subtract the best-fit model white dwarf from the original spectrum to reveal the secondary. A best-fit secondary template was then subtracted from the original spectrum to reveal the white dwarf which was then fitted again. This is different from our approach were we fit both components simultaneously, thereby forcing them to form a physical binary.

Figures 5.10-5.12 show our results in comparison with those of Silvestri et al. (2006) for the derived white dwarf temperature, $\log g$ and spectral type of the secondary. We note that within a few thousand degrees the majority of our white dwarf temperatures are consistent with those from Silvestri et al. (2006). In the effective gravity distribution it is clear that we underestimate $\log g$ by $\sim$0.4 on average. This is mostly due to the reddening effect described above. Silvestri et al. (2006) include a component to correct for uncertain reddening, while we do not. Our red dwarf spectral types are generally one subtype later. Silvestri et al. (2006) use the M dwarf templates from Hawley et al. (2002). When we use our fitting procedure on these M dwarf templates, we see a general shift of one subtype. This is consistent with the one subtype difference that we see by comparing our results with those from Silvestri et al. (2006). This shift in spectral type classification is probably due to a different classification scheme between Hawley et al. (2002) and Pickles (1998).
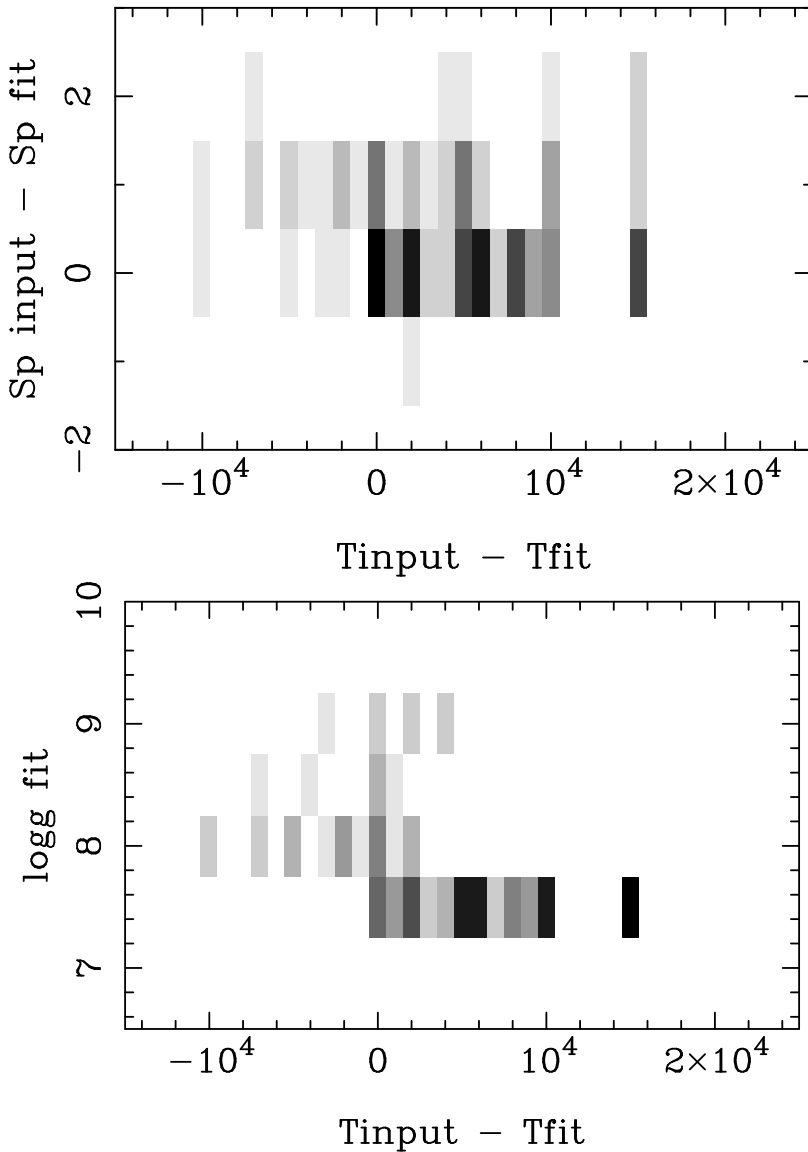
Figure 5.9: *The grey scale shows how many points are situated at each location in the plot. Top: The difference in spectral type vs the difference in temperature for the simulated white dwarf–red dwarf spectra. The grey scale runs from 0 (white) to 11 (black). Bottom: log g of the fit vs the difference in temperature for the simulated white dwarf–red dwarf spectra. The grey scale runs from 0 (white) to 10 (black).*
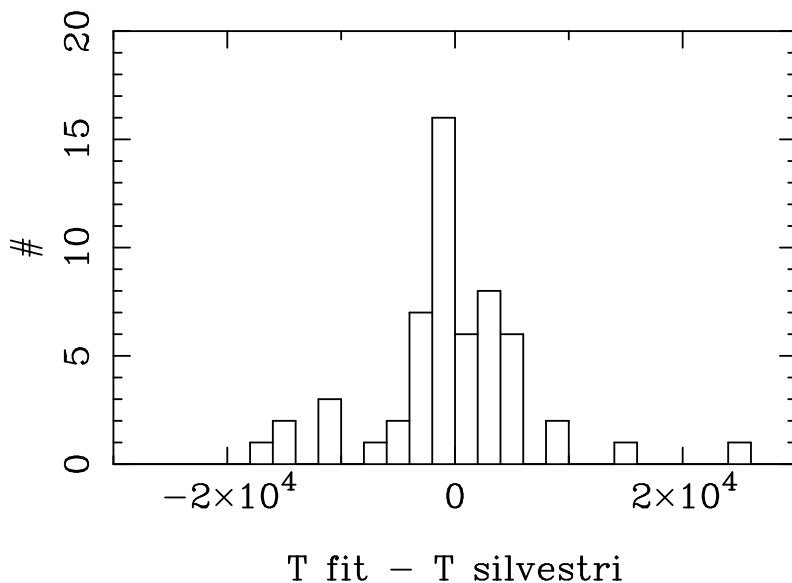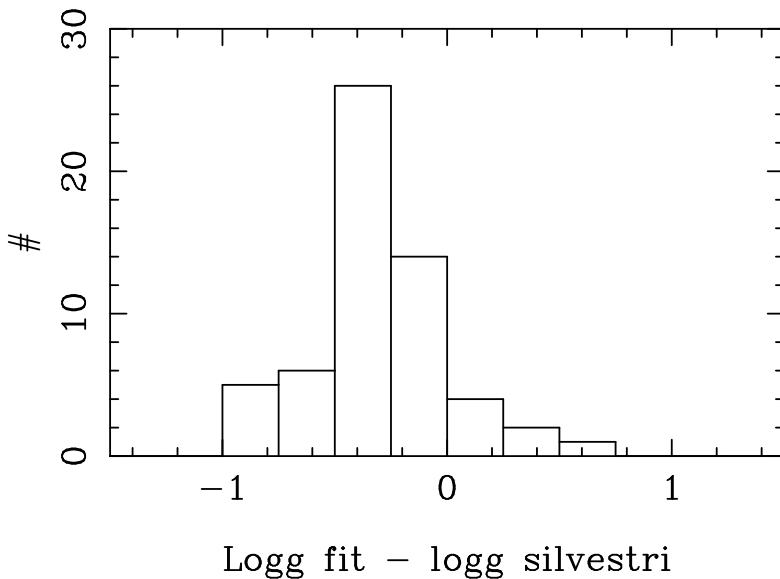
Figure 5.10: *Histogram showing the difference between our white dwarf temperature and the one from Silvestri et al. (2006).*

5.6   Binary characterization based on photometry

Only a small number of SDSS objects will ever have their spectra taken. A large jump in effectivity to study the overall population would be obtained if the white dwarf–red dwarf binaries in our photometrically determined sample could be characterized in terms of white dwarf effective temperature, spectral type of the secondary and, ideally, surface gravity, on the basis of the photometry alone.

Since we now have a photometric sample of objects, the model photometric tracks (see Chapter 4), and the spectral classification, we can actually investigate whether this is possible. To test this, we have assigned to all photometric points a characterization based on the most closely located photometric track in the $(u-g)$, $(g-r)$, $(r-i)$ data cube, where we have used the same steps in white dwarf effective temperature as in the spectral models. For those objects with spectral classifications based on the modelling described above, we have determined the difference between photometric and

Figure 5.11: *Histogram showing the difference between our white dwarf surface gravity and the one from Silvestri et al. (2006).*

spectroscopic white dwarf temperature, and the difference between photometric and spectroscopic red dwarf classification. Since the adopted white dwarf surface gravity shifts the tracks in the three-dimensional colour, we have done this separately by assigning $\log g = 7.0$, 7.5, 8.0, 8.5, and 9.0 to all objects. Note that, for single white dwarfs, observationally the $\log g$ distribution peaks rather steeply around $\log g = 8.0$. The distributions of these differences are shown in Fig. 5.13. From the statistics of the distributions the association of the photometric points with the $\log g = 7.0$ tracks gives the best correspondence between the photometry and the spectroscopy. This result is not surprising given the effect of reddening on the surface gravity as described in Sect. 5.4.1. Therefore, our association of the photometry with these tracks does not imply an, on average, lower white dwarf mass in white dwarf–red dwarf binaries than in single white dwarfs. We see that for the $\log g = 7.0$ tracks, 60% of the objects have a temperature difference of $\leq 2\,000$ K and 74% $\leq 4\,000$ K. Furthermore, 69% of the objects have the same spectral type, while 93% ≤ 1 subtype difference. This shows that we have a
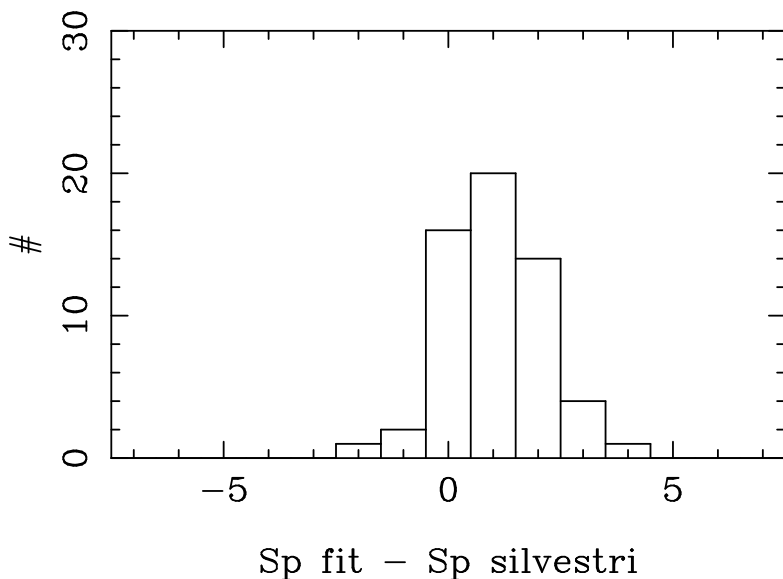
Figure 5.12: *Histogram showing the difference between our secondary spectral type and the one from Silvestri et al. (2006).*

very good agreement between the spectral and photometric classifications.

Associating all the photometric observations with the photometric $\log g = 7.0$ tracks now gives us a very strong tool to investigate the composition of the white dwarf–red dwarf binaries in the SDSS. Although the characterization of each individual object may be uncertain, the population characteristics are well determined.

5.6.1 Error determination

From Fig. 5.13 we conclude that, assuming $\log g = 7.0$, the uncertainty on the white dwarf temperature is $2\,000$ K and the uncertainty on the spectral type of the red dwarf is 0.5 subtype. For each of the possible white dwarf–red dwarf combination in our grid, we have determined the uncertainty on the r-band magnitude assuming the $2\,000$ K error on the white dwarf temperature and the 0.5 subtype error on the secondary spectral type. In cases where our grid step is $5\,000$ K we have taken an uncertainty of $5\,000$ K of the white
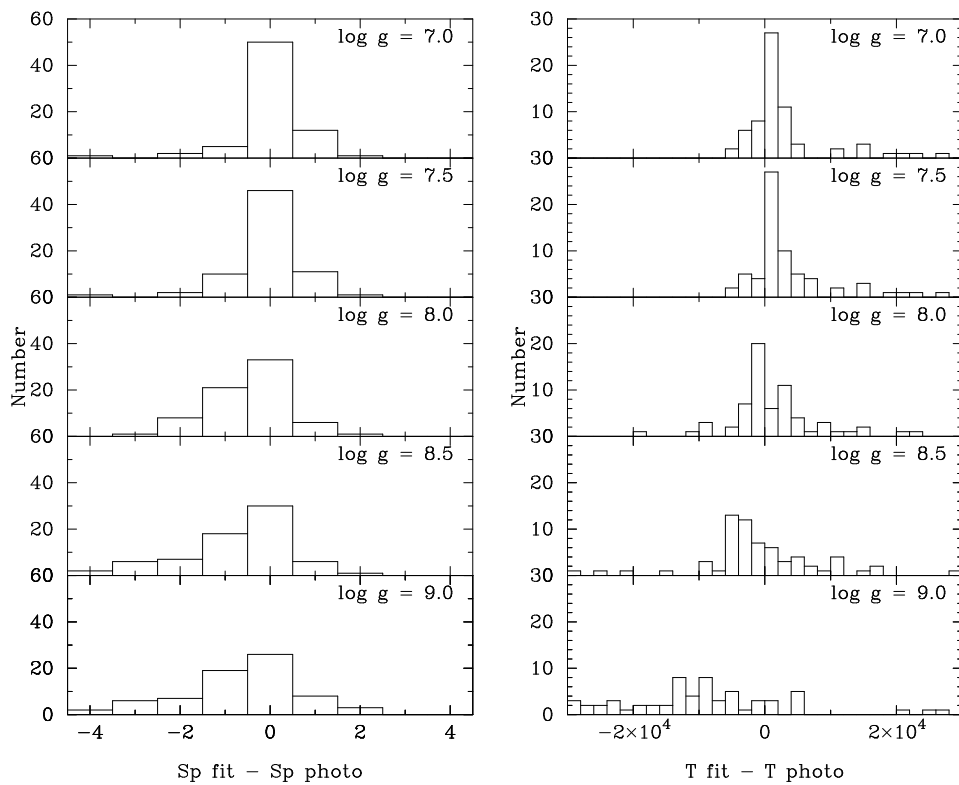
Figure 5.13: *Comparisons between the best spectral fit (*log *g free) and the best characteri-zation from the tracks by using the indicated* log *g value. Left: Histograms of the difference between the spectral type. Right: Histograms of the difference between the white dwarf temperature.*

dwarf temperature. Because our red dwarf grid consists of integer types, we have taken half the difference in absolute magnitudes between 2 subtypes as the uncertainty on having half a subtype error.

For each combination we can then derive four error determinations. First, assuming the fitted temperature is too high. Second, the spectral type of the secondary is too early. Third, the fitted temperature is too low. And fourth, the spectral type of the secondary is too late. The errors we derived are a negative error on the r-band magnitude and a positive error on the r-band magnitude, where the negative error is the highest of the first and second error determination and the positive error is the highest of the third and fourth error determination. The positive error ranges between 0.012 and 0.663, and the negative error ranges between 0.035 and 0.663 magnitudes.

5.7 Conclusion

We have shown that it is possible to characterize white dwarf–red dwarf binaries based on multicolour photometry (as provided by the SDSS), with a typical accuracy of $\sim 2\,000$-$4\,000$ K on the white dwarf temperature and a half subtype on the spectral type in the range M0-M6 compared to the spectral fitting. This classification is based on comparing spectral model fitting to photometric tracks of white dwarf–red dwarf binaries where the best photometric fit was obtained for effective white dwarf surface gravities of $\log g = 7.0$. There are however a number of limitations. The most important of these is the non-inclusion of dereddening. This causes the observed blue flux to be suppressed, leading to a white dwarf temperature that is in general $\sim 5\%$ lower than when determined from either only fitting the spectral lines, or from correcting the spectral shape by including a polynomial fit. We choose not to include such a correction, since in general the exact amount of reddening will not be known for an individual system, and also because it would add further degrees of freedom to the characterization of the white dwarf–red dwarf binaries under investigation. The consequence of this non-inclusion of extinction, is also that we are poorly constraining the surface gravity of the white dwarf in our binaries. The effect of a lower white dwarf effective temperature is compensated by also lowering the surface gravity to obtain the correct luminosity for the white dwarf to fit to the

red dwarf luminosity. This is also a consequence of the simultaneous combined fit to the white dwarf and red dwarf by requiring an equal distance to the two objects. This is justified by the fact that we assume they are in physical binaries. Associating the observed colours to photometric tracks produces a large sample (651 objects) with binary characterizations in terms of white dwarf temperatures and spectral types. Combined with the proper motions that are known for all of these, this forms the basis of Chapter 6 on the galactic population of detached white dwarf–red dwarf binaries.

Acknowledgements

Table 5.2: *Fit results for the 72 white dwarf–red dwarf binaries.*

Name (1)	MJD (2)	Pl (3)	Fib (4)	μ (5)	r (6)	$u-g$ (7)	$g-r$ (8)	$r-i$ (9)	$i-z$ (10)	S/N r (11)
SDSSJ110604.20+012010.4	52374	0509	292	32.0	18.539	0.194	0.790	0.521	0.376	13.77
SDSSJ091040.52+014548.2	51924	0471	558	29.3	16.934	1.009	0.950	0.630	0.332	42.13
SDSSJ031404.98−011136.6	52258	0412	054	22.0	19.033	0.880	0.856	1.262	0.786	13.65
SDSSJ030351.96+003548.4	51817	0411	485	29.4	18.985	0.833	0.886	0.906	0.510	13.01
SDSSJ100609.18+004417.0	51910	0269	608	51.7	17.703	0.462	0.155	0.336	0.673	23.84
SDSSJ105853.59+005608.5	51908	0277	372	44.4	18.587	0.163	0.363	0.351	0.303	15.09
SDSSJ112357.72−011027.5	51612	0280	043	20.0	18.244	0.029	−0.290	0.217	0.446	19.67
SDSSJ115156.94−000725.4	51943	0284	440	58.6	18.156	0.501	−0.015	0.333	0.510	20.03
SDSSJ122339.60−005631.2	52000	0288	015	112.8	18.056	0.494	−0.141	0.144	0.346	22.02
SDSSJ145300.98+005557.0	51994	0309	401	51.1	19.146	0.483	0.063	0.607	0.494	11.21
SDSSJ150648.12+002716.4	51665	0311	345	39.6	18.536	0.261	0.573	0.749	0.493	15.36
SDSSJ151058.76+004112.6	51665	0311	461	63.6	19.463	0.440	−0.047	0.381	0.624	8.24
SDSSJ121258.25−012310.1	52367	0332	564	27.0	16.937	0.318	−0.168	0.306	0.491	36.83
SDSSJ123139.80−031000.4	51993	0334	061	47.6	18.194	0.737	0.467	1.109	0.830	17.54
SDSSJ122752.72−015053.0	51993	0334	420	96.1	19.224	0.776	0.891	0.578	0.427	8.67
SDSSJ132312.64−025456.0[a]	51690	0341	061	42.6	17.400	0.344	0.624	1.074	0.679	33.95
SDSSJ172433.69+623410.1	51789	0352	045	82.1	17.555	−0.065	−0.261	0.313	0.373	25.45
SDSSJ171955.22+625106.7	51789	0352	171	41.6	19.413	0.349	−0.015	0.693	0.741	8.07
SDSSJ171810.15+610114.1	51792	0354	427	31.1	18.197	0.252	−0.182	0.425	0.606	17.65
SDSSJ173734.39+561224.7	51818	0358	109	148.9	18.590	0.220	0.078	0.414	0.346	15.67
SDSSJ171611.15+544346.4	51997	0367	288	20.6	18.836	0.331	0.233	0.750	0.489	22.19
SDSSJ171145.44+555444.4	51997	0367	356	28.5	18.565	−0.253	−0.300	0.310	0.490	25.13
SDSSJ172008.58+565211.7	51997	0367	525	23.7	19.274	0.438	0.659	1.038	0.660	15.04
SDSSJ172601.54+560527.0	51997	0367	548	25.0	18.880	0.351	0.343	0.742	0.494	19.66
SDSSJ234131.09+003749.2	51877	0385	500	35.4	19.196	0.679	0.770	0.852	0.536	11.28

Table 5.2: *Continued.*

Name (1)	MJD (2)	Pl (3)	Fib (4)	μ (5)	r (6)	u − g (7)	g − r (8)	r − i (9)	i − z (10)	S/N r (11)
SDSSJ001749.24−000955.5	51795	0389	112	40.5	17.034	−0.291	−0.165	0.254	0.307	47.35
SDSSJ005457.61−002517.1	51913	0394	110	36.4	18.709	0.318	−0.158	0.251	0.457	27.17
SDSSJ005208.42−005134.6	51913	0394	138	41.2	17.708	0.695	0.634	1.077	0.686	55.01
SDSSJ023515.14−000737.1	51821	0408	270	81.3	16.182	0.374	0.529	0.813	0.536	48.93
SDSSJ024642.56+004137.1	51871	0409	425	21.8	18.425	0.731	0.801	1.128	0.698	16.86
SDSSJ025753.40−003159.6	51816	0410	104	22.0	19.471	0.537	−0.068	0.497	0.630	8.61
SDSSJ030904.82−010100.9	52258	0412	215	25.1	19.512	0.549	0.731	1.078	0.665	8.91
SDSSJ032842.92+001749.6	51901	0414	531	28.1	17.133	0.983	0.911	0.930	0.623	63.47
SDSSJ010045.94+150659.1	51821	0421	463	31.8	19.005	0.465	−0.143	0.245	0.465	12.53
SDSSJ012259.53+154253.8	51893	0424	404	43.2	18.995	0.393	−0.013	0.439	0.517	11.14
SDSSJ021534.78+141846.7	51883	0428	606	53.4	19.439	0.032	0.097	0.433	0.361	7.78
SDSSJ074301.93+410655.2	51884	0432	444	33.1	17.454	0.159	−0.114	0.491	0.557	37.56
SDSSJ075009.89+381641.6	51873	0433	040	38.2	18.274	0.211	−0.052	0.510	0.597	23.61
SDSSJ093918.47+572901.2	51911	0452	067	32.2	18.207	0.394	0.093	0.681	0.611	18.05
SDSSJ025610.60−073024.5	51901	0457	509	35.7	16.863	0.436	−0.063	0.610	0.605	34.90
SDSSJ030544.41−074941.2	51929	0458	153	45.4	18.124	0.320	0.245	0.822	0.604	22.64
SDSSJ032038.72−063822.8	51924	0460	432	31.0	19.150	0.466	0.125	0.637	0.613	12.71
SDSSJ092451.63−001736.4	52000	0474	175	28.4	18.204	0.237	0.351	0.795	0.566	21.13
SDSSJ090439.84+562141.9	51924	0483	035	115.5	19.233	0.506	0.123	0.695	0.740	10.96
SDSSJ103743.60+655448.0	51930	0489	538	74.6	18.428	0.389	−0.092	0.346	0.515	15.67
SDSSJ105133.34+663401.0	51929	0490	439	20.6	17.415	0.102	−0.254	0.227	0.476	34.46
SDSSJ111530.00+664300.8	51942	0491	316	71.7	17.716	0.458	0.015	0.426	0.651	38.53
SDSSJ132040.28+661214.8	51988	0496	189	20.0	18.378	0.066	0.349	0.596	0.378	16.75
SDSSJ100905.62+024441.2	51957	0502	362	27.2	18.706	0.355	−0.150	0.092	0.480	18.83
SDSSJ111735.11+012940.0	52636	0511	284	62.2	17.645	0.452	0.085	0.446	0.687	26.70
SDSSJ120507.97+031234.4	52024	0517	332	45.1	18.524	0.345	−0.016	0.474	0.600	17.07

Table 5.2: *Continued.*

Name (1)	MJD (2)	Pl (3)	Fib (4)	μ (5)	r (6)	u − g (7)	g − r (8)	r − i (9)	i − z (10)	S/N r (11)
SDSSJ131334.74+023750.8	52295	0525	518	25.4	18.528	0.407	0.147	0.795	0.673	17.33
SDSSJ131954.22+013418.1	52312	0526	217	40.0	16.990	0.589	0.534	1.365	0.789	37.97
SDSSJ133953.88+015614.8	52022	0528	074	29.8	19.219	0.343	0.105	0.583	0.543	13.02
SDSSJ142541.31+023047.4	51999	0535	348	46.5	18.969	0.453	−0.146	0.218	0.443	10.89
SDSSJ150231.65+011045.8	52017	0539	219	209.5	18.509	0.410	−0.043	0.435	0.539	17.08
SDSSJ151046.70+022159.3	51996	0540	453	32.6	18.909	0.462	−0.166	0.137	0.282	12.10
SDSSJ074425.42+353040.8[a,b]	51993	0542	329	24.8	18.882	0.195	0.017	0.705	0.683	21.52
SDSSJ090925.42+533700.6	51999	0553	397	24.5	17.408	0.147	−0.079	0.604	0.518	34.20
SDSSJ094853.94+573957.8	52317	0558	354	26.8	18.025	−0.327	−0.193	0.364	0.298	20.81
SDSSJ094913.36+032254.5	52286	0571	251	51.6	18.950	0.294	0.043	0.652	0.659	12.69
SDSSJ101722.71+025147.9	52355	0574	044	22.0	19.653	0.065	0.230	0.774	0.503	7.01
SDSSJ123902.93+654934.5	52317	0600	620	33.7	17.118	0.096	−0.148	0.425	0.432	38.45
SDSSJ143222.06+611231.1[c,d]	52368	0607	448	20.2	18.606	0.023	−0.092	0.489	0.610	15.95
SDSSJ143633.66+615436.9	52368	0607	541	30.3	19.532	0.404	0.028	0.576	0.733	6.46
SDSSJ145527.72+611504.6	52055	0611	395	21.2	19.245	0.056	−0.030	0.673	0.571	9.05
SDSSJ152054.28+610047.1[a]	52345	0613	570	36.5	19.163	0.250	0.441	1.034	0.704	12.92
SDSSJ164615.60+422349.2	52083	0628	629	21.4	18.561	0.323	−0.147	0.606	0.744	13.26
SDSSJ170459.70+384432.9	52079	0633	065	34.1	18.369	0.123	−0.030	0.455	0.463	18.56
SDSSJ205857.09−060519.4	52176	0636	592	26.9	17.989	0.200	−0.244	0.189	0.391	26.16
SDSSJ231825.22−093539.0	52203	0645	422	20.0	18.507	0.037	−0.181	0.355	0.401	15.34
SDSSJ015132.81−080047.8	52168	0665	322	20.2	19.239	0.402	−0.053	0.405	0.540	8.08

Notes: Column (1): Name, [a] classified as DC+dM by Silvestri et al. (2006), [b] classified as DC+dM in Chapter 2, [c] classified as DB+dM in Chapter 2, [d] classified as DB+dM by Silvestri et al. (2006); Column (2): Modified Julian Date; Column (3): Plate; Column (4): Fiber; Column (5): Proper motion in mas yr^{-1}; Column (6): r magnitude in DR1; Column (7) - (10): SDSS colours; Column (11): Signal-to-noise in the r-band of the SDSS spectrum;

Table 5.3: *Fit results for the 72 white dwarf–red dwarf binaries.*

Name (1)	r (2)	T_{WD} (3)	$\log g$ (4)	Sp (5)	D (pc) (6)	χ^2 (7)	T_{ph} (8)	Sp_{ph} (9)
SDSSJ110604.20+012010.4	18.539	45000	8.0	1	1385	2.85	30000	0
SDSSJ091040.52+014548.2	16.934	20000	7.5	0	721	7.93	20000	0
SDSSJ031404.98−011136.6	19.033	8000	7.5	5	389	8.61	9000	4
SDSSJ030351.96+003548.4	18.985	13000	7.5	3	863	4.30	17000	2
SDSSJ100609.18+004417.0	17.703	50000	7.5	1	1028	26.10	13000	6
SDSSJ105853.59+005608.5	18.587	55000	7.5	0	1762	2.72	40000	0
SDSSJ112357.72−011027.5	18.244	26000	7.5	5	620	4.65	24000	5
SDSSJ115156.94−000725.4	18.156	14000	7.5	6	354	12.62	13000	6
SDSSJ122339.60−005631.2	18.056	16000	7.5	6	341	13.19	15000	6
SDSSJ145300.98+005557.0	19.146	15000	7.5	5	617	3.07	14000	5
SDSSJ150648.12+002716.4	18.536	18000	7.5	3	763	4.43	24000	2
SDSSJ151058.76+004112.6	19.463	13000	7.5	6	575	2.75	13000	6
SDSSJ121258.25−012310.1	16.937	16000	7.5	6	206	19.39	15000	6
SDSSJ123139.80−031000.4	18.194	9000	7.0	5	296	11.68	9000	5
SDSSJ122752.72−015053.0	19.224	19000	7.5	1	1730	2.08	24000	0
SDSSJ132312.64−025456.0^a	17.400	40000	9.0	3	385	9.22	17000	3
SDSSJ172433.69+623410.1	17.555	24000	7.5	5	411	3.20	24000	5
SDSSJ171955.22+625106.7	19.413	14000	7.5	5	670	1.96	15000	5
SDSSJ171810.15+610114.1	18.197	20000	7.5	5	469	3.18	18000	5
SDSSJ173734.39+561224.7	18.590	80000	7.5	1	1698	4.91	18000	5
SDSSJ171611.15+544346.4	18.836	24000	7.5	3	921	4.56	20000	3
SDSSJ171145.44+555444.4	18.565	45000	7.5	3	1086	5.65	35000	4
SDSSJ172008.58+565211.7	19.274	35000	8.5	5	525	11.76	16000	3
SDSSJ172601.54+560527.0	18.880	22000	7.5	3	913	5.26	20000	3
SDSSJ234131.09+003749.2	19.196	50000	9.0	2	1342	4.17	19000	2

Table 5.3: *Continued.*

Name (1)	r (2)	T_{WD} (3)	$\log g$ (4)	Sp (5)	D (pc) (6)	χ^2 (7)	T_{ph} (8)	Sp_{ph} (9)
SDSSJ001749.24−000955.5	17.034	80000	7.0	2	729	11.90	80000	2
SDSSJ005457.61−002517.1	18.709	17000	7.5	6	502	4.59	16000	6
SDSSJ005208.42−005134.6	17.708	11000	7.5	4	345	41.29	9000	5
SDSSJ023515.14−000737.1	16.182	17000	7.5	3	248	15.29	18000	3
SDSSJ024642.56+004137.1	18.425	13000	8.0	4	443	8.75	8000	5
SDSSJ025753.40−003159.6	19.471	13000	7.5	6	555	2.68	12000	6
SDSSJ030904.82−010100.9	19.512	16000	8.0	4	766	3.83	15000	3
SDSSJ032842.92+001749.6	17.133	11000	7.5	3	351	36.86	12000	3
SDSSJ010045.94+150659.1	19.005	15000	7.5	6	523	5.82	14000	6
SDSSJ012259.53+154253.8	18.995	13000	7.5	6	456	4.35	16000	5
SDSSJ02534.78+141846.7	19.439	55000	7.5	2	2087	2.20	35000	2
SDSSJ074301.93+410655.2	17.454	19000	7.5	5	314	11.72	19000	5
SDSSJ075009.89+381641.6	18.274	17000	7.5	5	423	7.28	18000	5
SDSSJ093918.47+572901.2	18.207	20000	7.5	4	526	6.24	18000	4
SDSSJ025610.60−073024.5	16.863	16000	7.5	5	230	14.89	15000	5
SDSSJ030544.41−074941.2	18.124	17000	7.5	4	479	5.81	20000	3
SDSSJ032038.72−063822.8	19.150	15000	7.5	5	618	4.27	14000	5
SDSSJ092451.63−001736.4	18.204	20000	7.5	3	661	3.58	20000	3
SDSSJ090439.84+562141.9	19.233	10000	7.5	6	407	3.01	14000	5
SDSSJ103743.60+655448.0	18.428	14000	7.5	6	381	4.39	14000	6
SDSSJ105133.34+663401.0	17.415	17000	7.5	6	273	8.24	18000	6
SDSSJ111530.00+664300.8	17.716	12000	7.5	6	251	30.62	13000	6
SDSSJ132040.28+661214.8	18.378	30000	7.5	2	1082	2.02	30000	2
SDSSJ100905.62+024441.2	18.706	18000	7.5	6	518	10.38	16000	6
SDSSJ111735.11+012940.0	17.645	18000	7.5	5	339	11.65	15000	5
SDSSJ120507.97+031234.4	18.524	12000	7.5	6	341	4.68	16000	5

Table 5.3: Continued.

Name (1)	r (2)	T_{WD} (3)	$\log g$ (4)	Sp (5)	D (pc) (6)	χ^2 (7)	T_{ph} (8)	Sp_{ph} (9)
SDSSJ131334.74+023750.8	18.528	17000	7.5	4	590	4.90	17000	4
SDSSJ131954.22+013418.1	16.990	22000	9.0	4	200	24.96	7000	6
SDSSJ133953.88+015614.8	19.219	26000	7.5	3	1132	3.08	15000	5
SDSSJ142541.31+023047.4	18.969	16000	7.5	6	535	7.44	15000	6
SDSSJ150231.65+011045.8	18.509	19000	7.5	5	528	6.82	16000	5
SDSSJ151046.70+022159.3	18.909	17000	7.5	6	512	5.44	15000	6
SDSSJ074425.42+353040.8^{a,b}	18.882	70000	8.5	3	958	11.64	20000	4
SDSSJ090925.42+533700.6	17.408	24000	7.5	4	410	10.63	22000	4
SDSSJ094853.94+573957.8	18.025	45000	7.5	3	876	2.62	40000	3
SDSSJ094913.36+032254.5	18.950	22000	7.5	4	811	3.05	19000	4
SDSSJ101722.71+025147.9	19.653	50000	8.5	3	1356	2.59	24000	3
SDSSJ123902.93+654934.5	17.118	20000	7.5	5	285	18.87	20000	5
SDSSJ143222.06+611231.1^{c,d}	18.606	60000	8.0	3	983	6.17	26000	4
SDSSJ143633.66+615436.9	19.532	11000	7.5	6	509	2.48	15000	5
SDSSJ145527.72+611504.6	19.245	22000	7.5	4	915	2.17	22000	4
SDSSJ152054.28+610047.1^{a}	19.163	50000	9.0	4	681	5.88	19000	3
SDSSJ164615.60+422349.2	18.561	17000	7.5	5	503	3.07	16000	5
SDSSJ170459.70+384432.9	18.369	19000	7.5	5	497	5.25	19000	5
SDSSJ205857.09−060519.4	17.989	19000	7.5	6	373	4.55	18000	6
SDSSJ231825.22−093539.0	18.507	22000	7.5	5	576	2.69	22000	5
SDSSJ015132.81−080047.8	19.239	13000	7.5	6	517	2.45	14000	6

Notes: Column (1): Name, ^{a} classified as DC+dM by Silvestri et al. (2006), ^{b} classified as DC+dM in Chapter 2, ^{c} classified as DB+dM in Chapter 2, ^{d} classified as DB+dM by Silvestri et al. (2006); Column (2): r magnitude in DR1; Column (3) - (5): White dwarf temperature and surface gravity, and secondary spectral type from the spectra; Column (6): Distance derived from our fitting; Column (7): χ^2 of our fitting; Column (8) and (9): White dwarf temperature and secondary spectral type from the tracks;

White dwarf–red dwarf binaries in the Sloan Digital Sky Survey III: Space density[1]

E.J.M. van den Besselaar, P.J. Groot, N.R. Deacon, G. Nelemans,
L. Morales-Rueda, T. Augusteijn, R. Greimel

Abstract

Here we continue the research on white dwarf–red dwarf binaries
that we started in this series of papers. A better understand-
ing of the space density and population characteristics of white
dwarf–red dwarf binaries will be needed to advance our under-
standing of binary evolution, and in particular the common-
envelope phase. The aim of this paper is to determine the
fractions of thin disc, thick disc, and halo populations of white
dwarf–red dwarf binaries and the corresponding space densities
near the Sun. We will use the proper motion and colour se-
lected photometric sample described in the previous papers in
this series. This sample will be fitted with a galactic model com-
posed of a thin disc, a thick disc, and a halo population. The
majority of the binary candidates in our sample are thin disc
objects (92%). The fractions of the thick disc and the halo are

---

[1]Submitted to A&A

5% and 3%, respectively, but we needed to fix the thick disc fraction to obtain reliable results. The local space density, by using a thick disc fraction of 5.5% of the thin disc fraction, is $5.5 \cdot 10^{-5}$ pc^{-3}. By varying the thick disc fraction between the literature values of 2 to 10% the overall space density varies between $5.1 - 5.5 \cdot 10^{-5}$ pc^{-3}. The uncertainty is estimated as $1 \cdot 10^{-5}$ pc^{-3}. This value of the space density agrees with theoretical values which vary between $3.6 \cdot 10^{-6}$ and $1.6 \cdot 10^{-4}$ pc^{-3}. With the proper motion limit of $\mu > 20$ mas yr^{-1} present in our observed sample, we conclude that we have observed about one third of the whole population of white dwarf–red dwarf binaries in the selected area by using $16.5 \leq r \leq 19.5$.

6.1   Introduction

At present, close binary evolution is uncertain on a number of crucial points. One of these is the common-envelope evolution phase (Paczyński 1976). During the evolution in a binary system, the more massive star (primary) will evolve into a giant. When the two components are close enough (orbital period ≤10 years, depending on the masses of the components; Taam & Sandquist 2000), unstable mass transfer on a dynamical timescale may start. In this case the lower mass star (secondary) cannot accommodate all the mass transferred to it and this matter will encompass both components, forming a common-envelope (CE). Due to friction, the secondary star will spiral in towards the core of the primary star. After ejection of the envelope (the energetics of which is still relatively uncertain), a compact binary consisting of the core of the former primary star and the main-sequence secondary may emerge. This core will cool into a white dwarf, and a binary, consisting of this white dwarf and the low-mass main-sequence star, will form.

Such detached low-mass binaries, consisting of a late-type secondary (red dwarf) with a white dwarf, are almost ideal probes of stellar evolution. They are easy to recognize observationally, are abundant, and are relatively easy to model numerically. Large-scale sky surveys are now producing observational samples of these binaries in large numbers, mainly from the Sloan Digital Sky Survey (SDSS; Raymond et al. 2003; Silvestri et al. 2006).

Other studies of detached white dwarf–red dwarf binaries can be found in Schreiber & Gänsicke (2003), Morales-Rueda et al. (2005), and Marsh (2000).

The general idea of our Galaxy is that it is composed of a thin disc, a thick disc, and an halo. The stars in the thin disc and thick disc follow exponential distributions in the plane of the Galaxy and perpendicular to it, while the halo stars are more spherically distributed (Binney & Merrifield 1998, chap. 10). The majority of the stars belong to the thin disc, but the relative fractions of the three components are different for different kind of stars and they are not very well known (see e.g. Binney & Merrifield 1998; Cabrera-Lavers et al. 2005; Robin et al. 1996). Each of these populations has its own kinematical properties. Knowledge of the kinematical properties (space velocity, distance) can be used to disentangle the fractions of the three populations.

With Augusteijn et al. (2007, hereafter Chapter 4) we started a study of detached white dwarf–red dwarf binaries in the SDSS. The aim of this study is to come to a better determination of the space density and spectral characterization of these binaries in a well understood sample. In Chapter 4 we extracted a large sample of 651 white dwarf–red dwarf binaries on the basis of their colours and proper motion in the SDSS, by using the catalogue of Gould & Kollmeier (2004). On the basis of spectral models we constructed photometric tracks to determine the position of these systems in colour-colour diagrams.

In van den Besselaar et al. (2007a, hereafter Chapter 5) we continued our study of this sample. In that paper we compared the classifications based on the spectral fitting with those from the photometric tracks and concluded that, for the sample as a whole, we can reliably derive the spectral type and white dwarf temperature for white dwarf–red dwarf binaries on the basis of their colours alone. In this paper we will apply this characterization to the photometric sample discussed in Chapter 4 to derive the space densities for the galactic population of white dwarf–red dwarf binaries. We present the selection in Sect. 6.2. The results for the observed sample are shown in Sect. 6.3 and the galactic model is described in Sect. 6.4. The resulting space densities are derived in Sect. 6.5 and we end with a discussion in Sect. 6.6.

6.2 Selection

To derive the space densities for the galactic population of white dwarf–red dwarf binaries, we use the full photometric sample selected and discussed in Chapter 4 and Chapter 5. This sample consists of 651 objects from the proper motion catalogue of Gould & Kollmeier (2004), which are $\geq 3\sigma$ above the main-sequence in the $(u-g)$ vs $(g-r)$ colour-colour diagram *and* $\geq 4\sigma$ above the main-sequence in the $(g-r)$ vs $(r-i)$ colour-colour diagram. Gould & Kollmeier (2004) have used the intersection between the SDSS (York et al. 2000) and the USNO-B catalogue (Monet et al. 2003) to derive the proper motions. The objects in this catalogue have $\mu \geq 20$ mas yr^{-1} with an uncertainty of 3.9 mas yr^{-1} and cover an area of 1474 deg^2 (Gould 2007). In Chapter 4 we have discussed the photometric tracks that we constructed from the absolute magnitudes of the hydrogen-rich white dwarf models and red dwarf templates. For more information on the models, we refer the reader to Chapter 5.

From the photometric tracks in 3D colour-space, we have shown in Chapter 4 that white dwarf–red dwarf binaries are not expected to have $(g-r) \leq -0.6$. Therefore we have excluded all objects below this limit from our photometric sample. Together with the magnitude cuts of $16.5 \leq r \leq 19.5$ which are needed to remove contaminant objects (see Chapter 4), this leaves 418 objects. We have seen that the majority of the objects in the full sample that have spectra are indeed detached white dwarf–red dwarf binaries ($\sim$85%). Here we will use the whole sample of 418 objects as our white dwarf–red dwarf binary candidates. In Chapter 5 we have shown that the tracks for $\log g = 7.0$ best represent the characteristics of the sample compared to the results from the spectral fitting. As discussed in Chapter 5, this low surface gravity does not immediately imply a low mass for the white dwarf, but is the result of uncertain reddening and flux calibration. For each object, the closest model grid point in 3D colour space is derived. From this point, the white dwarf effective temperature and secondary spectral type are derived.

6.2.1 Sample limitations

From the absolute magnitudes of the photometric characterization and the apparent magnitudes of the SDSS, we can derive the distance to the objects

in our sample. The distance is derived from the r-band magnitudes. In Fig. 6.1 we show the r-band magnitudes of the 418 white dwarf–red dwarf binary candidates vs the distance as derived from the photometric tracks. The solid line on the left shows where objects composed of a white dwarf with a temperature of 6 000 K, and a red dwarf of spectral type M6 should be. This combination gives us the lowest luminosity possible with our grid ($M_r = 12.7$). Therefore, this solid line gives the boundary above which we can find white dwarf–red dwarf binaries. The right solid line shows the boundary for objects with a 80 000 K white dwarf combined with an M0 red dwarf. This combination gives the highest luminosity in our grid ($M_r = 7.5$) and shows the upper boundary for objects we can find. We note there might be some clustering present in Fig. 6.1, but this is an artefact of our classification method. The uncertainties on each point (as indicated in the figure) are large enough so that this clustering is negligible in our analysis.

In Fig. 6.2 we show the distance for the white dwarf - red dwarf binary candidates vs the transverse velocity (derived from the distance and proper motion) for each object. The solid lines show the boundary for objects with a proper motion of 20 mas yr^{-1} which is the lower limit in the catalogue of Gould & Kollmeier (2004). We cannot detect objects on the left of this line. We will use a galactic model population to correct for the fraction of objects that we miss because of the proper motion limit (Sect. 6.4). The uncertainties shown in Figs 6.1 & 6.2 are determined by using the error determinations given in Chapter 5.

6.3   Results from the observed sample

6.3.1   Binary characteristics

The average white dwarf–red dwarf binary in our sample has a white dwarf effective temperature of 14 084 K and secondary spectral type of M3.7. The average effective temperature for white dwarfs in post-CE binaries, given by Schreiber & Gänsicke (2003), is 33 423 K. They do not discuss the spectral types of the secondaries in post-CE binaries. Our average effective temperature of white dwarfs in binaries is more consistent with the value for single white dwarfs (19 360 K; McCook & Sion 1999) than with the one from Schreiber & Gänsicke (2003). The difference is most likely due to the fact
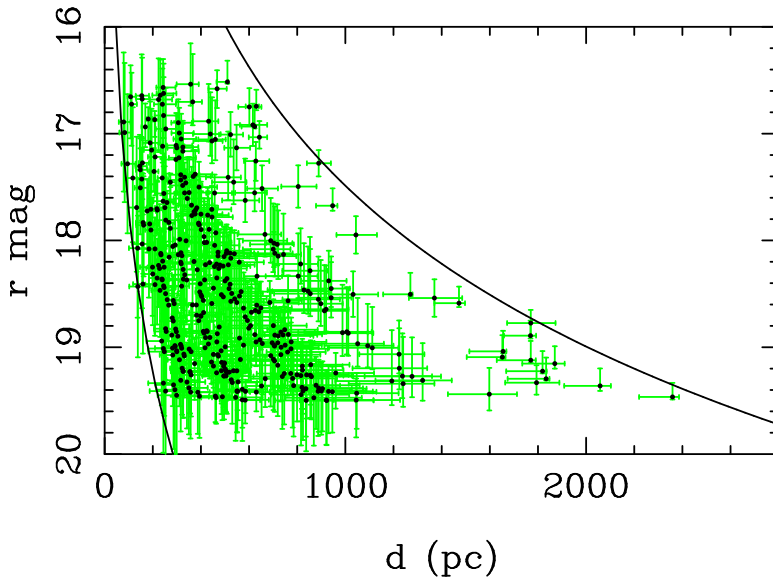
Figure 6.1: *r magnitude vs distance derived from the photometric fitting for our 418 white dwarf–red dwarf binary candidates. The left solid line corresponds to the combination of a 6 000 K white dwarf and an M6 secondary. The right solid line corresponds to the combination of a 80 000 K white dwarf and an M0 secondary.*

that most of the binaries discussed in Schreiber & Gänsicke (2003), are products of surveys not specifically searching for these binaries, mainly devised to study blue objects, thereby selecting binaries with hot white dwarfs. Our selection method in 3D colour space combined with the proper motion data, selects all possible white dwarf–red dwarf (spectral type M) combinations. Therefore, it is not really surprising that our average effective temperature of the white dwarf is closer to the one for single white dwarfs than for the one derived by Schreiber & Gänsicke (2003). The uncertainty on our white dwarf temperatures is a few thousand Kelvin at most, so the difference with the value for single white dwarfs is probably not significant.

6.3.2 Kinematics

Determining the galactic population the white dwarf–red dwarf binaries belong to, requires an understanding of the kinematic properties of the stars,
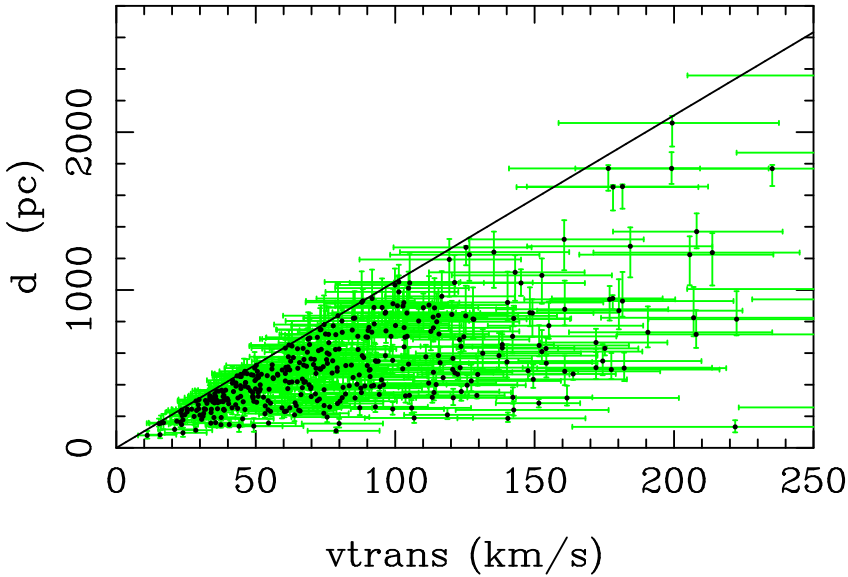
Figure 6.2: *Distance vs transverse velocity for the 418 white dwarf–red dwarf candidates. The solid line shows the boundary for objects with 20 mas yr^{-1}, which is the proper motion threshold of the catalogue.*

because each population has its own distribution of space velocities. For each object in our study, we know the proper motion in both right ascension and declination, and the distance derived from the absolute magnitude of the corresponding grid point in the 3D colour-space. Full 3D kinematics requires radial velocities as well, which are unavailable in our case. Pauli et al. (2003) have investigated the effect of setting the radial velocity to zero for a sample of white dwarfs. These results were compared with the results including the measured radial velocity for the same objects. They show in their Fig. 17 that the differences are small. A few objects might shift from thick disc to thin disc, or the other way around, but the overall results are not very different whether they set the radial velocity to zero or not. Furthermore, we discuss in Sect. 6.5 that we can not disentangle the thin disc and thick disc fractions in our sample. We study the sample of white dwarf–red dwarf binaries as a whole, and therefore our results, using zero radial velocities, are not expected to be very different from the real populations.
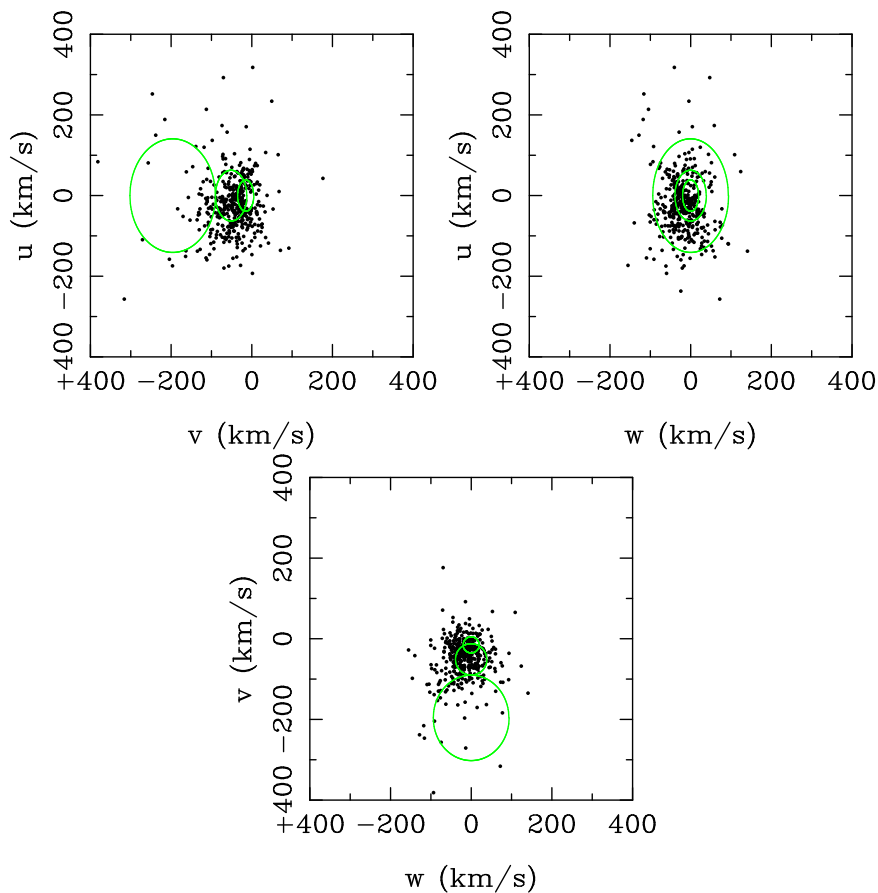
Figure 6.3: *Space velocities for the 418 objects in our sample. We have set the radial velocity to zero when calculating these diagrams. The smallest ellipses show the 1σ probabilities for the thin disc population, the middle sized ones those for the thick disc, and the largest ellipses those for the halo. These ellipses are only used for illustrative purposes.*

Table 6.1: *Velocity ellipsoids of the 3-dimensional galactic space velocities used in the galactic modelling. All velocities are in km s^{-1} (Chiba & Beers 2000; Mishenina et al. 2004).*

	thin	thick	halo
V_{lag}	-15	-51	-196
σ_U	39	63	141
σ_V	20	39	106
σ_W	20	39	94

Johnson & Soderblom (1987) give the equations to calculate the space velocities (U, V, W) and we use $(U_\odot, V_\odot, W_\odot) = (10.00 \pm 0.36, 5.25 \pm 0.62, 7.17 \pm 0.38)$ in km s^{-1} as the velocity of the Sun with respect to the local standard of rest as given by Dehnen & Binney (1998). The space velocities for each object are then defined as

$$(u, v, w) = (U, V, W) - (U_\odot, V_\odot, W_\odot). \tag{6.1}$$

U is defined as positive in the direction of the galactic center, V is positive in the direction of the galactic rotation, and W is positive in the direction of the galactic North Pole. In Fig. 6.3 we show the space velocities of the 418 objects in our sample. From these figures we can see that the majority of objects are located at low velocities, from which we expect that the majority will belong to the thin disc. We have shown the 1σ velocity ellipsoids for the three populations as well by using the values in Table 6.1 (the smallest ellipses for the thin disc, the middle sized ones for the thick disc, and largest ellipses for the halo), but these are only for illustrative purposes and are not used to determine the population where each of the observed objects belong to.

6.4   Results from the galactic modelling

By knowing the 3-dimensional galactic space velocities of white dwarf–red dwarf binaries it is possible to determine the relative fractions of the thin disc, thick disc, and halo populations. To do this we use a galactic model which will be fit to our observed sample and from which the space densities

of white dwarf–red dwarf binaries near the Sun will be derived. In Chapter 4 we have shown that we expect at least 85% of the sources in our selection to be genuine white dwarf–red dwarf binaries. Here we will first assume that all our observed objects are binaries. In Sect. 6.5 we will then correct for the fact that only 85% are probably real binaries.

6.4.1 The model

The simulated galactic models used in this analysis are calculated in the following way. For each of the thin disc and thick disc populations we have simulated $1 \cdot 10^7$ objects out to $3\,000$ pc from the Sun, which is further than the furthest observed object we have. For the halo we have simulated $2 \cdot 10^6$ objects. These initial numbers are needed to end up with a relatively large number of objects after our selection procedure, which is described later. Each object was given a random position in galactic longitude and latitude based on double exponential density distributions. For this we assumed that the thin disc has a scale height of 300 pc and a scale length of $2\,500$ pc, and the thick disc has a scale height of $1\,350$ pc and a scale length of $2\,700$ pc. These values are typical of such populations (Binney & Merrifield 1998; Robin et al. 1996). For the halo we use the density profile of a flattened sphere from Digby et al. (2003). At this point we have not assumed any relative scaling for the different populations yet, which will be determined later.

In Fig. 6.4 we show the distributions of the height above the plane (z) vs the projected distance to the galactic center within the disc (R) for $5\,000$ objects in each population. We choose a random subsample to be able to see the structure in this figure. For the simulated models we used the distance from the Sun to the galactic center as 8.0 kpc (Eisenhauer et al. 2003; Reid 1993).

After this, each of the objects is given random 3D galactic space velocities taken from the velocity ellipsoids for each of the populations. For these we have used 3D gaussians with the widths and average V velocity given in Table 6.1 (Chiba & Beers 2000; Mishenina et al. 2004). The 3D space velocities were calculated in the rest frame of the galaxy at the position of the object and then transformed to the rest frame of the Sun. From the space velocities and the distances the proper motions are derived. The galactic coordinates are converted into right ascension (RA) and declination (Dec).

Table 6.2: *Number of objects for the three populations obtained from the models after the area selection and magnitude selections where five absolute magnitude bins were used. The second line of each population includes the proper motion selection as well. The number of observed objects is also given. Furthermore, the space density for each of the models within 100 pc of the Sun (ρ_0) is given as well.*

|	Initial Number	ρ_0 (pc^{-3})	area selection	proper motion	Absolute magnitude bin 7.5–8.5	8.5–9.5	9.5–10.5	10.5–11.5	11.5–12.5
Thin	$1 \cdot 10^7$	$4.71 \cdot 10^{-4}$	33577	-	24451	17785	9648	4011	1491
	$1 \cdot 10^7$	$4.71 \cdot 10^{-4}$	33577	3547	1178	2336	2886	2229	1159
Thick	$1 \cdot 10^7$	$1.58 \cdot 10^{-4}$	188625	-	82512	28773	9048	2561	672
	$1 \cdot 10^7$	$1.58 \cdot 10^{-4}$	188625	14103	11610	10747	5932	2213	664
Halo	$2 \cdot 10^6$	$1.77 \cdot 10^{-5}$	57147	-	19046	5054	1277	331	83
	$2 \cdot 10^6$	$1.77 \cdot 10^{-5}$	57147	30014	14052	4537	1244	322	83
Obs	-	-	-	-	31	57	152	134	43
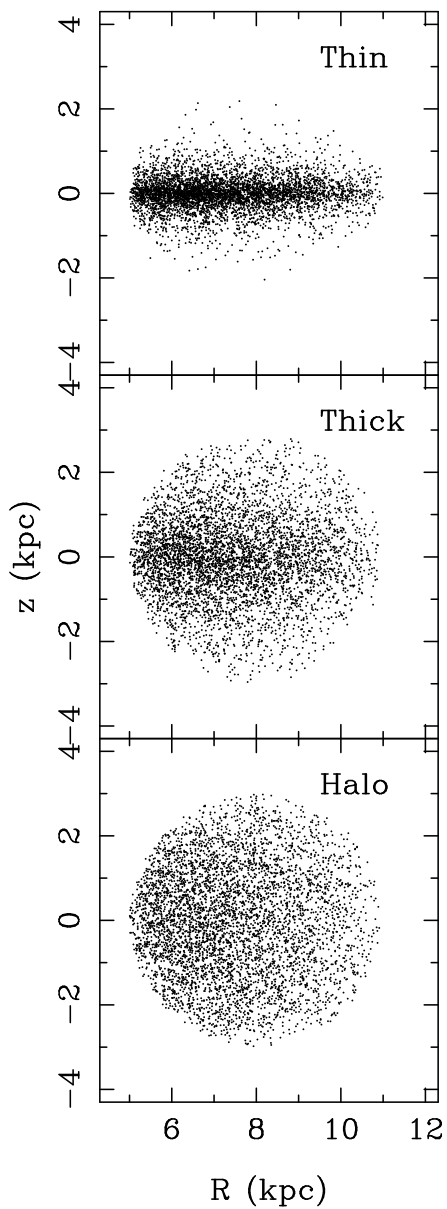
Figure 6.4: *The height above the plane vs the distance from the galactic center to the projected position of the object in the disc. To keep the distributions visible we have shown a random sample of 5 000 objects for each population.*

We do not assign magnitudes or luminosities to the objects in the models at this stage.

6.4.2 Sky area

Our observed sample covers only a certain area on the sky (see Fig. 6.5), while our models cover the whole sky. We have simulated the whole sky to be able to calculate the space densities (and thus fractions) in the vicinity of the Sun and not only in the observed area.

In order to use the galactic models to determine the missing fraction, we need to know what subset of the models cover the same area on the sky as our observed sample. To do that we have split-up the sky in galactic coordinates in sections of 0.25×0.25 degrees. The RA and Dec of the catalogue of Gould & Kollmeier (2004) were converted to galactic coordinates. For every section on the sky we checked if there was at least one object present in the catalogue of Gould & Kollmeier (2004). If that was the case, the area was included in the sky mask.

To correct for boundary effects we checked for each grid point how many of the adjacent grid points were filled. If this number was < 8 this grid point was identified as a boundary. Assuming equal probability of any filling factor, the boundary grid points are all given weight 0.5. If all 8 adjacent grid points were filled, that grid point was counted as full. This way we arrived at an area of 1478.3 deg^2. The catalogue of Gould & Kollmeier (2004) covers 1474 deg^2 (Gould 2007), so the area covered by our grid is in very good agreement with the real value.

The next step was to go through the simulated objects in each population. If an object was located in a full grid point it was included in our simulated selection. If the simulated object was located in a half grid point, only the first half of the number of objects in that grid point were included in our simulated sample. As our simulated populations are randomly ordered, we do not expect to introduce a bias by selecting objects in this way.

The simulated model catalogues used in the following sections are composed of the objects which thus cover the same area as the observed sample. The number of objects we are left with after the area selection is given in the fourth column of Table 6.2.
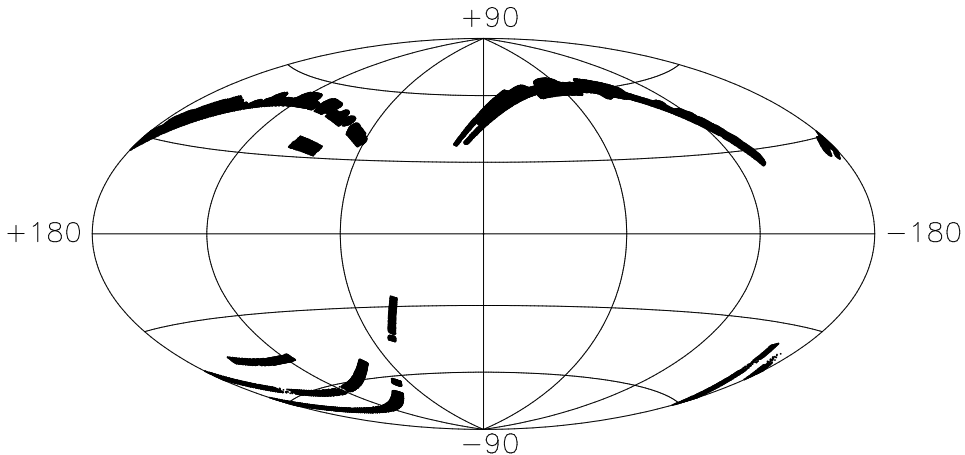
Figure 6.5: *Area covered by the Gould & Kollmeier (2004) catalogue in galactic coordinates.*

6.4.3   Selections

To simulate which objects would have been observed in a proper motion limited survey, we performed a proper motion cut of ≥ 20 mas yr^{-1} on the model catalogues, which is the same as in the catalogue of Gould & Kollmeier (2004). This we have done for the simulated thin disc, thick disc and halo population models. The number of objects in the models after the proper motion selection is given in column 5 of Table 6.2.

Furthermore, the observed sample also has a bright and faint magnitude limit. To obtain a simulated sample with the same magnitude limit as the observed sample we have performed the following procedure. This is described for one population, but we have done this for all three. As a magnitude limit is actually a distance limit (and thereby a volume limit), we need to split-up the simulated samples and observed sample in a number of bins depending on the absolute magnitude, to be able to compare them correctly. Due to the low number of observed objects for each of the white dwarf–red dwarf combinations it was decided that it was not very useful to split-up the sample in the different binary combinations. The errors on the absolute magnitudes of our classifications are relatively large and because

we want a relatively high number of observed objects per bin, we decided to split-up the sample in five absolute magnitude bins. Therefore, the model catalogue after the proper motion selection is obtained five times. For each of them we have given every object a random absolute magnitude taken from a one magnitude bin. This resulted in a catalogue for each of the bins $7.5 < M_r \leq 8.5$, $8.5 < M_r \leq 9.5$, $9.5 < M_r \leq 10.5$, $10.5 < M_r \leq 11.5$, $11.5 < M_r \leq 12.5$. This corresponds to the range in absolute magnitudes of the white dwarf–red dwarf binaries used in our analysis. The absolute magnitude together with the distance corresponds to a certain apparent magnitude where we have applied the $16.5 \leq r \leq 19.5$ magnitude cut. This resulted in 5×3 catalogues for the thin disc, thick disc and halo population models together. The resulting numbers for the different absolute magnitude bins after the magnitude selection are given in columns 6–10 of Table 6.2. The first line for each population gives the numbers without proper motion selection and the second line includes the proper motion selection.

We note that for the brightest absolute magnitude bin, only a fraction of the objects make it through the proper motion selection, while for the faintest bin, the majority is included. This is not unexpected as we have an apparent magnitude limit as well. For the brightest absolute magnitude bin, the objects are on average further away than for the faintest bin. Furthermore, larger distances imply larger space velocities to still make it into the final sample. Halo objects have on average larger space velocities and thus larger proper motions. From the values in Table 6.2 we can see that the fraction of objects that are still included with a proper motion limit is larger for the halo population than for the thin disc population. This is exactly what we expect.

6.4.4 Kinematics

For every object in the 15 models we have determined its 3D space velocities (u, v, and w) from its distance and proper motion in exactly the same way as for our observed sample. Also here, the radial velocity was set to zero. We did specifically not use the space velocities from the initial models which included a radial velocity component. We wanted to have a simulated sample with the selection effects and analysis as close as possible to the observed sample and therefore we decided to determine the space velocities from the proper motion and distance in exactly the same way as we did for

the observed sample. In this way the simulated model catalogues cover the
same area on the sky, have the same proper motion and magnitude limits,
and the same way of calculating the space velocities.

6.5   Space densities of the populations

To compare our model populations with the observed objects we need to
know the thin disc fraction, thick disc fraction, halo fraction, and the multi-
plication factor used to scale the number of objects in the simulated models
to the observed numbers. The three fractions together should add up to one,
so we have three variables to solve. The fractions and multiplication factor
are determined separately for each of the five absolute magnitude bins. The
following is a description of the method for one absolute magnitude bin.

The value for the thin disc fraction is taken between 0 and 1, and the
thick disc fraction between 0 and 0.32. Cabrera-Lavers et al. (2005, and
references therein) argue that the thick disc fraction ranges between 2% to
10% of the thin disc fraction so our upper limit of 32% is well above the
general accepted value. The halo fraction is taken as one minus the thin
disc and thick disc fractions. The simulated populations are scaled in such
a way that the initial input space densities are the same within 100 pc of
the Sun for all three populations, being 1 pc^{-3}. In this way, the scaling
factor immediately tells us the overall space density of white dwarf–red
dwarf binaries.

The scaling of the number of objects in the three populations together
with the observed sample is taken between 0 and $5 \cdot 10^{-5}$. This value is
the maximum space density in our grid for one absolute magnitude bin.
We have varied this limit and checked the χ^2 contours to be sure that all
possible values are included. For each of the three simulated models and
the observed sample we have determined the number of objects in ten bins
between -200 and $+200$ km s^{-1} for the u and w components, and ten bins
between -300 and $+100$ km s^{-1} for the v component. These limits were
chosen to minimize the number of empty bins. The total number of objects

in the model for each velocity component is determined with:

$$
\begin{aligned}
N_{\mathrm{model}} \;=\; & M(f_{\mathrm{thin}}N_{\mathrm{thin}}/\rho_{\mathrm{thin},0} + \\
& f_{\mathrm{thick}}N_{\mathrm{thick}}/\rho_{\mathrm{thick},0} + \\
& (1 - f_{\mathrm{thin}} - f_{\mathrm{thick}})N_{\mathrm{halo}}/\rho_{\mathrm{halo},0})
\end{aligned}
\tag{6.2}
$$

where N is the number of objects in a certain velocity bin for the total objects in the model and the indicated populations, f is the fraction of the indicated population, M is the multiplication factor, and ρ_0 (column 3 in Table 6.2) the space density of the whole model within 100 pc of the Sun for the indicated population. The χ^2 is then determined by:

$$
\chi^2 = \frac{\sum_{u,v,w} \sum_{\mathrm{bins}} (N_{\mathrm{obs}} - N_{\mathrm{model}})^2 / \sigma_{N\mathrm{obs}}^2}{3N_{\mathrm{bins}}}
\tag{6.3}
$$

where $\sum_{\mathrm{bins}}$ stands for the summation over the ten velocity bins and $\sum_{u,v,w}$ is the summation over the three space velocities, and N_{bins} the number of velocity bins (where we have used ten). $\sigma_{N\mathrm{obs}}$ is the uncertainty on the number of objects in the observed sample in a certain velocity bin for which we have used the estimate for small numbers of Gehrels (1986). If $N_{\mathrm{model}} \geq N_{\mathrm{obs}}$ or $N_{\mathrm{obs}} = 0$, we have used the upper limit given as $\sigma_{N\mathrm{obs}} = \sigma_+ = 1 + \sqrt{N_{\mathrm{obs}} + 0.75}$. If $N_{\mathrm{model}} < N_{\mathrm{obs}}$, the negative limit of $\sigma_{N\mathrm{obs}} = \sigma_- = \sqrt{N_{\mathrm{obs}} - 0.25}$ is used. Due to the large number of objects in our model, the uncertainty on the number of objects in the model is negligible.

The fractions and multiplication factor corresponding to the lowest χ^2 are taken as the best values. It turns out that we cannot reliably distinguish between the thin disc and thick disc fractions. We have tried a variable velocity binsize and/or including the magnitude and distance histograms but this did not improve the results. Therefore we have decided to fix the thick disc fraction to 5.5% *of the thin disc fraction*, which corresponds to the $5.6 \pm 1\%$ derived by Robin et al. (1996). The thin disc fraction was chosen between 0 and 1, while the halo fraction was one minus the thin disc and thick disc fractions. Then we solved for the thin disc fraction and multiplication factor. The normalized χ^2 contours of the fit are given in Fig. 6.6 showing the total disc fraction vs the total space density for each of the absolute magnitude bins with the dotted line indicating $\chi^2 = 2$. The best values are given in Table 6.3. The average percentages of the three populations that fit our observed sample best are 92.4% thin disc, 5.1%

thick disc and 2.5% halo which corresponds to an overall space density of $6.5 \cdot 10^{-5}$ pc^{-3} (Note that this thick disc fraction is 5.1% of the *total* population). The observed histograms together with the scaled simulated histograms of u, v, and w are shown in Fig. 6.7.

The overall distributions of the simulated histograms fit very well with the observed ones (χ^2 given in Table 6.3). From the resulting numbers of the fitting procedure we find that for these two absolute magnitude bins, the resulting halo fraction is large, 29–39% in the proper motion limited sample (for the other three absolute magnitude bins 9–13%). Furthermore, these bins have a relative low number of observed objects.

Cabrera-Lavers et al. (2005, and references therein) argue that the thick disc fraction ranges between 2% to 10% of the thin disc fraction. By using these fractions for the thick disc, the overall space density changes from $6.1 \cdot 10^{-5}$ to $6.6 \cdot 10^{-5}$ pc^{-3}, where the highest space density is derived by using 4.5% for the thick disc fraction and the lowest value by using 10%. The thick disc fraction of Robin et al. (1996) is in between these values, so here we will use the fraction of 5.5% of the thin disc fraction as well. As mentioned before, about 85% of the observed objects are probably real binaries. Correcting our space density for this, we obtain the value of $5.5 \cdot 10^{-5}$ pc^{-3}. We can see from the results in Table 6.3 that the faintest three absolute magnitude bins have the highest contribution to the overall space density. Together with the $\Delta\chi^2 = 1$ contour plots (dotted lines) in Fig. 6.6 we estimate the uncertainty on the overall space density to be $\sim 1 \cdot 10^{-5}$ pc^{-3}. With the resulting fractions and space density, we derived that we should have seen ~ 1150 objects if there was no proper motion limit present. We have observed 418 objects, which implies that, with the proper motion limit of 20 mas yr^{-1}, we have seen only $\sim 35\%$ of the total number of white dwarf–red dwarf binaries present in the selected area.

6.6 Discussion

The space density of white dwarf-red dwarf binaries derived from our study is a factor of two larger than the upper value determined by Schreiber & Gänsicke (2003), i.e. $6 - 30 \cdot 10^{-6}$ pc^{-3}. The difference can be explained by the fact that they have only used post-common-envelope binaries to determine their space density and we have included all binaries,
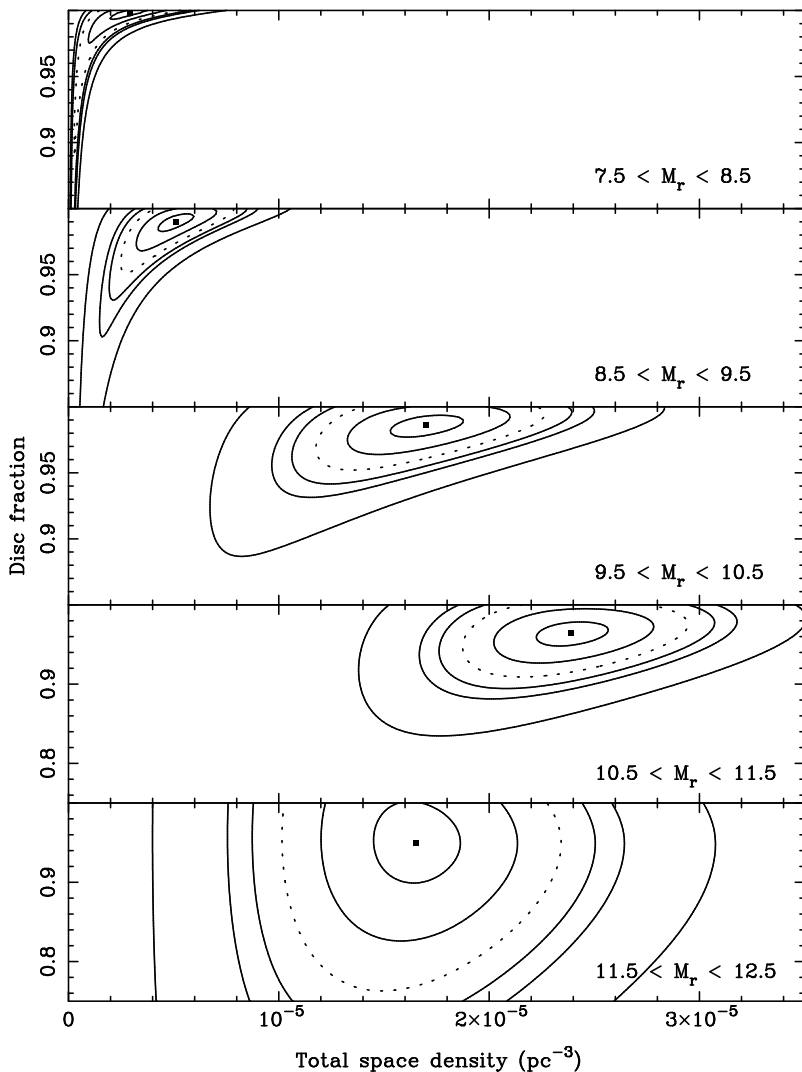
Figure 6.6: *Normalized χ^2 contours of the fit where the thick disc fraction is fixed to 0.055 times the thin disc fraction and the χ^2 values are normalised. The dotted contour line corresponds to $\chi^2 = 2$. The panels show from top to bottom the different absolute magnitude bins.*

Table 6.3: *Best fractions and multiplication factor for each of the magnitude bins for our selection. The thick disc fraction is taken as 0.055 times the thin disc fraction. The resulting χ^2 is given as well.*

Magnitude bin	f_{thin}	f_{thick}	f_{halo}	Space density (pc^{-3})	χ^2
7.5–8.5	0.943	0.052	0.005	$2.90 \cdot 10^{-6}$	0.62
8.5–9.5	0.936	0.051	0.013	$5.10 \cdot 10^{-6}$	0.60
9.5–10.5	0.932	0.051	0.017	$1.70 \cdot 10^{-5}$	1.01
10.5–11.5	0.911	0.050	0.039	$2.39 \cdot 10^{-5}$	0.52
11.5–12.5	0.898	0.049	0.053	$1.65 \cdot 10^{-5}$	0.54
Average	0.924	0.051	0.025	-	

Table 6.4: *Space densities in pc^{-3} for the thin disc, thick disc and halo fractions for each of the absolute magnitude bins. The total space density for each of the absolute magnitude bins is also given.*

Magnitude bin	Population	Space density (pc^{-3})	Total space density (pc^{-3})
7.5–8.5	Thin	$2.74 \cdot 10^{-6}$	
	Thick	$1.50 \cdot 10^{-7}$	$2.90 \cdot 10^{-6}$
	Halo	$2.46 \cdot 10^{-8}$	
8.5–9.5	Thin	$4.77 \cdot 10^{-6}$	
	Thick	$2.62 \cdot 10^{-7}$	$5.10 \cdot 10^{-6}$
	Halo	$6.63 \cdot 10^{-8}$	
9.5–10.5	Thin	$1.58 \cdot 10^{-5}$	
	Thick	$8.71 \cdot 10^{-7}$	$1.70 \cdot 10^{-5}$
	Halo	$2.89 \cdot 10^{-7}$	
10.5–11.5	Thin	$2.18 \cdot 10^{-5}$	
	Thick	$1.20 \cdot 10^{-6}$	$2.39 \cdot 10^{-5}$
	Halo	$9.30 \cdot 10^{-7}$	
11.5–12.5	Thin	$1.48 \cdot 10^{-5}$	
	Thick	$8.15 \cdot 10^{-7}$	$1.65 \cdot 10^{-5}$
	Halo	$8.72 \cdot 10^{-7}$	
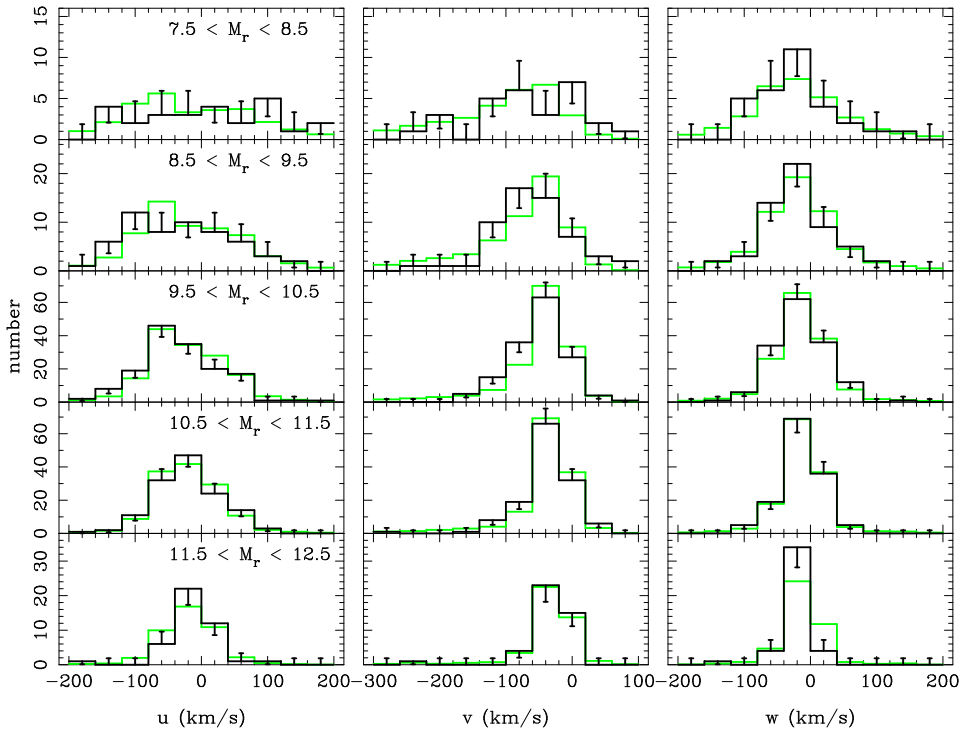
Figure 6.7: *Observed (black) and simulated (green/grey) histograms for the distributions in u, v, and w by using the best values for the fractions of the different simulated populations and multiplication factor.*

also those that might not have gone through a common-envelope phase. In their paper, they quote their value as a lower limit thus it is not necessarily in disagreement with ours.

Willems & Kolb (2004) have derived from theory a general space density for white dwarf–main-sequence star binaries, which include all spectral types and not only the M stars we are studying in this paper. In their Fig. 13 they show what fraction of all the white dwarf–main-sequence star binaries has a ratio of the white dwarf luminosity over the main-sequence star luminosity larger than a certain value for their model A, which uses a flat initial mass ratio distribution ($n(q)$ with q the ratio between the mass of the main-sequence star and the mass of the progenitor of the white dwarf). The

white dwarf–red dwarf binaries studied in our sample have around equal luminosity. From their Fig. 13 we then derive that a fraction of ∼0.03 of their total population corresponds to the binaries we have studied here. Here we will assume that this fraction is not dependent on their different models or their initial mass ratio distributions. Depending on the initial mass ratio distribution that Willems & Kolb (2004) use, the corresponding theoretical space density for white dwarf–red dwarf binaries ranges from $3.6 \cdot 10^{-6}$ (using $n(q) \propto q^{-0.99}$, $0 < q \leq 1$) to $1.6 \cdot 10^{-4}$ pc^{-3} (using a secondary mass taken from the same initial mass function as the primary). Our observed space density of $5.5 \cdot 10^{-5}$ pc^{-3} is in agreement with these theoretical values and corresponds best with their value of $7.8 \cdot 10^{-5}$ pc^{-3} for an initial mass ratio distribution $n(q) \propto q$, $0 < q \leq 1$.

For (apparently) single white dwarfs from the SPY survey, Pauli et al. (2006) have determined that 2% of the white dwarfs belong to the halo and 7% to the thick disc. Depending on the thick disc fraction that we use, the fraction of halo binaries varies between 2 and 3%. Using the thick disc value for which 7% of the *total* population of binaries belong to the thick disc, results in 3% of the binaries being halo objects, which is in agreement with the values for single white dwarfs.

The space density for hydrogen-rich white dwarfs in the SDSS with temperatures <48 000 K is $1.94 \cdot 10^{-3}$ pc^{-3} (Hu et al. 2007). Maxted & Marsh (1999) find that ∼10% of the hydrogen-rich white dwarfs are double degenerates, resulting in a space density of $1.94 \cdot 10^{-4}$ pc^{-3}. This is ∼3 times the space density that we found for white dwarf–red dwarf binaries. As mentioned before, only ∼0.03 of all the theoretical white dwarf–main-sequence binaries of Willems & Kolb (2004) are studied in our sample. A large fraction of white dwarf–main-sequence binaries may evolve to double degenerate systems. Therefore, it is not surprising that the space density for double degenerates is larger than the white dwarf–red dwarf binaries, but a more detailed study is needed.

The observed volume mass density for main-sequence stars with $0.08 < M < 1 M_\odot$ is 0.036 $M_\odot$ pc^{-3} (Kroupa et al. 1993). About 60% of these have a mass between 0.15 and 0.55 $M_\odot$ which corresponds to about spectral types M0 to M6 (the spectral range considered in this study). The average mass in the range $0.08 < M < 1 M_\odot$ when using a Kroupa initial mass function (Kroupa et al. 1993) is 0.3 $M_\odot$. This gives a space density of $7 \cdot 10^{-2}$ pc^{-3}. This value is much higher than the space density for white dwarf–red dwarf

binaries determined here and in previous studies. This implies that only ~ 1 in $1\,000$ red dwarfs has an observable white dwarf companion.

The proper motion catalogue of Gould & Kollmeier (2004) used in this analysis was produced by using DR1 of the SDSS. The footprint of DR5 is ~ 4 times larger than for DR1. At first approximation we would expect our sample to be ~ 4 times larger as well, when using a proper motion catalogue based on DR5. With this larger sample it might be possible to disentangle the thin disc and thick disc distributions which was not possible with our present sample. Also deriving the radial velocities for the objects might improve the disentangling between thin disc and thick disc.

In order to use this sample of binary systems to determine fundamental parameters of the common-envelope phase, we would need to know the orbital parameters of the binaries, e.g. orbital periods, orbital separations, masses of the binary components. This requires an extensive follow-up effort. With this series of papers we have laid down the ground for this study to be carried out. A suitable, complete, sample of white dwarf-red dwarf binaries has been identified. A method to find and classify these type of binaries has been developed. Future spectroscopic follow-up of this sample will allow us to further constrain the common-envelope evolution.

Acknowledgements

Bibliography

Abt, H. A. 1983, ARA&A, 21, 343

Adams, W. S. 1925, The Observatory, 48, 337

Adelman-McCarthy, J. K. 2007, VizieR Online Data Catalog

Augusteijn, T., Greimel, R., van den Besselaar, E. J. M., & Groot, P. J. 2007, submitted to A&A, (Chapter 4)

Bergeron, P., Saumon, D., & Wesemael, F. 1995, ApJ, 443, 764

Bergeron, P., Wesemael, F., & Fontaine, G. 1991, ApJ, 367, 253

Bessel, F. W. 1844, MNRAS, 6, 136

Bessell, M. S., Castelli, F., & Plez, B. 1998, A&A, 333, 231

Binney, J. & Merrifield, M. 1998, Galactic astronomy (Princeton University Press)

Bochanski, J. J., West, A. A., Hawley, S. L., & Covey, K. R. 2007, AJ, 133, 531

Bond, G. 1862, Astronomische Nachrichten, 57, 131

Brinkworth, C. S., Marsh, T. R., Dhillon, V. S., & Knigge, C. 2006, MNRAS, 365, 287

Bruch, A. 1999, AJ, 117, 3031

Cabrera-Lavers, A., Garzón, F., & Hammersley, P. L. 2005, A&A, 433, 173

Campbell, W. W. 1920, PASP, 32, 199

Chiba, M. & Beers, T. C. 2000, AJ, 119, 2843

de Jager, C., Heise, J., Avgoloupis, S., et al. 1986, A&A, 156, 95

de Jager, C., Heise, J., van Genderen, A. M., et al. 1989, A&A, 211, 157

de Kool, M. 1992, A&A, 261, 188

de Kool, M. & Ritter, H. 1993, A&A, 267, 397

de Kool, M., van den Heuvel, E. P. J., & Pylyser, E. 1987, A&A, 183, 47

Dehnen, W. & Binney, J. J. 1998, MNRAS, 298, 387

Dewi, J. D. M. & Tauris, T. M. 2000, A&A, 360, 1043

Dhillon, V. & Marsh, T. 2001, New Astronomy Review, 45, 91

Digby, A. P., Hambly, N. C., Cooke, J. A., Reid, I. N., & Cannon, R. D. 2003, MNRAS, 344, 583

Eddington, A. S. 1924, MNRAS, 84, 308

Eggleton, P. P. 1983, ApJ, 268, 368

Eisenhauer, F., Schödel, R., Genzel, R., et al. 2003, ApJ, 597, L121

Eisenstein, D. J., Liebert, J., Harris, H. C., et al. 2006, ApJS, 167, 40

Fan, X. 1999, AJ, 117, 2528

Finley, D. S., Koester, D., & Basri, G. 1997, ApJ, 488, 375

Friedrich, S., Koester, D., Christlieb, N., Reimers, D., & Wisotzki, L. 2000, A&A, 363, 1040

Fuhrmann, K. 2004, Astronomische Nachrichten, 325, 3

Fukugita, M., Ichikawa, T., Gunn, J. E., et al. 1996, AJ, 111, 1748

Gehrels, N. 1986, ApJ, 303, 336

Gould, A. 2007, private communication

Gould, A. & Kollmeier, J. A. 2004, ApJS, 152, 103

Grebel, E. K. 2001, in Reviews in Modern Astronomy, Vol. 14, Reviews in Modern Astronomy, ed. R. E. Schielicke, 223–243

Green, P. J., Ali, B., & Napiwotzki, R. 2000, ApJ, 540, 992

Green, R. F., Schmidt, M., & Liebert, J. 1986, ApJS, 61, 305

Greenstein, J. 1975, ApJ, 196, L117

Haefner, R. 1989, A&A, 213, L15

Harris, H., Liebert, J., Kleinman, S., et al. 2003, AJ, 126, 1023

Hawley, S. L., Covey, K. R., Knapp, G. R., et al. 2002, AJ, 123, 3409

Holmes, S. & Samus, N. 2001, Journal of the American Association of Variable Star Observers (JAAVSO), 29, 148

Homeier, D., Koester, D., Hagen, H.-J., et al. 1998, A&A, 338, 563

Hu, Q., Wu, C., & Wu, X.-B. 2007, A&A, 466, 627

Hurley, J. R., Pols, O. R., & Tout, C. A. 2000, MNRAS, 315, 543

Hussey, W. J. 1896, PASP, 8, 183

Iben, I. & Livio, M. 1993, PASP, 105, 1373

Johnson, D. R. H. & Soderblom, D. R. 1987, AJ, 93, 864

Kalirai, J. S., Richer, H. B., Hansen, B. M. S., Reitzel, D., & Rich, R. M. 2005, ApJ, 618, L129

King, A. R. 1988, QJRAS, 29, 1

Kirkpatrick, J. D., Henry, T. J., & McCarthy, D. W. 1991, ApJS, 77, 417

Kirkpatrick, J. D., Kelly, D. M., Rieke, G. H., et al. 1993, ApJ, 402, 643

Kleinman, S., Harris, H., Eisenstein, D., et al. 2004, ApJ, 607, 426

Koester, D. 1972, A&A, 16, 459

Koester, D. & Wolff, B. 2000, A&A, 357, 587

Kothari, D. S. 1932, MNRAS, 93, 61

Kroupa, P., Tout, C. A., & Gilmore, G. 1993, MNRAS, 262, 545

Liebert, J., Wesemael, F., Hansen, C., et al. 1986, ApJ, 309, 241

Margon, B., Anderson, S. F., Harris, H. C., et al. 2002, AJ, 124, 1651

Marsh, T. R. 2000, New Astronomy Review, 44, 119

Maxted, P. F. L. & Marsh, T. R. 1999, MNRAS, 307, 122

Maxted, P. F. L., Marsh, T. R., Morales-Rueda, L., et al. 2004, MNRAS, 355, 1143

McCook, G. P. & Sion, E. M. 1999, ApJS, 121, 1

Mishenina, T. V., Soubiran, C., Kovtyukh, V. V., & Korotin, S. A. 2004, A&A, 418, 551

Moffett, T., Barnes, T., & Evans, D. 1985, in IAU Symp. 111: Calibration of Fundamental Stellar Quantities, 365–368

Monet, D. G., Levine, S. E., Canzian, B., et al. 2003, AJ, 125, 984

Morales-Rueda, L., Marsh, T. R., Maxted, P. F. L., et al. 2005, MNRAS, 359, 648

Napiwotzki, R., Karl, C. A., Nelemans, G., et al. 2005, in ASP Conf. Ser. 334: 14th European Workshop on White Dwarfs, ed. D. Koester & S. Moehler, 375

Nelemans, G. & Tout, C. A. 2005, MNRAS, 356, 753

O'Donoghue, D., Koen, C., Kilkenny, D., et al. 2003, MNRAS, 345, 506

Paczyński, B. 1976, in IAU Symp. 73: Structure and Evolution of Close Binary Systems, 75–80

Panei, J. A., Althaus, L. G., & Benvenuto, O. G. 2000, A&A, 353, 970

Pauli, E.-M., Napiwotzki, R., Altmann, M., et al. 2003, A&A, 400, 877

Pauli, E.-M., Napiwotzki, R., Heber, U., Altmann, M., & Odenkirchen, M. 2006, A&A, 447, 173

Pickles, A. 1998, PASP, 110, 863

Pourbaix, D., Ivezić, Ž., Knapp, G. R., Gunn, J. E., & Lupton, R. H. 2004, A&A, 423, 755

Raymond, S., Szkody, P., Hawley, S., et al. 2003, AJ, 125, 2621

Reid, I. N., Hawley, S. L., & Gizis, J. E. 1995, AJ, 110, 1838

Reid, M. J. 1993, ARA&A, 31, 345

Ritter, H. & Kolb, U. 2003, A&A, 404, 301

Robb, R. M. & Greimel, R. 1997, Informational Bulletin on Variable Stars, 4486, 1

Robin, A. C., Haywood, M., Creze, M., Ojha, D. K., & Bienayme, O. 1996, A&A, 305, 125

Schreiber, M. R. & Gänsicke, B. T. 2003, A&A, 406, 305

Schrijver, C. J. & Zwaan, C. 2000, Solar and Stellar Magnetic Activity (Solar and stellar magnetic activity (Cambridge astrophysics series))

Silvestri, N. M., Hawley, S. L., West, A. A., et al. 2006, AJ, 131, 1674

Silvestri, N. M., Oswalt, T. D., Wood, M. A., et al. 2001, AJ, 121, 503

Smith, J. A., Tucker, D. L., Kent, S., et al. 2002, AJ, 123, 2121

Smolčić, V., Ivezić, Ž., Knapp, G. R., et al. 2004, ApJ, 615, L141

Taam, R. E. & Sandquist, E. L. 2000, ARA&A, 38, 113

Tas, G., Sipahi, E., dal, H. A., et al. 2004, Informational Bulletin on Variable Stars, 5548, 1

van den Besselaar, E. J. M., Augusteijn, T., Greimel, R., et al. 2007a, submitted to A&A, (Chapter 5)

van den Besselaar, E. J. M., Groot, P. J., Deacon, N. R., et al. 2007b, submitted to A&A, (Chapter 6)

van den Besselaar, E. J. M., Roelofs, G. H. A., Nelemans, G. A., Augusteijn, T., & Groot, P. J. 2005, A&A, 434, L13, (Chapter 2)

Verbunt, F. & Rappaport, S. 1988, ApJ, 332, 193

Verbunt, F. & Zwaan, C. 1981, A&A, 100, L7

Voges, W., Aschenbach, B., Boller, T., et al. 1999, A&A, 349, 389

Wachter, S., Hoard, D. W., Hansen, K. H., et al. 2003, ApJ, 586, 1356

Wagner, R., Sion, E., Liebert, J., & Starrfield, S. 1988, ApJ, 328, 213

Webbink, R. F. 1984, ApJ, 277, 355

Wesemael, F., Greenstein, J. L., Liebert, J., et al. 1993, PASP, 105, 761

Willems, B. & Kolb, U. 2004, A&A, 419, 1057

Wood, M. A. 1995, in LNP Vol. 443: White Dwarfs, ed. D. Koester & K. Werner, 41–45

York, D., Adelman, J., Anderson, J., et al. 2000, AJ, 120, 1579

Summary

This thesis presents several studies on white dwarf–red dwarf populations in our Galaxy. Several stages of binary evolution are not yet well understood, such as the common-envelope phase. White dwarf–red dwarf binaries are almost ideal objects to study the effects of this phase thanks to their relative simple spectra, they are detached, and their periods have not changed much since they came out of the common-envelope phase. Therefore, an effective selection method for finding these binaries is crucial. The selected binaries can then be used to determine the Galactic space density of white dwarf–red dwarf binaries which can then be compared with binary population models.

In contrast to the known white dwarf–red dwarf binaries, which almost all contain a hydrogen-rich white dwarf (DA), in Chapter 2 thirteen binaries with a helium-rich white dwarf (DB) are found by using a colour selection in the Sloan Digital Sky Survey (SDSS) photometric database and by using the equivalent widths of the helium lines in the SDSS spectra. For single white dwarfs the fraction of DB/DA is 9-15% while the fraction for white dwarfs in binaries is found to be $\sim 5\%$. The origin of the difference between the fraction of single DB white dwarfs and DB white dwarfs in binaries is not known, but might be due to binary evolution. Furthermore, spectral fitting indicates that a fraction of the white dwarfs in the binaries found in Chapter 2 might be in the so called DB-gap, a temperature range between 30 000–45 000 K in which only a few single DB white dwarfs are found.

A detailed study of the eclipsing white dwarf–red dwarf binary DE CVn is given in Chapter 3. Photometric and spectroscopic data from a number of instruments on a number of telescopes are combined to derive the

temperature of the white dwarf ($8\,000 \pm 1\,000$ K) and the spectral type of the red dwarf (M3). Furthermore, the mass and radius of the white dwarf are determined as $0.51^{+0.06}_{-0.02}$ solar masses and $0.0136^{+0.0008}_{-0.0002}$ solar radii, respectively. The values for the red dwarf are 0.41 ± 0.06 solar masses and $0.37^{+0.06}_{-0.007}$ solar radii. The orbital separation is $2.07^{+0.09}_{-0.04}$ solar radii and the inclination is 86^{+3}_{-2} °. From the short orbital period combined with these results it is concluded that DE CVn went through a common-envelope phase sometime in its past.

In the remaining chapters we used the SDSS database to establish a new way to select white dwarf–red dwarf binaries in our Galaxy, which is based on proper motions and SDSS colours. The selection method itself is described in Chapter 4. The catalog of Gould & Kollmeier (2004), which consist of all the objects in the intersection between the SDSS Data Release 1 (DR1) and the USNO-B1.0 that have a proper motion of $\geq$20 mas yr^{-1} and $r{\leq}20$, is used as a basis for our investigations. A proper motion selection is needed to remove the quasars from the sample as they occupy the same colour space, but they should not show a measurable proper motion. Several colour selections were tested on the spectroscopic database of DR5 to include as many real binaries as possible and to remove an as large as possible fraction of non-binaries. It is concluded that the best method is to take objects that are $\geq 3\sigma$ above the main-sequence in the $(u - g)$ vs. $(g - r)$ diagram *and* $\geq 4\sigma$ above the main-sequence in the $(g - r)$ vs. $(r - i)$ diagram.

In Chapter 5, the objects selected using these criteria that have spectra in the SDSS DR5 are discussed. Binary template spectra are created by adding a white dwarf model to a red dwarf template where the individual spectra are first scaled to a common distance to form a physical binary. The SDSS spectra are then fitted with these binary templates. The model with the lowest χ^2 is taken as the best fit and used to classify the objects. To indicate where one would find white dwarf–red dwarf binaries with a certain combination of white dwarf temperature and secondary spectral type, tracks are obtained in colour-colour diagrams (Chapter 4). These tracks are used in the 3-dimensional $(u - g)$, $(g - r)$, $(r - i)$ colour space to classify the same objects that are studied in the spectroscopic investigation, but now on the basis of their colours alone. The results from the photometry and the spectroscopy are in very good agreement.

The consistency between the spectroscopic and photometric classifica-

tion allows us to use the whole photometric sample in Chapter 6 and classify each object on the basis of its colours alone. The sample is studied as a whole instead of each object individually. To estimate the missing fraction of binaries due to the proper motion cutoff applied to the data, we simulate the complete Galactic population by using a theoretical model of our Galaxy. The model and the sample itself were combined to determine the space density of white dwarf–red dwarf binaries in the Galaxy. To determine the fractions and space density reliably we needed to fix the thick disc fraction to a certain value. We have chosen to use 5.5% of *the thin disc fraction* as the thick disc fraction, which corresponds to the value of $5.6 \pm 1\%$ of Robin et al. (1996). This gives us a best fit model consisting of 92.4% thin disc objects, 5.1% thick disc objects, and 2.5% halo objects. The corresponding space density is $5.5 \cdot 10^{-5}$ pc^{-3} which is in agreement with the theoretical range of $3.6 \cdot 10^{-6}$ to $1.6 \cdot 10^{-4}$ pc^{-3} (Willems & Kolb 2004).

Samenvatting

A.1 Introductie van sterren

Een ster zoals de Zon is een gasbol bestaande uit voornamelijk waterstof ($\sim$70%), helium ($\sim$28%) en een kleine fractie zwaardere elementen, metalen genoemd in de sterrenkunde ($\sim$2%). De temperatuur en dichtheid in de kern van een ster zijn zo hoog dat er waterstoffusie plaatsvindt, waarbij helium wordt gevormd. De warmte die daarbij geproduceerd wordt, zorgt voor een druk die het ineenkrimpen door de zwaartekracht tegen houdt, waardoor de ster in evenwicht is. Wanneer de waterstof in de kern op is, stopt de fusie en gaat de kern samentrekken waarbij de temperatuur en de druk in de kern oplopen. In deze fase zullen de buitenlagen van de ster uit gaan zetten tot het formaat van een reus met een straal van enkele tot honderden zonsstralen. Voor sterren met een beginmassa $\gtrsim$0.5 zonsmassa's zullen de temperatuur en druk zover oplopen dat heliumfusie begint en een koolstof–zuurstof kern wordt gevormd.

Wanneer de heliumfusie in de kern van de ster gestopt is, gaat de kern samentrekken terwijl de buitenlagen verder uitzetten waardoor de ster opnieuw een reus wordt, met een straal van enkele tot honderden zonsstralen. De buitenlagen worden verwijderd door pulsaties vanwege instabiliteiten in de ster. Voor sterren met een beginmassa van $\lesssim$8–11 zonsmassa's wordt het ineenkrimpen van de kern gestopt door gedegenereerde elektronendruk waardoor er een compacte koolstof–zuurstof kern overblijft. Deze zal uiteindelijk afkoelen tot een witte dwerg. Voor sterren met een hogere beginmassa vindt er uiteindelijk een supernova explosie plaats waarbij een neutronenster of zwart gat gevormd wordt, maar dit zijn objecten waar in dit proefschrift

geen onderzoek naar gedaan is.

De distributie van sterren met een bepaalde beginmassa volgt de zoge-
noemde Salpeter functie. Dit houdt in dat er meer sterren gevormd worden
met een lage massa dan sterren met een hoge massa. Van alle sterren die
gevormd zijn, heeft $\sim$90% een massa van $\lesssim$8–11 zonsmassa's. Vanwege de
zwaartekracht zijn de temperatuur en de druk in de kernen van zware ster-
ren hoger dan voor lichte sterren. Hierdoor gaat de fusie sneller en evolueert
de ster ook sneller. De tijdschaal voor waterstoffusie in een ster van 5 zons-
massa's is ongeveer 100 miljoen jaar, terwijl de tijdschaal voor waterstoffusie
voor een ster van 0.5 zonsmassa's ongeveer 65 miljard jaar is. Vanwege de
eindige leeftijd van het heelal kunnen alleen sterren met een beginmassa
$\geq 0.8 - 0.9$ zonsmassa's ge-evolueerd zijn.

A.1.1 Witte dwergen

Nadat de fusie in de kern van een ster met een beginmassa van $\lesssim$8–11 zons-
massa's gestopt is en de buitenlagen verwijderd zijn, blijft de kern van de
ster over. Over het algemeen bestaat deze voornamelijk uit koolstof en zuur-
stof met een dunne mantel van waterstof of helium. De massa van de kern
is ongeveer een halve zonsmassa terwijl de kern ongeveer zo groot is als de
Aarde. Dit is een zeer compact object dat een witte dwerg wordt genoemd.
De witte dwerg bestaat uit gedegenereerde materie, wat betekent dat de
druk niet afhankelijk is van de combinatie van dichtheid en temperatuur,
zoals in een normaal gas, maar alleen van de dichtheid.

Een witte dwerg wordt geboren met een oppervlakte temperatuur van
ongeveer 100 000 K waarna deze langzaam afkoelt. Het duurt ongeveer 0.8
miljard jaar om af te koelen tot 8 000 K. De koelste witte dwergen die gevon-
den zijn, hebben een temperatuur van een paar duizend Kelvin. De kleur en
intensiteit van een witte dwerg worden bepaald door de temperatuur; een
hete witte dwerg is blauwer en heeft een hogere intensiteit dan een koele
witte dwerg.

Wanneer een witte dwerg spectroscopisch wordt waargenomen, zien we
een blauwe ster met brede absorptielijnen van waterstof of helium, afhan-
kelijk van de samenstelling en temperatuur van de mantel, die veroorzaakt
worden door de hoge zwaartekracht en druk. Een voorbeeld van een spec-
trum is te zien in Fig. A.1 waarbij de brede absorptielijnen van waterstof
duidelijk zichtbaar zijn.
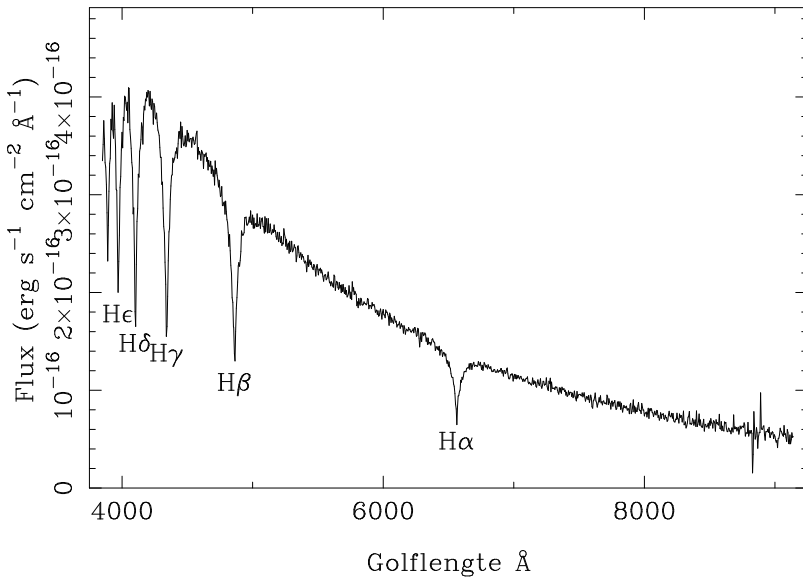
Figuur A.1: *Een voorbeeld van een witte dwerg spectrum met absorptielijnen van waterstof. Dit is SDSS J110326.70+003725.8, een witte dwerg met een temperatuur van 10 000 K en een zwaartekracht van* $\log g = 8.0$.

Classificatie van witte dwergen

Over het algemeen worden witte dwergen geclassificeerd aan de hand van de lijnen in het spectrum die veroorzaakt worden door de samenstelling en temperatuur van de dunne mantel boven de gedegenereerde kern. De overgrote meerderheid van alle alleenstaande witte dwergen ($\sim$85%) vertoont waterstoflijnen en deze sterren worden DA witte dwergen genoemd. Een tweede groep wordt gevormd door witte dwergen die heliumlijnen vertonen, de DB witte dwergen ($\sim$8%). Andere groepen zijn witte dwergen waarvan het spectrum helemaal geen lijnen vertoont (DC, $\sim$3%), koolstoflijnen vertoont (DQ, $\sim$1%) of metaallijnen (elementen zwaarder dan waterstof, helium en koolstof) vertoont (DZ, $\sim$1%). Verder komen er ook witte dwergen voor die een combinatie van lijnen van verschillende elementen in het spectrum hebben, zoals bijvoorbeeld waterstof en helium (DAB).
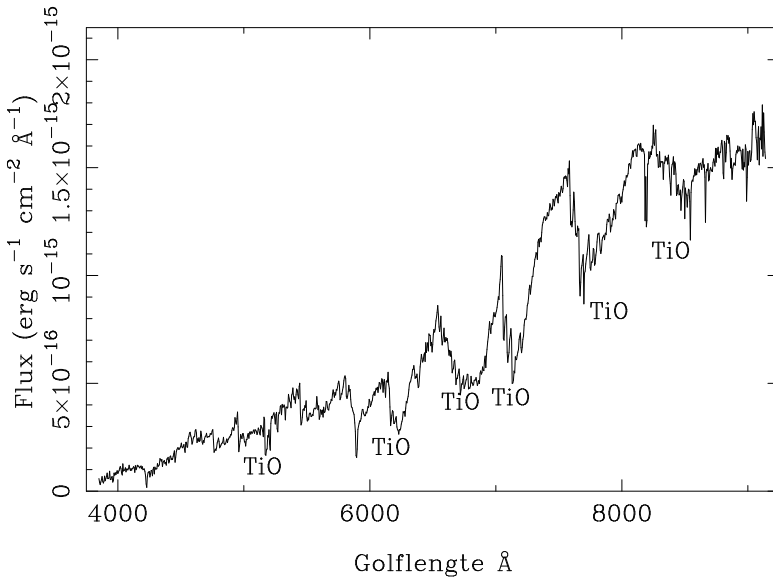
Figuur A.2: *Dit is een voorbeeld van een rode dwerg waarbij de titanium oxide banden zichtbaar zijn. Dit is SDSS J024727.29+010751.7, een ster met spectraal type M3.*
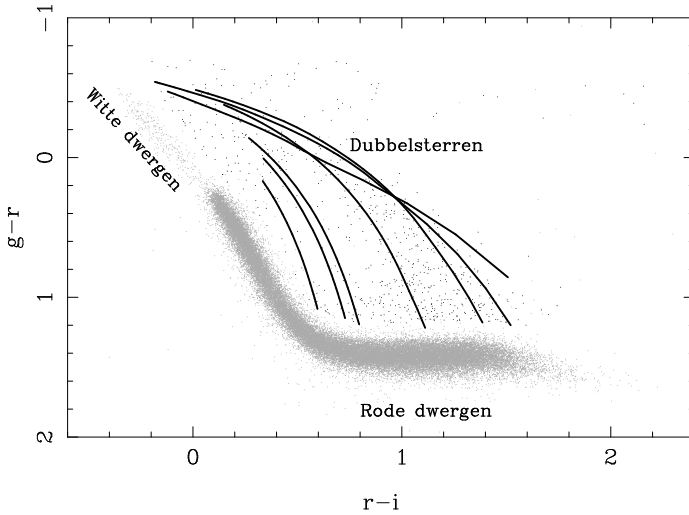
A.1.2   Rode dwergen

De classificatie van waterstoffuserende sterren wordt gedaan aan de hand van de temperatuur. Hete, zware sterren ($\sim$50 000 K, 60 zonsmassa's) hebben spectraal type O. Koelere, lichtere sterren gaan, via spectraal types B, A, F, G, K naar spectraal type M. Elk spectraal type is onderverdeeld in een aantal subtypes, waarbij de Zon bijvoorbeeld een G2 ster is. Sterren met spectraal type M hebben een massa van $\lesssim$0.5 zonsmassa en worden rode dwergen genoemd. Voor deze sterren is de tijdschaal voor waterstoffusie zo groot, dat ze nog niet tot witte dwergen ge-evolueerd kunnen zijn.

De oppervlakte temperatuur van een rode dwerg is ongeveer 3 000 K wat laag genoeg is om molekulen in de atmosfeer te vormen, voornamelijk titanium-oxide. Deze molekulen produceren absorptiebanden in het spectrum die zeer herkenbaar zijn. Een voorbeeld van een rode dwerg is te zien in Fig. A.2.
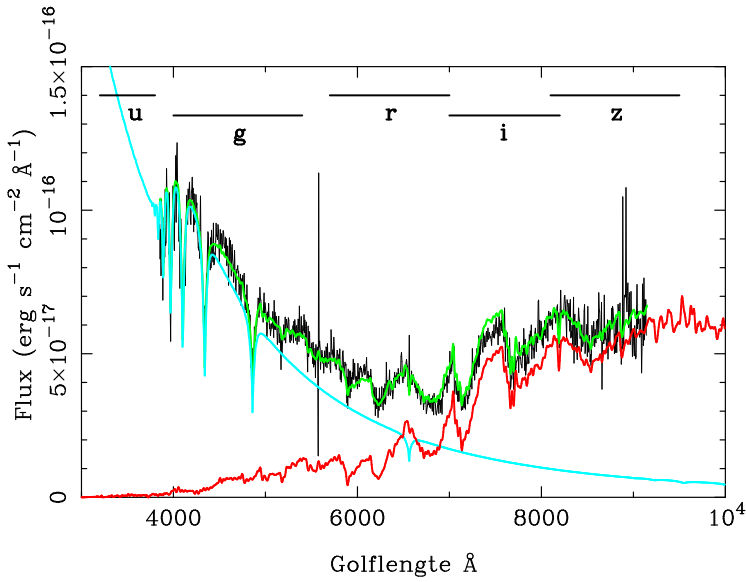
Figuur A.3: *Dit is een voorbeeld van een rode dwerg–witte dwerg dubbelster. Dit is SDSS J145527.72+611504.6 waarvan de witte dwerg een temperatuur van 22 000 K heeft en $\log g$ van 7.5 heeft (domineert in het blauwe gebied) en de rode dwerg een spectraal type M4 heeft (domineert in het rode gebied). De groen/grijze lijn bovenop de zwarte lijn is de combinatie van de twee enkele sterren.*

Figuur A.4: *Kleur-kleur diagram met de hoofdreeks en de posities van enkele witte dwergen, enkele rode dwergen en dubbelsterren.*

A.2   Rode dwerg–witte dwerg dubbelsterren

In dit proefschrift heb ik dubbelsterren bestudeerd die bestaan uit een rode dwerg en een witte dwerg. Een witte dwerg is over het algemeen heter en kleiner dan de rode dwerg, waardoor ze intrinsiek een ongeveer even grote intensiteit hebben. Vanwege de contrasterende kleuren zijn dan ook beide objecten zichtbaar in het spectrum. Een voorbeeld van een spectrum van een rode dwerg–witte dwerg dubbelster is te zien in Fig. A.3. In dit figuur zijn ook de twee spectra van de afzonderlijke componenten te zien, alsmede het spectrum van de dubbelster, wat aantoont dat het waargenomen object inderdaad een rode dwerg–witte dwerg dubbelster is.

Wanneer een groot aantal sterren waargenomen wordt in een aantal breedbandige filters kunnen deze dubbelsterren heel gemakkelijk gevonden worden doordat de ene rood is en de andere blauw. In een kleur-kleur diagram, zoals Fig. A.4, vormen deze dubbelsterren een soort van brug tussen de posities van alleenstaande rode dwergen en alleenstaande witte dwergen. Dit maakt het relatief makkelijk om deze dubbelsterren te vinden.

A.3   Waarom willen we ze bestuderen?

In een dubbelster kan de aanwezigheid van de begeleider de evolutie van de sterren beïnvloeden. Rondom de sterren is een zogenoemde Roche geometrie aanwezig. Dichtbij de sterren zijn de equipotentiaal volumes nog vrijwel rond. Materiaal dat zich binnen zo'n volume bevindt, is gravitationeel gebonden aan de ster in dat volume. Verder van de ster af worden de equipotentiaal volumes vervormd tot een soort van druppels. Het kritieke volume waarbij een zadelpunt aanwezig is tussen de sterren, wordt de Roche Lobe genoemd (zie Fig. A.5).

Net als bij alleenstaande sterren evoleert de zwaardere ster in een dubbelster het snelst. Tijdens de evolutie zal de ster gaan uitzetten tot een reus met een typische straal van enkele tot honderden zonsstralen. Wanneer de beginperiode kort genoeg is ($\lesssim 10$ jaar) zal de reus groter willen worden dan zijn Roche Lobe. Als een ster zijn Roche Lobe volledig vult, zal er massa overdracht plaats gaan vinden via het zadelpunt, de ster "stroomt over". Hierdoor stroomt er materie van de reus naar de begeleider. Afhankelijk van de massa's van de sterren en de structuur van de reus kan de snelheid waar-
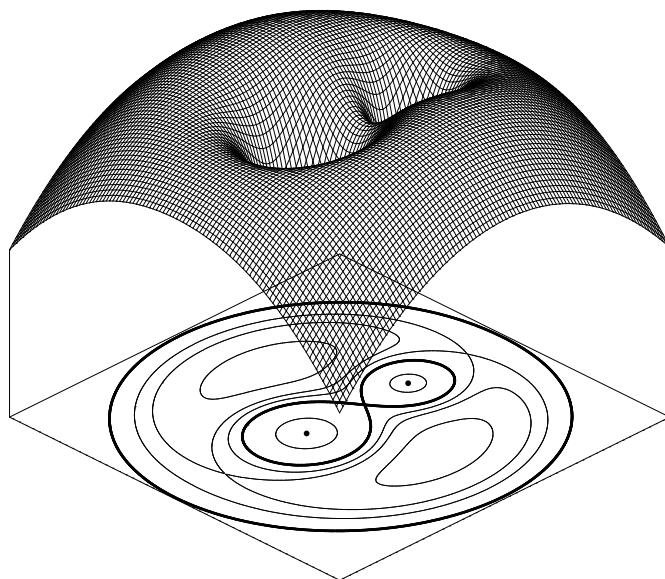
Figuur A.5: *De Roche geometry van een dubbelster. De Roche Lobe is het equipotentiaal oppervlak dat een acht-vormig figuur vormt. Auteur: Martin Heemskerk.*

mee de reus uitzet, en dus materie overdraagt naar de begeleider, zo hoog zijn dat de begeleider de materie niet snel genoeg kan verwerken en er al snel een gemeenschappelijke mantel zal ontstaat waarbij de begeleider zich binnen de reus bevindt. Dit wordt een common-envelope genoemd. Deze fase is één van de punten in dubbelster-evolutie die nog niet goed begrepen is. Als de buitenlagen weggeblazen zijn (de methode hiervan is ook nog vrij onbekend) en als dit gebeurt voordat de kern van de reus en de begeleider samensmelten, kan er een compacte dubbelster ontstaan, bestaande uit de kern van de oorspronkelijk zwaarste ster en de begeleider. De kern van de oorspronkelijk zwaarste ster zal afkoelen tot een witte dwerg. Waneer de begeleider een lage massa ($\lesssim 0.5$ zonsmassa's) heeft, is er een rode dwerg–witte dwerg dubbelster gevormd.

Er wordt vermoed dat de fase waarin de begeleider zich in de mantel van de reus bevindt, op astronomische tijdschaal gezien, erg kort is ($\lesssim 1\,000$ jaar). De kans om een systeem in deze fase te vinden is dan ook erg klein, waardoor het bijna onmogelijk is om deze fase direct waar te nemen. Om

de effecten van deze gemeenschappelijke mantel te bestuderen en de fysica beter te begrijpen is het daarom beter om naar objecten te kijken die zeer waarschijnlijk zo'n fase met een gemeenschappelijke mantel hebben doorstaan. Dit soort systemen zien wij als dubbelsterren waarvan minstens een van beide componenten een compacte ster is en waarvan de huidige afstand tussen de twee sterren veel kleiner is dan de straal van de reus waaruit de compacte ster ontstaan is (normaal gesproken met baanperiodes $\lesssim 1$ dag).

In rode dwerg–witte dwerg dubbelsterren bevinden beide sterren zich binnen hun Roche Lobe, waardoor er geen massa-overdracht plaatsvindt en de spectra en kleuren van deze systemen dus vrij gemakkelijk te simuleren zijn. Vanwege de contrasterende kleuren van de twee componenten kunnen ze bovendien relatief gemakkelijk gevonden worden. Deze dubbelsterren kunnen het resultaat zijn van een fase met een gemeenschappelijke mantel en aangezien ze vrij gemakkelijk te simuleren zijn, zijn deze systemen ideaal om dubbelster-evolutie te bestuderen.

A.4   De Sloan Digital Sky Survey

Voor het grootste gedeelte van dit proefschrift heb ik gebruik gemaakt van de Sloan Digital Sky Survey (SDSS). De SDSS heeft ongeveer een vijfde van de hemel fotometrisch waargenomen in 5 optische filterbanden, u, g, r, i en z, die schematisch weergegeven zijn in Fig. A.3. Van ongeveer 1% van de objecten is ook een spectrum opgenomen. In dit proefschrift is gebruik gemaakt van zowel de fotometrische data als de spectroscopische data.

Het doel van de SDSS is voornamelijk het in kaart brengen en bestuderen van sterrenstelsels in het heelal. Een bijproduct is dat hierbij ook veel objecten in de Melkweg worden waargenomen en vanwege de 5 filters kan er al vrij snel een idee verkregen worden van de classificatie uit de kleuren van objecten. De magnitude-grens van de SDSS is ongeveer 22.3 in het r filter. Dit alles bij elkaar maakt de SDSS de grootste en diepste database van dit moment en dus uitermate geschikt voor het zoeken naar rode dwerg–witte dwerg dubbelsterren.

A.5   Rode dwerg–witte dwerg dubbelsterren zonder DA witte dwerg

In paragraaf A.1.1 is uitgelegd dat er verschillende soorten alleenstaande witte dwergen zijn. Voordat ik aan dit onderzoek begon, waren er een paar honderd rode dwerg–witte dwerg dubbelsterren bekend (inclusief diegene met lange of onbekende baanperioden) waarvan het overgrote merendeel een DA witte dwerg bevat. In de literatuur waren er slechts twee dubbelsterren bekend met een DB witte dwerg (GD 325 en CBS 47) en één dubbelster met een DC witte dwerg (EG 388).

Zoals hiervoor uitgelegd, zijn rode dwerg–witte dwerg dubbelsterren relatief makkelijk te selecteren aan de hand van hun kleuren. Helaas blijkt het zo te zijn dat deze kleuren ook overeen komen met quasars, de actieve kernen van sterrenstelsels die zo ver weg staan dat ze als puntbronnen waargenomen worden. Hierdoor is een selectie nodig op basis van kleuren zodat de meeste quasars buiten de selectie vallen, maar de dubbelsterren wel meegenomen worden.

Aan de hand van de SDSS fotometrische data werd gekeken wat een mogelijke selectie zou zijn. Van de objecten in die selectie werd achterhaald of er een spectrum van was genomen en zo ja, wat voor soort object het was. Op deze manier werd de kleur selectie verbeterd om zoveel mogelijk dubbelsterren mee te nemen en de quasars juist niet. Tijdens deze zoektocht werden er negen dubbelsterren gevonden waarin de witte dwerg een DB is (zie hoofdstuk 2). Hierdoor werd besloten om alle SDSS spectroscopische data te doorzoeken naar systemen die *en* blauw *en* rood *en* helium absorptielijnen hadden. Uiteindelijk zijn er 13 gevonden in de derde data release van de SDSS. Aan de hand van de kleur selectie blijkt dat ongeveer 5% van de witte dwergen in dubbelsterren een DB is, wat dus een groot verschil is met alleenstaande witte dwergen ($\sim$9%). De reden voor dit verschil zit waarschijnlijk in de dubbelster-evolutie, maar is niet precies bekend.

Er zijn vrijwel geen alleenstaande witte dwergen gevonden met een temperatuur tussen 30 000 en 45 000 K, de DB-gap. Het fitten van de rode dwerg–DB witte dwerg dubbelsterren met waargenomen witte dwergen met een bekende temperatuur uit de SDSS, suggereert dat 23% een witte dwerg temperatuur heeft hoger dan 30 000 K en nog eens 38% een temperatuur rond de 30 000 K. Om deze temperaturen beter te bepalen, zijn een betere

fit met modelspectra nodig samen met betere waargenomen spectra.

A.6   DE Canum Venaticorum

Om meer inzicht te krijgen in compacte dubbelsterren is een studie uit-
gevoerd van een specifiek systeem genaamd DE Canum Venaticorum (DE
CVn). Uit de literatuur was bekend dat dit een eclipserende rode dwerg–
witte dwerg dubbelster was. Met de hulp van een aantal onderzoekers uit
dit gebied is een grote hoeveelheid fotometrische en spectroscopische data
van DE CVn gecombineerd. Het onderzoek hiervan is beschreven in hoofd-
stuk 3. Uit alle data samen is bepaald dat de witte dwerg een temperatuur
heeft van $8\,000 \pm 1\,000$ K met een zwaartekracht $\log g = 7.5$. De rode dwerg
is een M3 ster. Vanwege de stralen, massa's en baanperiode van DE CVn
werd er geconcludeerd dat deze ster door een fase met een gemeenschap-
pelijke mantel is gegaan. Ook is er bepaald dat de voorloper van de witte
dwerg een ster met beginmassa van $\leq$1.6 zonsmassa's moet zijn geweest.

A.7   Selectie op basis van eigenbewegingen

Sterren staan niet stil, maar bewegen rond het centrum van de Melkweg
waarbij de snelheidsverdeling een bepaalde spreiding heeft rond een gemid-
delde waarde behorende bij een bepaalde positie in de Melkweg. Hierdoor
hebben sterren een snelheid ten opzichte van de Zon welke zich reflecteert
in een beweging van de ster aan de hemel wat de eigenbeweging wordt ge-
noemd. Deze eigenbeweging is dus afhankelijk van de intrinsieke snelheid
van de ster, de richting waarin de ster beweegt en de afstand tot de ster.

Rode dwerg–witte dwerg dubbelsterren konden geselecteerd worden op
basis van hun kleuren, maar zoals gezegd worden daar ook quasars mee
geselecteerd. Aangezien quasars de actieve kernen van sterrenstelsels zijn
die als puntbronnen waargenomen worden, staan ze buiten de Melkweg en
dus ver weg. Hierdoor zouden ze geen meetbare eigenbeweging moeten
hebben. Daarom is besloten om een selectie te maken op basis van de kleuren
in combinatie met de eigenbewegingen. Dit is gedaan aan de hand van
de catalogus van Gould & Kollmeier (2004), waarvoor zij gebruik hebben
gemaakt van de overlap tussen de eerste data release van de SDSS en de
USNO-B catalogus.

De hoofdreeks in een kleur-kleur diagram heeft een bepaalde breedte en een maat voor deze breedte wordt aangegeven met σ. Hoe verder een object van de hoofdreeks af ligt, en daarmee een grotere σ heeft, hoe minder kans het object heeft om toch een hoofdreeksster te zijn. In hoofdstuk 4 is besproken dat het voor het selecteren van rode dwerg–witte dwerg dubbelsterren het beste is om objecten te nemen die meer dan 3σ boven de hoofdreeks in het $(u - g)$ vs. $(g - r)$ diagram af liggen *en* 4σ boven de hoofdreeks in het $(g - r)$ vs. $(r - i)$ diagram.

In hoofdstuk 5 is de selectie genomen zoals hiervoor besproken, maar is er alleen gekeken naar objecten die ook een waargenomen spectrum hebben. Deze zijn gefit met modelspectra bestaande uit witte dwerg modellen gecombineerd met rode dwerg spectra. Hierbij zijn de rode dwerg en witte dwerg tegelijkertijd gefit, terwijl in andere studies eerst de witte dwerg gefit wordt, waarna het witte dwerg model spectrum van het waargenomen spectrum afgetrokken wordt en het overgebleven spectrum met rode dwerg modellen gefit wordt. In hoofdstuk 5 is er gebruik gemaakt van de witte dwerg modellen van Koester en van rode dwerg template spectra van Pickles. De temperatuur van de witte dwerg modellen loopt van $6\,000$ K naar $80\,000$ K en het spectraal type van de rode dwerg loopt van M0 naar M6. Voordat de beide componenten samengevoegd werden, zijn ze eerst naar een gemeenschappelijke afstand geschaald om een dubbelster te simuleren. Voor elk waargenomen spectrum is de combinatie met de laagste χ^2 (een maat voor hoe goed een fit is) genomen als beste fit.

Aan de hand van de modelspectra van rode dwerg–witte dwerg dubbelsterren is de positie van iedere combinatie bepaald in de kleur-kleur diagrammen. De punten die bij hetzelfde spectraal type van de rode dwerg horen, zijn verbonden, waardoor zogenaamde tracks gemaakt zijn. Aan de hand van de waargenomen kleuren van objecten in de 3-dimensionale $(u-g)$, $(g-r)$ en $(r-i)$ kleurruimte, is een classificatie van de temperatuur van de witte dwerg en het spectraal type van de rode dwerg gemaakt op basis van het meest nabije punt op een track. Dit is eerst gedaan voor de objecten met spectra om te kunnen vergelijken met de resultaten van de spectrale fitting. De fotometrische en spectrale karakterisatie komen erg goed met elkaar overeen. De fouten op de temperatuur van de witte dwerg en op het spectraal type van de rode dwerg zijn afgeleid van de vergelijking tussen de twee methoden en bedragen ongeveer $2\,000$ K voor de temperatuur en ongeveer een half subtype voor het spectraal type van de rode dwerg. Voor elk

object afzonderlijk kunnen de fouten vrij groot zijn, maar voor de selectie als geheel is de fotometrische karakterisatie betrouwbaar.

In hoofdstuk 6 is vervolgens alleen de fotometrische selectie bestudeerd, dus ook de objecten zonder spectra. Aangezien de objecten geselecteerd waren als zijnde rode dwerg–witte dwerg dubbelsterren, is er dus aangenomen dat ze dat ook inderdaad zijn. Voor elk van deze objecten is er een classificatie gemaakt aan de hand van de fotometrische tracks. Met behulp van de absolute magnitudes van de bijbehorende rode dwerg–witte dwerg combinatie en de waargenomen magnitudes is de afstand bepaald voor elk van de objecten. Samen met de eigenbeweging en aannemende dat de snelheid in de gezichtslijn nul is, kon de 3-dimensionale snelheid in de Melkweg bepaald worden. De Melkweg bestaat uit meerdere populaties: dunne schijf, dikke schijf en halo objecten. Op basis van de 3-dimensionale snelheid is bepaald tot welke populatie een object behoord. Voor elk object op zich kunnen de fouten groot zijn, maar wanneer we naar de selectie als een geheel kijken, is dit goed bepaald.

Nu de afstanden en karakterisaties van de objecten bekend zijn, is de ruimtelijke dichtheid van rode dwerg–witte dwerg dubbelsterren bepaald. Aangezien er hier met een selectie op basis van eigenbewegingen gewerkt is, moest er een model van de Melkweg gemaakt worden om de missende fractie te kunnen bepalen. We hebben een simulatie gemaakt bestaande uit een dunne schijf, dikke schijf en halo populatie. Dezelfde selecties die aanwezig zijn op de waargenomen objecten zijn ook toegepast op deze modellen. Daarna hebben we de gesimuleerde modellen met relatieve fracties bij elkaar opgeteld en een schalingsfactor toegevoegd. Deze fracties en schalingsfactor zijn gevarieerd om de beste fit te krijgen aan de waargenomen populatie. Het resultaat is dat 92.4% tot de dunne schijf behoord, 5.1% tot de dikke schijf en 2.5% tot de halo. Hierbij hebben we wel de fractie van de dikke schijf vast moeten zetten op 5.5% van de dunne schijf (dus 5.1% van de totale populatie), omdat we anders geen betrouwbare waarden konden krijgen. Deze fracties komen overeen met een totale ruimtelijke dichtheid van $5.5 \cdot 10^{-5}$ pc^{-3} wat overeenkomt met de theoretische voorspelling van $3.6 \cdot 10^{-6}$ tot $1.6 \cdot 10^{-4}$ pc^{-3}.

Curriculum Vitae

The author of this thesis, Else Josephina Maria van den Besselaar, was born on 13 March 1980 in Schijndel. At the age of six, her family moved to a small village nearby, called Gemonde, where she grew up. In 1998 she obtained her VWO diploma at the Elde-college in Schijndel after which she started to study Astronomy at Utrecht University from which she graduated in January 2003. After her graduation she applied for a PhD position at the Department of Astrophysics at the Radboud University Nijmegen which resulted in this thesis. In the few months between the submission of the thesis and the defence, she went for a work visit to the Astronomy and Astrophysics Group at the University of Warwick. She has always practiced a variety of sports, like korfball and swimming, but she likes dancing the most. She has participated in Ballroom and Latin-American dancing competitions, followed by Argentine Tango and Salsa courses, and she has recently started Belly dancing.

Acknowledgements